

Max-Planck-Institut für Astrophysik

On Nucleosynthesis-Relevant Conditions in Neutrino-Driven Supernova Outflows

Almudena Arcones Segovia

Vollständiger Abdruck der von der Fakultät für Physik der Technischen Universität München
zur Erlangung des akademischen Grades eines

Doktors der Naturwissenschaften

genehmigten Dissertation.

Vorsitzender: Univ.-Prof. Dr. R. Krücken

Prüfer der Dissertation:

1. Priv.-Doz. Dr. H.-Th. Janka
2. Univ.-Prof. Dr. A. J. Buras

Die Dissertation wurde am 19.02.2007 bei der Technischen Universität München eingereicht

und durch die Fakultät für Physik am 29.03.2007 angenommen.

Contents

1	Introduction	5
1.1	Core-collapse supernovae	7
1.2	Neutrino-driven wind	8
1.3	Nucleosynthesis in neutrino-driven winds	9
1.4	Previous works	11
1.5	Aims of this thesis	12
2	Model description	15
2.1	Hydrodynamics	15
2.2	Gravity	16
2.3	Neutrino treatment	18
2.4	Definitions	19
2.5	Numerical grid	21
2.6	Boundary conditions	21
2.7	Initial model and progenitors	23
3	Spherically symmetric hydrodynamic simulations	25
3.1	The computed models	25
3.2	Comparison with fully relativistic wind solutions	26
3.3	Evolution of a reference case	32
3.4	Analytic discussion of the wind termination shock	39
3.5	Variations of inner boundary conditions	42
3.5.1	Neutron star contraction	42
3.5.2	Different neutrino luminosities and neutron star masses	43
3.6	Different progenitors	50
3.7	Summary	53
4	Results for two-dimensional models	55
4.1	The computed models	55
4.2	Evolution of a reference case in two dimensions	57
4.3	Analytic discussion: angular dependence	62
4.4	Two more models base on a $15 M_{\odot}$ progenitor	65
4.5	Progenitor variation	68
4.6	Comparison of one- and two-dimensional simulations	72
4.7	Summary	78
5	Summary and conclusions	81

1

Introduction

In 1957 Margaret and Geoffrey Burbidge, William Fowler, Fred Hoyle, and Alistair Cameron presented in a pioneering work the details of nucleosynthesis in stars by neutrons (Burbidge et al. 1957; Cameron 1957). The theories at that time claimed that all elements were already present after the Big Bang and before the first stars were formed, in contrast to their work, which explained the origin of metals¹ as a consequence of processes occurring in stars. According to Burbidge et al. (1957) “*the history is hidden in the abundance distribution of the elements*”. Their reasoning was based on three main features, which can be distinguished in the element abundance curve (Fig. 1.1): A rapid drop of the abundance from mass numbers $A = 1$ to $A = 50$, a big peak around $A \approx 56$, and smaller, slow decline (with mass number) of the abundances for $A > 56$. From each of these features it is possible to extract some information about properties of the nuclei and hints on the mechanisms that led to their formation.

The most abundant nuclei, hydrogen and helium, are ashes of the Big Bang. These ashes themselves are burned in stellar interiors producing the metallic elements as residue. During the life of a star, nuclear burning in the center produces the pressure necessary to hold the star up against the force of gravity. The price paid by the star is the change of its composition: In the first burning stage hydrogen is burned to helium, which in turn is converted to carbon in the second stage. Increasingly heavy nuclei are produced in the later stages. Once one type of fuel is exhausted, the star contracts and its central temperature rises, thus allowing for the next type of fuel to be ignited. This process continues, in the case of massive stars² ($M > 8 M_{\odot}$), until an inert core of iron is formed in the center.

These burning stages give rise to the nuclei from mass number $A = 1$ to $A \approx 50$. The decrease of the abundances in this mass number range is due to the fact that the Coulomb barrier rises as the nuclear charge increases. On the other hand, also the binding energy per nucleon increases

¹Elements heavier than He

²For low mass stars, i.e. $M < 8 M_{\odot}$, the final composition of the core depends on the central temperature that the star can reach and which is related to its mass (gravitational pressure). For stellar evolution reviews with discussion of the different burning stages, see Clayton (1968); Arnett (1996)

with nuclear mass and reaches its maximum for ^{56}Fe , the most tightly bound of all nuclei. This explains the pronounced abundance peak around iron. The production of any heavier nuclei by direct fusion is endothermic and thus strongly suppressed, compared to the lighter ones. From the astrophysical point of view the production of elements lighter than iron in stellar interiors is well understood (see Clayton 1968). Most of the iron is produced in thermonuclear supernovae, violent events in which the explosive disruption of a white dwarf is triggered by mass accretion from a companion star.

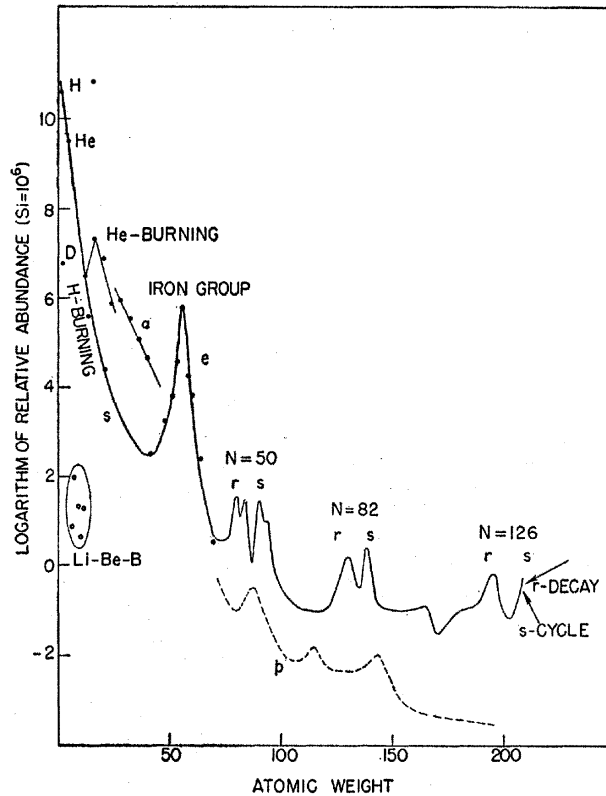


Figure 1.1: This is the original figure of the paper of Burbidge et al. (1957), which shows the element abundance distribution. One can distinguish the elements formed by nuclear fusion in stellar interiors, they are indicated in the figure as H- and He-burning products. The peak in the iron-group elements is one of the most remarkable features. For heavier elements r, s, and p indicate that they are generated by rapid and slow neutron capture or by proton capture, respectively. The numbers ($N = 50, 82, 126$) correspond to magic numbers for closed neutron shells.

After the iron-group peak the abundance curve exhibits a much slower decrease with mass number and the absolute abundances are much higher than the values one would expect if they were produced in the same way (i.e. by charged-particle reactions) as the lighter elements. Where and how are these heavy elements produced? The basic mechanism for nucleosynthesis beyond iron is neutron capture, already proposed by Burbidge et al. (1957). As a result of neutron captures, a nucleus is transformed into heavier isotopes and moves out of the valley of stability. Eventually it undergoes a beta decay, which transforms a neutron into a proton and thus increases the charge number Z by 1 without changing the mass number A . If every neutron capture is immediately followed by a beta decay the process is known as s-process. Here s means slow and refers to the fact that the neutron capture timescale is longer than the beta decay time ($\tau_\beta \ll \tau_n$). Therefore the new nuclei remain close to the valley of stability. In

contrast, when the timescale between two neutron capture reactions is much smaller than the beta decay timescale ($\tau_\beta \gg \tau_n$), nuclei are produced far away from the valley of stability and close to the neutron drip line. This process is called rapid or r-process. For both processes maxima in the abundance distribution are reached for certain “magic” neutron numbers, which correspond to closed neutron shell configurations. However, owing to the fact that s- and r-process occur along different paths in the N-Z plane these maxima are located at different mass numbers. This is the reason for the double peaks visible in Fig. 1.1.

Different astrophysical sites are needed for these two kinds of processes. The s-process nuclei are understood to be products of neutron captures on preexisting silicon-iron “seed” nuclei, occurring under hydrostatic burning conditions in both helium-burning cores of massive stars and particularly the thermally pulsing helium shells of asymptotic giant branch stars. The r-process nuclei are primary nucleosynthesis products formed under extreme and dynamic conditions. However, the exact site where r-process takes place is still unclear. The most promising sites are associated with supernova explosions of massive stars, as already proposed by Burbidge et al. (1957). However, there are other possible r-process scenarios like neutron star mergers (Lattimer et al. 1977; Rosswog et al. 1999), which can produce an r-process abundance pattern consistent with the solar system matter (Freiburghaus et al. 1999). However, it seems problematic that the frequency of such events in the Galaxy is too low (Qian 2000; Argast et al. 2004) and therefore a high amount of r-process matter has to be ejected per event, which is inconsistent with the level of scattering of r-process abundances observed in the halo stars. Accretion disks and outflows in collapsing stellar cores (LeBlanc & Wilson 1970; Cameron 2001) are another possibility also tied to massive stars and supernovae.

The core collapse supernova is one of the most promising and the best-studied r-process sites. However, neither the explosion mechanism itself, nor the nucleosynthesis taking place during the explosion are well-understood. In the following sections some details of this scenario and its nucleosynthesis implications are given.

1.1 Core-collapse supernovae

The composition of massive stars changes with time as they go through different hydrostatic burning stages (Arnett 1996). At the end of their life massive stars (Woosley et al. 2002) have developed an onion-shell like structure with a central core that consists of iron-group elements and is surrounded by shells of lighter elements – around the core silicon, and further out oxygen, neon, carbon, helium, and finally hydrogen. The inert iron core increases in mass owing to the silicon burning taking place at its surface. When the core mass approaches a mass close to the Chandrasekhar mass limit (about $1.44 M_\odot$), the gravity cannot be balanced by the pressure of the degenerate electrons any more and the core becomes unstable and starts to collapse. During the collapse gravitational energy is transformed into internal energy, which initially can be radiated away in form of neutrinos. However, this energy loss is stopped soon, when the density in the contracting core exceeds a density of about 10^{12}g cm^{-3} . At such densities the opacity for neutrinos becomes so high that they cannot stream out freely and are “trapped” in the collapsing core. Therefore most of the released gravitational energy remains stored as internal energy in the core.

The collapse is stopped when super-nuclear densities are reached and a proto-neutron star con-

sisting of almost incompressible matter forms. In the center the matter overshoots the hydrostatic equilibrium density and bounces back, thereby generating pressure waves that steepen into a shock wave, which travels outwards into the still infalling matter of the progenitor star.

Initially it was thought that this shock wave could propagate through the outer layers of the star and make them unbound, triggering an explosion. However, it turned out that in general this “prompt explosion mechanism” does not work, because the shock wave suffers severe energy loss and stagnates at only 100–200 km, still inside the collapsing iron core. On the one hand the energy loss is caused by the endothermic dissociation of the iron group nuclei falling through the shock. On the other hand, once the post-shock density has fallen below the trapping density, neutrinos are able to stream off freely again and remove considerable amounts of energy from the shock wave.

Already Colgate & White (1966) proposed that neutrinos leaking out of the forming neutron star, the so-called proto-neutron star could deposit energy in the layers close to the shock and compensate for these energy losses. Indeed, Wilson (1985) found in numerical simulations that neutrinos emitted by the proto-neutron star can deposit enough energy behind the shock to revive it and trigger an explosion (see also Bethe & Wilson 1985). Furthermore, it turned out that this mechanism requires several 100 ms of neutrino energy deposition before the explosion sets in. Consequently it is known as the “delayed, neutrino-driven explosion mechanism”.

However, improved simulations (e.g. better microphysics, general relativity effects, more sophisticated neutrino transport, multidimensional hydrodynamics) that have been performed in the past 20 years failed to demonstrate that the delayed explosion mechanism works robustly (Rampp & Janka 2000, 2002; Buras et al. 2003, 2006b,a; Mezzacappa et al. 2001; Liebendörfer et al. 2001; Thompson et al. 2003; Liebendörfer et al. 2005). Although several successful simulations have been reported (Kitaura et al. 2006; Buras et al. 2006b; Burrows et al. 2006), the viability of this mechanism for a wide range of parameters (e.g. progenitor masses, rotation rates) remains unproven. Nevertheless, all these simulations have helped to understand which effects play important roles. For example convection and other hydrodynamic instabilities have been recognized to improve the efficiency of energy deposition behind the shock (Herant et al. 1994; Burrows et al. 1995; Janka & Müller 1995, 1996). Despite these problems the delayed, neutrino-driven mechanism is still the most promising explanation for supernova explosions of massive stars (see Bethe 1990; Kotake et al. 2006; Woosley & Janka 2005 for reviews).

Independent of the details of the mechanism that leads to the onset of the explosion it is expected that the densities around the nascent neutron star will decrease in the subsequent evolution, which will allow for the formation of a neutrino-driven wind emanating from the neutron star surface.

1.2 Neutrino-driven wind

Neutron stars are born as extremely hot and dense remnants at the center of exploding massive stars. Shortly after their formation they heat up to temperatures that can reach tens of MeV and become even higher than 50 MeV for soft nuclear equations of state (e.g., Burrows & Lattimer 1986; Keil & Janka 1995; Pons et al. 1999). Their gravitational binding energy is carried away by neutrinos, which are abundantly produced at such conditions. On a timescale of seconds these neutrinos diffuse out of the interior of the star and escape from their mean surface of last

scattering, the neutrinosphere. By the associated energy and lepton number loss, the hot, still proton-rich and neutrino-opaque proto-neutron star thus evolves to the final cold, neutron-rich and neutrino-transparent remnant during roughly the first minute of its life.

Outside of the neutrinosphere the radiated neutrinos, which have typical energies of 10–20 MeV, travel through a layer with a very steep density gradient and decreasing temperature. It is unavoidable that the residual interactions of the high-energy neutrinos with the cooler stellar matter deposit energy in this region. This energy transfer does not allow the “surface” layers of the hot, neutrino-cooling neutron star to remain in hydrostatic equilibrium, but leads to mass loss at a low rate in a neutrino-driven outflow of baryonic matter (Duncan et al. 1986; Woosley & Baron 1992). This outflow, the so-called “neutrino-driven wind”, unavoidably accompanies the birth of a hot, neutrino-cooling neutron star, independent of the details of the not finally understood supernova explosion mechanism. The mass loss of the nascent neutron star begins after the supernova explosion has been launched and continues until the neutron star is essentially transparent to neutrinos.

Only in case the neutrino-driven outflow becomes supersonic beyond a critical point, the sonic point, it truly deserves the name “wind”. In such wind solutions the physical conditions at the neutrinosphere and behind the supernova shock are causally disconnected. The presence of the sonic point unambiguously determines the solution for a given value of the driving luminosity. Wind solutions possess the highest (“critical”) mass loss rate (and the lowest specific total energy of the ejected matter) for a given neutrino luminosity. Physical solutions with larger mass loss rates (and lower specific total energy) do not exist. Lower mass loss rates (higher specific total energies) correspond to “breeze solutions” (Takahashi & Janka 1997; Otsuki et al. 2000). In these, the outflow velocity reaches a maximum and then decreases again to asymptote to zero at infinity. The whole region between the proto-neutron star surface and the outer boundary of the considered outflow is therefore in sonic contact. While wind solutions are characterized by a continuously rising velocity and decreasing temperature, the temperature of breezes levels off to a constant value at large radii where the flow is dominated by internal instead of kinetic energy. This limiting value of the temperature at large distances from the neutron star is an additional characteristic parameter of breeze solutions.

1.3 Nucleosynthesis in neutrino-driven winds

This flow of baryonic matter is a rapidly expanding and cooling high-entropy environment – conditions that can lead to the production of elements heavier than the iron group. A number of parameters have been recognized to determine the possibility of r-process nucleosynthesis in the neutrino-wind environment:

- the neutron-to-proton ratio in the wind, expressed in terms of the electron-to-baryon ratio or electron fraction Y_e ;
- the expansion timescale, τ , which decides how fast the temperature and density of the outflowing matter drop;
- the wind entropy per nucleon, s , as a measure of the photon-to-baryon ratio of the environment.

Nucleosynthesis processes taking place during supernova expansion start with high temperature and density. The extreme conditions in the first phase of the supernova explosion allows the system to be in nuclear statistical equilibrium (NSE), i.e. there is a balance between nuclear reactions, which produce heavy nuclei, and photodisintegration that decompose those existing heavy nuclei into nucleons. The entropy for a system in equilibrium has a maximum, which means that the system has evolved until all possible states of the total energy are available. In nuclear statistical equilibrium the mass fraction of a nucleus AZ is given by (Meyer et al. 1992; Woosley & Hoffman 1992)

$$Y(Z, A) = G(Z, A) [\zeta(3)^{A-1} \pi^{(1-A)/2} 2^{(3A-5)/2}] A^{3/2} \left(\frac{kT}{m_N c^2} \right)^{3(A-1)/2} \phi^{1-A} Y_p^Z Y_n^{A-Z} \exp \left[\frac{B(Z, A)}{kT} \right], \quad (1.1)$$

where $G(Z, A)$ is the nuclear partition function, $B(Z, A)$ is the binding energy, T is the temperature, k is the Boltzmann constant, $\zeta(3)$ is the Riemann zeta function, m_N is the nucleon mass, Y_p and Y_n are the proton and neutron fraction, respectively, and ϕ is the photon-to-baryon ratio given by

$$\phi = \frac{n_\gamma}{\rho N_A} = \frac{1}{\pi^2} \frac{g_\gamma}{(hc)^3} \frac{\zeta(3)(kT)^3}{\rho N_A}, \quad (1.2)$$

where g_γ is the spin factor for photons, h is the Planck constant, N_A is the Avogadro number, and ρ is the baryon density. The photon-to-baryon ratio is proportional to the entropy per baryon in a relativistic gas, which is

$$s \approx \frac{4}{3} a \frac{(kT)^3}{\rho N_A}, \quad (1.3)$$

here a is the Stephan-Boltzmann constant. Therefore, combining Eqs. (1.2) and (1.3) we get the relation between the photon-to-baryon ratio and the entropy, i.e. $\phi \approx 10s$.

Equation (1.1) indicates that the presence of a nucleus depends strongly on ϕ and $B(Z, A)/kT$. If ϕ is of the order of unity, iron-group nuclei are favored in NSE because of their large binding energies, $B(Z, A)$. In contrast, if ϕ is large, many photons are available per baryon, and the result is a gas consisting mostly of nucleons and alpha particles in which it is difficult to build up heavy nuclei because they are quickly photodisintegrated.

In the first half a second after bounce, the temperatures and densities are high enough to maintain equilibrium. During the expansion the temperature decreases and consequently the NSE composition varies. For $T_9 \sim 10$ ($T_9 = 10^9$ K) alpha particles start to appear. With the decrease of the temperature the reactions begin to proceed more slowly, and finally the reaction rates become smaller than the expansion rate. These reactions first fall out of equilibrium and then “freeze out”. At the breakdown of the NSE ($T_9 \sim 6$) alpha-particles recombine into heavier nuclei starting with the triple-alpha reaction ($3\alpha \rightarrow {}^{12}\text{C}$), and followed by alpha- and neutron-captures on the produced ${}^{12}\text{C}$. This is known as “alpha-process” (Witti et al. 1994), which continues until the Coulomb barrier for alpha-particles becomes too high ($T_9 \sim 3$) and the “alpha-rich freeze-out” of the charged-particle reactions takes place.

In the first one or two seconds after the onset of the explosion, the proton-rich ejecta ($Y_e > 0.5$) are exposed to an extreme neutrino flux. Recently, Fröhlich et al. (2006a) found that under such conditions the electron antineutrinos are absorbed by free protons producing a continuous supply of free neutrons, which are captured by the seed nuclei. This novel nucleosynthesis

process is known as νp -process (Pruet et al. 2006, 2005; Fröhlich et al. 2006b, 2005; Wanajo 2006). For later times the ejecta may become neutron-rich ($Y_e < 0.5$). In this case, after the alpha freeze-out, the expanding matter consists of heavy nuclei formed by alpha-process and free neutrons. The r-process sets in when these heavy seed nuclei capture the neutrons and experience beta decays. The neutron-to-seed ratio necessary to build up nuclei to $A \sim 240$ from seed nuclei with $A \approx 70 - 100$ has to be $Y_n/Y_{\text{seed}} > 100$. Therefore, during the alpha-process only a few seed nuclei are allowed to be formed in order to have enough neutrons left.

In addition to the neutron-richness of the matter, two more conditions have to be fulfilled to allow for the r-process: The entropy must be high and the expansion timescale short. The entropy of the wind is typically tens to more than $100 k_B$ per nucleon, making the wind environment a candidate for the so-called high-entropy r-process (Meyer et al. 1992; Meyer 1994). At very high entropy ($s \sim 300k_B$) the photodisintegration allows for the presence of only a few seed nuclei, and therefore, there are many free neutrons. On the other hand, the expansion timescale plays an important role during the alpha-process. The first alpha reaction is a three-body reaction that is very slow, so that for a sufficiently rapid expansion this reaction has no time to start the formation of heavy nuclei. Only if the time scale is very short (around a few milliseconds), it is possible to obtain a small abundance of seed nuclei and a high neutron density.

Together with the requirement that the conditions in the wind have to allow the r-process, the mass-loss rate decides whether the wind can be the major source of the observed galactic abundance of r-process material. These wind parameters (i.e. expansion timescale, entropy, mass loss rate) depend on the neutron star properties, in particular on the gravitational field of the neutron star and thus its mass and radius, and on the neutrino emission of the neutron star, i.e., the time-dependent luminosities and spectra of the radiated neutrinos (Qian & Woosley 1996). Since it is mainly the absorption of electron neutrinos, ν_e , and antineutrinos, $\bar{\nu}_e$, on free neutrons and protons, respectively, which heats the stellar gas and is responsible for driving the mass loss and for setting the electron fraction in the ejected gas, the emission properties of these neutrinos are most relevant.

1.4 Previous works

Transsonic neutrino-driven winds in the context of supernova explosions and nucleosynthesis were investigated by means of hydrodynamic simulations (Woosley & Baron 1992), analytic discussion (Qian & Woosley 1996; Cardall & Fuller 1997), and numerical solutions of the steady-state wind equations (Otsuki et al. 2000; Thompson et al. 2001). Otsuki et al. (2000) discussed the difference between winds and breezes, but like Wanajo et al. (2001) they concentrated on the subsonic solutions for their nucleosynthesis calculations, mainly because these allowed them to set a boundary value of the temperature at some large radius. This was understood to mimic the transition of the wind into a dense shell of ejecta behind the outgoing supernova shock, the presence of which hampered the free expansion of the wind. Such a behavior was found in calculations of supernova explosions by the Livermore group, which were employed in the r-process studies of Woosley & Hoffman (1992), Woosley et al. (1994), and Hoffman et al. (1996), and also in hydrodynamic simulations of neutrino-driven outflows by Wittl et al. (1994) and Takahashi et al. (1994), which were started from post-bounce models provided by the Livermore group. The outflow trajectories in these simulations showed temperature and density declining asymptotically to nearly constant values, which were reached when

the flow was gradually decelerated upon catching up with the slower, earlier ejecta behind the supernova shock. Sumiyoshi et al. (2000) and Terasawa et al. (2002) also referred to this behavior for using an artificially imposed constant pressure at the outer boundary in their Lagrangian hydrodynamic simulations of neutrino-driven mass ejection. The external pressure produced outflow deceleration similar to that found in the previous supernova models.

Applying modern, high-resolution shock-capturing schemes and a better numerical resolution to long-time hydrodynamic simulations of supernova explosions, Janka & Müller (1995) and Burrows et al. (1995) (see also the more recent models of Buras et al. 2006b used for nucleosynthesis studies by Pruet et al. 2005) discovered the formation of a wind termination shock caused by the collision of a transsonic neutrino-driven wind with the dense, slower ejecta shell behind the supernova shock. So far, however, this reverse shock, which leads to an abrupt deceleration and shock heating of the fast wind, has not received much attention. Subtle, potentially significant effects in the r-process nucleosynthesis that may depend in interesting ways on the location of and strength of the reverse shock were found by Thompson et al. (2001). Although these authors mentioned a rather modest reheating of the wind material by the reverse shock passage (that causes a increase of the specific entropy of $10 k_B$ per nucleon), they obtained a considerably enhanced production of third-peak r-process nuclei due to a slower post-shock expansion and a significantly higher temperature (0.05 MeV instead of 0.01 MeV for unshocked winds) at the time the r-process freeze-out happens. Also Wanajo et al. (2002), alluding to the possibility of a wind termination shock, introduced a freeze-out value T_f as the final temperature of the wind, i.e., they limited the temperature (and density) decrease in the supersonic wind by a chosen lower value. The choice of this temperature was, naturally, to some degree ad hoc, although Wanajo et al. (2002) justified it by nucleosynthesis considerations. A systematic and detailed exploration of the formation of the wind termination shock, of its hydrodynamical effects on the wind properties, and of its nucleosynthetic consequences, however, is still lacking.

1.5 Aims of this thesis

This work is a study of the time-dependent evolution of the wind termination shock in different stellar progenitors with spherically symmetric (1D) and two-dimensional (2D) models. For this purpose, simulations of neutrino-driven explosions have been performed, employing some approximations to the full supernova physics already used in previous works (Scheck et al. 2004, 2006). The neutron star in the performed simulation is replaced by a contracting inner boundary at which neutrino luminosities are imposed such that supernova explosions with a typical explosion energy of $1-2 \times 10^{51}$ erg = 1–2 bethe (B) are triggered by neutrino heating. The subsequent evolution of the relic neutron star and the explosion ejecta are followed until 10 s after core bounce in the case of one-dimensional simulation and during around 2 s for the more computationally expensive two-dimensional calculations. Varying the neutron star contraction, which depends on the incompletely known high-density equation of state, and the time-dependent neutrino emission from the forming neutron star, the sensitivity of the reverse shock effects on the neutrino-wind properties will be investigated. By means of two-dimensional simulations one can demonstrate that convection does not destroy the effect of the reverse shock, but makes it angular dependent. This has a direct influence on the amount of ejected matter with high entropy, i.e. possible favourable nucleosynthesis conditions. The one- and two-dimensional results found in this work suggest that wind termination shocks are a robust, long-lasting feature

in the supernova core just like the outgoing supernova shock and the neutrino-driven wind are. Of course, since a final understanding of the explosion mechanism of core-collapse supernovae is still missing (see, e.g. Buras et al. 2003, 2006b,a, and references therein) and because of the excision of the neutron star at the grid center (instead of simulating its neutrino-cooling evolution) and of the approximations contained in the neutrino transport method, the calculations of this work will not be able to yield final answers. Nevertheless, the results are suitable for discussing fundamental properties of the wind termination shock and for developing a basic understanding of how this so far not well studied aspect of supernova explosions may influence the nucleosynthesis.

This work is structured in the following way. In Chapter 2 I will briefly describe the numerical approach taken in this work, give definitions of several quantities that will be used later, and present the progenitor stars that are used as initial models. Spherically symmetric models are addressed in Chapter 3, which starts with a presentation of a reference case, followed by an analytic discussion and an investigation of how varied boundary and initial conditions change the results. Two-dimensional simulations are the topic of Chapter 4, where the influence of multidimensional effects on the ejecta distribution and on wind termination shock evolution is analyzed. Finally, summary and conclusions follow in Chapter 5. Parts of this work were already presented in the publication of Arcones et al. (2007).

2

Model description

The neutrino-driven wind, which sets after the supernova explosion, has been studied in previous works by solving the steady state wind equations (see e.g. Thompson et al. 2001). However, full neutrino-hydrodynamic simulations are necessary to deal with the whole problem, i.e. the wind evolution and its interaction with the ejecta, in a consistent way. In this work we are not interested in proving the viability of the explosion mechanism because the neutrino-driven wind is independent of it. Therefore, we can use an approximate treatment that allows a higher variability of the conditions relevant for the wind. We are using Newtonian hydrodynamics (Sect. 2.1) with relativistic correction for the gravitational potential (Sect. 2.2). In order to save computational time and thus to be able to follow the wind for some seconds, simplified neutrino transport is required (Sect. 2.3). Moreover, we avoid using the nuclear density equation that is needed in the neutron star but it is still not well understood. Instead of it, we cut out the interior (Sect. 2.5) and take an inner boundary that mimics the neutron star contraction (Sect. 2.6). With these approximations one can follow the wind evolution for different progenitor stars, which initial models are presented in Sect. 2.7.

2.1 Hydrodynamics

The tool we are using is based on solving the Euler equations of hydrodynamics, since the matter can be considered as a fluid in the non-relativistic limit and in the absence of viscosity and magnetic fields. These equations express the conservation of mass, momentum and energy:

$$\frac{\partial \rho}{\partial t} + \nabla \cdot (\rho \mathbf{v}) = 0 \quad (2.1)$$

$$\frac{\partial \rho \mathbf{v}}{\partial t} + \nabla \cdot (\rho \mathbf{v} \mathbf{v}) + \nabla \mathbf{P} = -\rho \nabla \Phi + \mathbf{Q}_M \quad (2.2)$$

$$\frac{\partial \rho E}{\partial t} + \nabla \cdot ([\rho E + P] \mathbf{v}) = -\rho \mathbf{v} \cdot \nabla \Phi + Q_E + \mathbf{v} \cdot \mathbf{Q}_M + \rho Q_N \quad (2.3)$$

here ρ , \mathbf{v} , and P are density, fluid velocity, and pressure, respectively. The $E = |\mathbf{v}|^2/2 + \epsilon$ is the specific total energy, with ϵ being the specific internal energy, and Φ is the gravitational potential, computed by solving the Poisson's equation. The source terms, denoted by Q , account for the neutrino momentum (\mathbf{Q}_M) and neutrino energy (Q_E) transfer (see Sect. 2.3), and for the specific net energy gain from nuclear reactions (Q_N). The latter requires one additional continuity equation to be added the set of Eqs. (2.1)-(2.3) for calculating the evolution of the composition:

$$\frac{\partial \rho X_i}{\partial t} + \nabla \cdot (\rho X_i \mathbf{v}) = \rho \dot{X}_i \quad (2.4)$$

here ρX_i is the partial density of the nucleus i , $\rho \dot{X}_i$ denotes the source term due to nuclear reactions, and X_i is the mass fraction of that species. We do not solve the nuclear reaction network, but assume nuclear statistical equilibrium (NSE) during the phase between collapse and first seconds of the neutrino-wind. Under this assumption one can calculate the composition just from the temperature, density and electron fractions. The temperature and the density change every time a new hydrodynamical state is computed, while the electron fraction depends on the neutrino-matter interaction. Therefore, after performing a hydro step and after calculating the transport, one has to update the energy and composition values by means of the equation of state. The equation of state (EoS) is needed to close the system, by defining a relation between pressure, density, and temperature: $P = P(\rho, e_{\text{int}}, X_i)$ with e_{int} being the internal energy.

The equation of state used in the simulations presented here is valid below densities of roughly $10^{13} \text{ g cm}^{-3}$ where non-ideal effects due to strong interactions between nucleons can be safely ignored. It was used before in the calculations by Janka & Müller (1996), Kifonidis et al. (2003), and Scheck et al. (2006). Neutrons, protons, α -particles and a representative heavy nucleus of the iron group (chosen to be ^{54}Mn) are assumed to be non-relativistic Boltzmann-gases in nuclear statistical equilibrium. Electrons and positrons are treated as Fermi-gases of arbitrary degeneracy and arbitrary degree of relativity, and photon contributions are included as well. Pressure and energy are corrected for Coulomb effects due to the electromagnetic interactions between nucleons and the surrounding sea of charged leptons.

The simulations of this work were carried out with the neutrino-hydrodynamics code and the microphysics described by Scheck et al. (2006). The hydrodynamics module is a version of the PROMETHEUS code which is based on a direct Eulerian implementation of the Piecewise Parabolic Method (PPM) of Colella & Woodward (1984). It is a high-resolution shock capturing scheme and performs a conservative, explicit integration of the Newtonian hydrodynamics equations with third-order accuracy in space and second-order accuracy in time (see, e.g., Kifonidis et al. 2003 and references therein).

2.2 Gravity

Relativistic effects are taken into account in our Newtonian hydrodynamics code by using an “effective relativistic gravitational potential” (Rampp & Janka 2002). The simulations performed for this work (different from those of Scheck et al. 2006) employ the improved version of this potential described by Marek et al. (2006), who found excellent agreement with fully relativistic calculations during collapse and the first several hundred milliseconds after core bounce (test for the later neutrino-wind phase can be found in Sect. 3.2).

The approach consist in taking the general relativity version of the one-dimensional Newtonian hydrostatics equation

$$\frac{1}{\rho_0} \frac{\partial P}{\partial r} = -\frac{GM_r}{r^2} = -\nabla \Phi_{1D}^N, \quad (2.5)$$

here M_r is the baryonic mass enclosed at a radius r . The Tolmann-Oppenheimer-Volkoff equation is the general relativistic form of Eq.(2.5):

$$\frac{1}{\rho_0} \frac{\partial P}{\partial r} = -\frac{G\tilde{m}_{\text{TOV}}}{r^2} \left(1 + \frac{4\pi r^3 P}{\tilde{m}_{\text{TOV}} c^2 \Gamma^2} \right) \left(1 + \frac{P}{\rho c^2} \right). \quad (2.6)$$

The Newtonian gravitational potential (Φ_{1D}^N) have been replaced with the modified TOV potential:

$$\Phi_{\text{TOV}}(r) = -4\pi G \int_r^\infty \frac{dr'}{r'^2} \left(\frac{\tilde{m}_{\text{TOV}}}{4\pi} + \frac{r'^3 P}{c^2} \right) \frac{1}{\Gamma^2} \left(\frac{\rho + e + P}{\rho c^2} \right), \quad (2.7)$$

where ρ is the rest-mass density, $e = \rho\varepsilon$ the internal energy density with ε being the specific internal energy, and P is the gas pressure. The usually rather small corrections of the gravitational potential due to neutrino pressure, energy density, and flux terms (see Marek et al. 2006) are neglected in Eq.(2.7). The ‘‘modified TOV mass’’ \tilde{m}_{TOV} is given by

$$\tilde{m}_{\text{TOV}}(r) = 4\pi \int_0^r dr' r'^2 \left(\rho + \frac{e}{c^2} \right) \Gamma, \quad (2.8)$$

with the metric function

$$\Gamma = \sqrt{1 + \frac{v^2}{c^2} - \frac{2\tilde{m}_{\text{TOV}}}{rc^2}}. \quad (2.9)$$

The extra factor Γ in Eq. (2.8), compared to the relativistic definition of the TOV mass, enters the mass integral for reasons of consistency with the Newtonian hydrodynamics equations and accounts for the fact that in the Newtonian code there is no distinction between local proper volume and coordinate volume (for more details, see Marek et al. 2006).

There is, however, an important difference of our calculations compared to those performed by Marek et al. (2006). While the latter included the whole neutron star down to the center, the use of the inner grid boundary at a radius $R_{\text{ib}} > 0$ in the present work prevents the evaluation of the integral in Eq. (2.8) within the neutron star core. We solve this problem by starting our calculations with a given value of the modified TOV mass of the core at $t = 0$, $\tilde{m}_{\text{TOV}}(R_{\text{ib}}, 0)$, which was provided to us as part of the data set for the initial conditions of our simulations. For $t > 0$ we then approximately evolve the modified TOV mass according to the expression

$$\tilde{m}_{\text{TOV}}(R_{\text{ib}}, t) = \tilde{m}_{\text{TOV}}(R_{\text{ib}}, 0) - \int_0^t L_v^{\text{ib}}(t') dt' - \int_0^t 4\pi R_{\text{ib}}^2(t') P_{\text{ib}}(t') \frac{dR_{\text{ib}}}{dt'} dt', \quad (2.10)$$

where the second term on the rhs yields the energy loss from the neutron star core by the total neutrino luminosity at the inner boundary, $L_v^{\text{ib}}(t)$, and the last term represents the compression (PdV) work done on the core at the contracting inner boundary. The total modified TOV-mass at radius r , which we consider as ‘‘gravitational mass’’, is thus given by

$$\tilde{m}_{\text{TOV}}(r, t) = \tilde{m}_{\text{TOV}}(R_{\text{ib}}, t) + 4\pi \int_{R_{\text{ib}}}^r dr' r'^2 \left(\rho + \frac{e}{c^2} \right) \Gamma. \quad (2.11)$$

In two-dimensional simulations asphericity of the potential is considered by using two-dimensional Newtonian corrections added to the Φ_{1D}^N :

$$\Phi_{2D} = \Phi_{1D}^{TOV} + (\Phi_{2D}^N - \Phi_{1D}^N) \quad (2.12)$$

2.3 Neutrino treatment

The role of the neutrinos in supernova is crucial, but the way they are included in the whole problem is not trivial. The most sophisticated neutrino treatment (Rampp & Janka 2002; Buras et al. 2006b,a) has the disadvantages that is computationally very expensive, thus it makes impossible to follow the evolution of the neutrino-driven wind during a few seconds, and it is not enough to explain explosion mechanism in general. On the other hand, the transport treatment used in previous works of neutrino-wind were rather simplified (Otsuki et al. 2000; Thompson et al. 2001). Here, we are using a neutrino transport approximation between both. The pros are that it is not very computational expensive but at the same time we are performing the radial integration of the grey energy and lepton number. Moreover, the results obtained with this neutrino transport are qualitatively the same as the ones coming from the most accurate Boltzmann transport, but not quantitatively. This is exactly the disadvantage, i.e. it is not possible to give final numbers for quantities like the electron fraction, which is crucial for nucleosynthesis.

The transport of neutrinos and antineutrinos of all flavors is based on a computationally very efficient, analytic integration along characteristics of the frequency-integrated zeroth-order moment equations of the Boltzmann equation for neutrino number and energy (for details, see the Appendix of Scheck et al. 2006). The zeroth-order moment of the equation of radiative transport for spherical symmetry is:

$$\frac{\partial}{\partial t} E + \frac{1}{r^2} \frac{\partial}{\partial r} (r^2 F) = Q^+ - Q^- \quad (2.13)$$

where E is the energy density and F the energy flux. In the rhs the source term is separated into emission rate Q^+ and absorption rate Q^- .

The neutrino spectra are assumed to have Fermi-Dirac shape, in which case

$$\mathcal{F}_n(\eta) = \int_0^\infty dx \frac{x^n}{1 + \exp(x - \eta)}, \quad (2.14)$$

with a spectral temperature that is determined from the ratio of neutrino-energy to neutrino-number flux. Therefore in general the spectral temperature is different from the local gas temperature. The closure of the neutrino number and energy equations is achieved by employing the flux factor:

$$f(r, t) = \frac{F}{E_C}, \quad (2.15)$$

which couples the local energy (or number) flux with the neutrino energy (or number) density. For $f(r, t)$ we use a prescribed function which was determined by fits to Monte Carlo transport results (Janka 1991). This yields a reasonably good approximation in the transparent and semi-transparent regimes but is not designed to accurately reproduce the diffusion limit at very high

optical depths (where due to numerical reasons the applicability of the approach is anyway strongly constrained by the need of very fine grid zoning, Sect. 2.5).

Therefore, assuming that $\partial_t f = 0$ and in terms of the luminosity ($L = 4\pi r^2 c_{\text{eff}} = 4\pi r^2 f c E$, with $c_{\text{eff}} = f c$ being the effective speed of neutrino propagation), Eq.(2.13) can be writing as:

$$\frac{\partial}{\partial t} L + c_{\text{eff}} \frac{\partial}{\partial r} L = 4\pi r^2 c_{\text{eff}} (Q^+ - Q^-). \quad (2.16)$$

The coefficients Q^+ and $\bar{\kappa} = \kappa/f = 4\pi r^2 Q^-/L$ can be considered constant between two points (r, t) and (r^*, t^*) which are connected by a characteristic line: $r^* = r - c_{\text{eff}}(t - t^*)$. Under this assumption, Eq.(2.16) can be solve analytically. Details about the numerical scheme to calculate the luminosity as a function of time and radius are given in Scheck et al. (2006). The integration yields the neutrino number ($L = L_n$) and energy fluxes ($L = L_e$) as functions of time and radius for three neutrino types: $\nu_e, \bar{\nu}_e$, and ν_x (with $\nu_x = \nu_\mu, \bar{\nu}_\mu, \nu_\tau, \bar{\nu}_\tau$). Our approach thus accounts for the luminosity contributions due to the accretion on the forming neutron star.

The neutrino source terms in the transport equation (Eq. 2.16) and thus the source terms for lepton number, energy, and momentum in the hydrodynamics equations include the most relevant neutrino-matter interactions:

- Charge-current processes with neutrons and protons,

$$\nu_e + n \longleftrightarrow p + e^-, \quad (2.17)$$

$$\bar{\nu}_e + p \longleftrightarrow n + e^+, \quad (2.18)$$

- Thermal electron-positron pair creation and annihilation,

$$e^+ + e^- \longleftrightarrow \nu_i + \bar{\nu}_i \quad (i = e, \mu, \tau), \quad (2.19)$$

- Neutrino scattering off nuclei (A), nucleons, and electrons and positrons,

$$\nu_i + \left\{ \begin{array}{c} A \\ n \\ p \\ e^\pm \end{array} \right\} \longleftrightarrow \nu_i + \left\{ \begin{array}{c} A \\ n \\ p \\ e^\pm \end{array} \right\}. \quad (2.20)$$

The neutrino emission and absorption rates for these processes are described in detail in the Appendix D.6 of Scheck et al. (2006).

2.4 Definitions

Here we introduce some quantities that will be used in the following chapters. The neutron star is defined by its radius and mass. The neutron star radius, R_{ns} corresponds to the location where the density is 10^{11}g cm^{-3} . The baryonic and gravitational mass are computed for the matter inside the neutron star radius. The baryonic mass of the neutron star, M_{ns} , is given by the central point mass plus the mass integral over all the grid zones below the neutron star radius.

The gravitational mass for the neutron star is given by Eq. (2.11) for $r = R_{\text{ns}}$. And the effective mass for the neutron star, M_{eff} , is the mass for which a Newtonian force equals the modified TOV force, i.e.

$$\frac{d\Phi_{\text{TOV}}}{dr} = \frac{GM_{\text{eff}}}{r^2}, \quad (2.21)$$

evaluated at $r = R_{\text{ns}}$

We define also some quantities related with the neutrinos, e.g. the total energy radiated in neutrinos of all flavours:

$$\Delta E_{\nu}^{\text{tot}}(t) = \int_0^t L_{\nu}^{\text{tot}}(r, t') dt', \quad (2.22)$$

where $L_{\nu}^{\text{tot}}(r, t')$ is the total neutrino luminosity given by the integration of Eq. (2.16). Usually the neutrino luminosity and the radiated energy are evaluated at radius of 500 km. These quantities are also given for ν_e and $\bar{\nu}_e$.

The inner boundary neutrino luminosity is

$$L_{\text{ib}}(t) \equiv L_{e,\nu_e}(R_{\text{ib}}, t) + L_{e,\bar{\nu}_e}(R_{\text{ib}}, t), \quad (2.23)$$

We use two definitions for the mean neutrino energy. One is defined as the ratio of neutrino energy flux to neutrino number flux,

$$\langle \epsilon_{\nu} \rangle \equiv \frac{L_e}{L_n}, \quad (2.24)$$

and another as rms (root mean squared) energy,

$$\langle \epsilon_{\nu} \rangle_{\text{rms}} \equiv \sqrt{\langle \epsilon_{\nu}^2 \rangle} \equiv k_{\text{B}} T_{\nu} \sqrt{\frac{\mathcal{F}_5(\eta_{\nu})}{\mathcal{F}_3(\eta_{\nu})}}, \quad (2.25)$$

which is the energy that enters the calculation of the neutrino absorption rates on nucleons (cf., for example, Scheck et al. 2006). In Eq. (2.25), T_{ν} and η_{ν} are the spectral temperature and degeneracy, assuming that the neutrino spectra have Fermi-Dirac shape (Eq. 2.14).

The explosion energy, E_{exp} , is defined as the sum of the total energy of all zones of the grid where the energy is positive, i.e.

$$E_{\text{exp}} = \sum_{e_{\text{tot},i} > 0} e_{\text{tot},i} \Delta m_i, \quad (2.26)$$

where i is the zone counter, Δm_i the mass contained in zone i , and e_{tot} is the total specific energy given by the sum of the specific gravitational, kinetic, and internal energies,

$$e_{\text{tot}} = e_{\text{grav}} + \frac{1}{2}v^2 + e_{\text{int}}. \quad (2.27)$$

Here we use the one-dimensional Newtonian expression to evaluate the gravitational energy,

$$e_{\text{grav}}(r) = -\frac{GM(r)}{r} \quad (2.28)$$

General relativistic corrections have been taken into account in the simulations, but can be neglected in the post-processing calculation because the majority of the matter that contributes to the explosion energy is placed at larger radii, where the Newtonian calculation does not differ from the general relativity one.

Another quantity related with the explosion itself is the explosion timescale, t_{exp} , which is the post-bounce time when the explosion sets in. Here, it is defined as the moment when the energy of the expanding postshock matter exceeds 10^{49} erg.

2.5 Numerical grid

The hydrodynamic equations are solved in a spherical grid (r, θ) . In the radial direction the inner boundary corresponds to a Lagrangian mass shell that is below the neutrinosphere, and the outer boundary is settle at $\sim 10^{10}$ cm, its exact value is chosen such that the supernova shock does not run off the grid. We note that the steepening density gradient near the neutron star surface requires extremely fine grid zoning for getting converged results of the neutrino-driven outflow. Therefore, the zone size fulfils the following prescription:

$$dr_i = \begin{cases} \alpha R_{\text{ib}} & \text{if } r \leq R_{\text{const}}, \\ \alpha r_i & \text{if } r > R_{\text{const}}, \end{cases} \quad (2.29)$$

where $\alpha \approx 2 - 3\%$. In the region between the inner boundary and the radius $R_{\text{const}} = 20 - 40$ km, the radial zones have the same size. And between R_{const} and the outer boundary the size of the zones increases logarithmically with radius.

In the angle direction, all the simulations presented in this work have a resolution of $\Delta\theta = 1^\circ$ and are performed for half sphere, $\theta_{\text{tot}} = \pi$. We denote as ‘‘north pole’’ the angle $\theta = 0$, and as ‘‘south pole’’ $\theta = \pi$.

We typically use about 1000 radial mesh points and, for the two-dimensional simulations, 180 angular beams.

2.6 Boundary conditions

In our simulations we replace the inner core of the neutron star (usually roughly $1 M_\odot$ of baryonic matter) by an inner Lagrangian boundary of our grid, whose prescribed contraction is supposed to mimic the shrinking of the nascent neutron star as it loses energy and lepton number by neutrino emission. Using this inner boundary, which typically is located at a ν_e optical depth of more than 100 and a density of $\rho_{\text{ib}} \gtrsim 10^{13}$ g cm $^{-3}$, does not only allow us to apply the simple neutrino transport approximation described above, but also gives us the freedom to vary the time-evolution of the neutron star radius and of the core neutrino fluxes imposed at the inner grid boundary. This makes sense because both the equation of state of hot neutron star matter and the neutrino transport in nascent neutron stars are not finally understood. Changing the inner boundary conditions thus allows us to investigate the differences resulting from different explosion energies and timescales and from a different evolution of the neutrino-wind power in a given progenitor.

Three parameters serve us to describe the motion of the inner boundary: R_i , R_f , and t_0 . The initial radius R_i is the radius of the inner core that we chose to excise from the post-bounce models we start our simulations from, R_f is the final radius of this core for time $t \rightarrow \infty$, and t_0 is the timescale of an exponential contraction according to the expression

$$R_{\text{ib}}(t) = R_f + (R_i - R_f)e^{-t/t_0} . \quad (2.30)$$

Our standard choice of $t_0 = 0.1$ s reproduces the contraction of the excised core during the first few hundred milliseconds after bounce as found in full-scale supernova simulations with the equation of state of Lattimer & Swesty (1991), using the energy-dependent neutrino transport of the VERTEX code (cf. Buras et al. 2006a and also Fig. 1 in Scheck et al. 2006).

In the simulations presented here we also explore the consequences of a different time-dependence of the neutrino luminosities imposed at the inner grid boundary (see Sects. 3.1 and 3.5). The explosion energy of a model is mostly determined by the choice of the initial values of these luminosities (in particular those of ν_e and $\bar{\nu}_e$). These initial values are constrained by the prescribed total loss of neutrino energy from the core during the proto-neutron star cooling, $\Delta E_{\nu, \text{core}}^{\text{tot}}$, and by the total loss of lepton number:

$$\Delta Y_{e, \text{core}}(t) = N_{\text{b,core}}^{-1} \int_0^t (L_{n, \nu_e}(R_{\text{ib}}, t') - L_{n, \bar{\nu}_e}(R_{\text{ib}}, t')) dt' = \frac{\Delta E_{\nu, \text{core}}^{\text{tot}}}{N_{\text{b,core}}} \left(\frac{K_{\nu_e}}{\langle \epsilon_{\nu_e} \rangle^{\text{ib}}} - \frac{K_{\bar{\nu}_e}}{\langle \epsilon_{\bar{\nu}_e} \rangle^{\text{ib}}} \right). \quad (2.31)$$

The relative contribution of ν_e to the total core luminosity is set to 20%, (i.e., $K_{\nu_e} = 0.2$ in terms of the parameters introduced in Scheck et al. 2006), the contribution of $\bar{\nu}_e$ is determined from requesting $\Delta Y_{e, \text{core}} = 0.3$, and the muon and tau neutrino contributions then follow from $K_{\nu_e} + K_{\bar{\nu}_e} + 4K_{\nu_x} = 1$. The mean energies of the neutrinos entering the computational grid at the inner boundary are chosen to be $\langle \epsilon_{\nu_e} \rangle^{\text{ib}} = 12$ MeV, $\langle \epsilon_{\bar{\nu}_e} \rangle^{\text{ib}} = 16$ MeV, and $\langle \epsilon_{\nu_x} \rangle^{\text{ib}} = 20$ MeV when ν_x denotes muon and tau neutrinos and antineutrinos. These energies are kept constant with time.

Because of the contraction and post-bounce accretion of the proto-neutron star, the density and optical depth in the layers near the inner grid boundary can increase to such large values that the application of our transport approximation becomes inefficient by the required very fine zoning, and the equation of state fails to describe the dense stellar matter. Whenever the ν_e optical depth begins to exceed a certain value (usually chosen to be 300), we shift the inner boundary to a larger radius $\widetilde{R}_{\text{ib}}(t_{\text{cut}})$ and thus to a larger mass shell where the neutrino optical depth is significantly lower (usually 200 for ν_e). The additional excised baryonic mass is added to the previous core mass and the gravitational mass of the new, increased core is set equal to the gravitational mass computed at radius $\widetilde{R}_{\text{ib}}(t_{\text{cut}})$ where the new inner grid boundary is placed (see Sect. 2.2). The subsequent motion of the new boundary for $t > t_{\text{cut}}$ is assumed to follow the function

$$R'_{\text{ib}}(t) = R_f + (\widetilde{R}_{\text{ib}}(t_{\text{cut}}) - R_f) \exp \left[v(t - t_{\text{cut}}) / (\widetilde{R}_{\text{ib}}(t_{\text{cut}}) - R_f) \right], \quad (2.32)$$

where $v < 0$ is the recession velocity of the mass shell of the new boundary at time t_{cut} . The new boundary contracts in a very similar way as the previous one because the removed shell is very narrow. The neutrino luminosities and mean energies of the streaming neutrinos imposed at the new boundary at $t = t_{\text{cut}}$ are chosen to be the values computed with the transport scheme at this radius and to have the same time behavior as the initial boundary luminosities and mean energies.

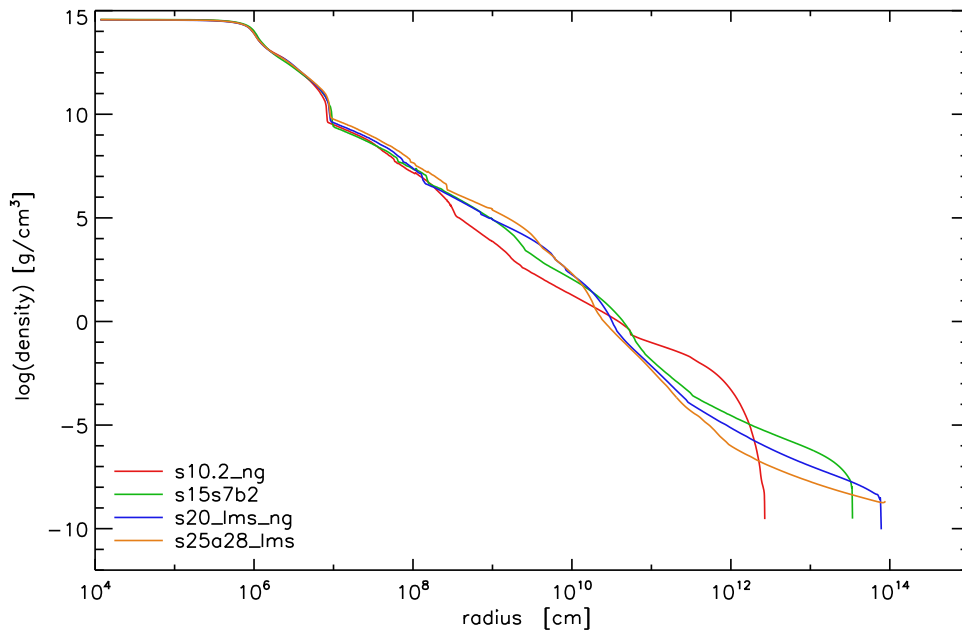


Figure 2.1: Density profiles for the progenitor stars we study (see Table 2.1). The differences at larger radii have a big influence for the shock expansion. For the progenitor with mass $10.2 M_{\odot}$ (red line) the density is lower and therefore the accretion is smaller, which allows to the shock to expand more rapidly. The $15 M_{\odot}$ and $20 M_{\odot}$ progenitor stars (green and blue lines, respectively) present a similar structure, thus their evolution will be also similar. The biggest progenitor (orange line) has $25 M_{\odot}$ and very high accretion rate, which leads slow shock expansion and a massive neutron star.

2.7 Initial model and progenitors

We start our simulations a few milliseconds after bounce and follow the shock stagnation and subsequent expansion, as well as the beginning of the wind and the its later interaction with the evolved supernova core. Starting after collapse allows us to ignore the neutron star in our simulation, and thus to reduce the computational time. The zero time of the model presented here corresponds to a few milliseconds after bounce (see Table 2.1). The collapse and bounce have been computed with neutrino-hydrodynamics code VERTEX producing the initial data for our simulations (A. Marek, private communication).

Table 2.1: List of progenitors used in the simulations

Progenitor	$M_{\text{ZAMS}} [M_{\odot}]$	t after bounce [ms]	Reference
s10.2	10.2	15.6	A. Heger personal communication
s15s7b2	15	15.1	Woosley & Weaver (1995)
s20.0	20.0	10.3	Woosley et al. (2002)
s25a28	25	12.9	Heger et al. (2001)

We have used four progenitors which cover a zero age main sequence mass (ZAMS mass) range from $10.2 M_{\odot}$ to $25 M_{\odot}$ (see Table 2.1). Figure 2.1 shows the density profiles of the progenitor at the time our simulations start.

3

Spherically symmetric hydrodynamic simulations

One-dimensional simulations require only modest amounts of computing time and therefore allow us to investigate a wide parameter range and also to study the evolution of the wind for several seconds. Since the neutrino-driven wind is spherical (in the absence of rotation, which is not considered in this study), the one-dimensional approach is adequate to study the evolution of the neutrino-driven wind and provides already basic information about the interaction of the wind with the explosion ejecta. However, in order to analyze this interaction in detail multidimensional simulations have to be performed (see Chap. 4). In this chapter we present the results of our time-dependent one-dimensional hydrodynamic simulations. An overview of the computed models will be given in Sect. 3.1. A comparison with fully relativistic wind solution is presented in Sect. 3.2. Sect. 3.3 contains the description of a reference case, which was computed for a certain choice of the time-dependent contraction of the inner grid boundary and of the neutrino luminosities imposed at this boundary. In Sect. 3.4 we demonstrate that basic features of the wind termination shock can be understood by simple analytic considerations. Furthermore, we investigate the influence of variations of the conditions at the inner boundary in Sect. 3.5, and finally we discuss the neutrino wind evolution in different progenitor stars (Sect. 3.6).

3.1 The computed models

A list of computed 1D models with their characterizing parameters is given in Table 3.1. We have performed simulations for progenitor stars which are presented in Tab. 2.1. Extensions of the model names (“r1”, “r2”,....) indicate different prescriptions for the contraction of the inner grid boundary, whose motion was varied by choosing different values of the final radius R_f and of the exponential contraction timescale t_0 (Eq. 2.30). Larger numbers in this sequence correspond to less quickly contracting or less compact neutron stars. Moreover, we varied

the sum of the ν_e and $\bar{\nu}_e$ luminosities imposed at the grid boundary with respect to the initial value as well as time-dependence. In most of the calculations the luminosities were chosen to be constant during the first second of post-bounce evolution and to decay proportional to $t^{-3/2}$ afterwards as in Scheck et al. (2006). Such models are labelled by the extensions “11”, “12”, etc., with a higher number meaning a lower initial value of the boundary luminosity. In another set of calculations the boundary luminosities were assumed to have a smoother time-dependence (with no jumps in the time derivative) and in particular with less neutrino energy radiated at late post-bounce times. The luminosities were prescribed as

$$L(t) = \begin{cases} L_0 & \text{if } t \leq 0.5\text{s}, \\ L_0 f(t) & \text{if } t > 0.5\text{s}, \end{cases} \quad (3.1)$$

with

$$f(t) = \frac{\exp[-(t - 0.5)^2] + b [1 + (t - 0.5)^n]^{-1}}{(1 + b)}, \quad (3.2)$$

where the time t is measured in seconds. The corresponding models can be recognized by the letters “lt” in their names. The parameter n was set to 1.5 in both cases, while $b = 0.2$ was used for model M15-lt1-r4 and $b = 0.3$ for M15-lt2-r3.

A comparison of these models allows us to study the influence of different contraction behavior of the nascent neutron star. The contraction determines the release of gravitational energy from the mantle layers of the compact remnant. The accretion luminosity generated in the mantle adds to the core flux (given by the imposed boundary condition) and has an influence on the explosion timescale and explosion energy of a model and thus on the location of the mass cut and the baryonic mass of the neutron star. The corresponding gravitational mass, which decreases when energy is lost in neutrinos (Eq. 2.10), the radius of the neutron star, and the luminosities and mean energies of the radiated neutrinos are crucial parameters that directly affect the neutrino-wind properties as functions of time (see Qian & Woosley 1996).

We note that the supernova models we study here do not permit us to change individually and independently all parameters and conditions that affect the neutrino wind properties and that determine the behavior of the wind termination shock. The wind depends, e.g., on the neutron star gravitational potential and thus on the neutron star mass. The latter becomes larger when the post-bounce accretion phase lasts longer and the explosion happens later, or when the progenitor is more massive and therefore the iron core and post-bounce accretion rate are larger. More massive progenitors thus tend to produce neutron stars with bigger masses. For this reason one cannot disentangle the influence of the progenitor structure on the wind termination shock from the effects of the neutron star mass on the neutrino wind.

In order to structure the discussion, we decided to first describe basic features in case of a $15 M_\odot$ reference model, then to vary the boundary conditions for this model, and finally to present the results for different progenitors.

3.2 Comparison with fully relativistic wind solutions

In this section we will discuss our simulation approach in view of other published work on relativistic steady-state solutions for neutrino-driven winds. General relativistic (GR) effects

Table 3.1: Model parameters of our spherically symmetric simulations. The different models are characterized by the chosen contraction of the inner grid boundary, which is expressed in terms of the final radius R_f and the exponential contraction timescale t_0 (cf. Eq. 2.30). Different choices of these values are indicated by the extensions “r1”, “r2”, etc. of the model names. In addition, different initial luminosities of ν_e plus $\bar{\nu}_e$ (measured in bethe [B] = 10^{51} erg per second) are imposed at the inner grid boundary in case of our standard luminosity behavior (constant until 1 s and then a $t^{-3/2}$ decay). These variations are reflected by the extensions “11”, “12”, etc. in the model names. Moreover, the time-dependence of the boundary luminosity has been modified to a luminosity decay that is more rapid than in the standard description (Eqs. 3.1 and 3.2; models with “1t” in their names).

Model	Contraction (R_f , t_0)	$L_{\nu_e}^{\text{ib}} + L_{\bar{\nu}_e}^{\text{ib}}$ [B/s]	Progenitor Mass [M_\odot]
M15-11-r1	9 km; 0.1 s	52.5	15
M15-11-r2	9 km; 0.2 s	52.5	15
M15-11-r5	11 km; 0.1 s	52.5	15
M15-11-r6	14 km; 0.1 s	52.5	15
M15-12-r1	9 km; 0.1 s	38.6	15
M15-13-r3	10 km; 0.1 s	35.8	15
M15-1t2-r3	10 km; 0.1 s	55.2	15
M15-1t1-r4	10.5 km; 0.1 s	55.8	15
M10-11-r1	9 km; 0.1 s	52.5	10
M10-15-r3	10 km; 0.1 s	30.3	10
M20-11-r1	9 km; 0.1 s	52.5	20
M20-13-r3	10 km; 0.1 s	35.8	20
M20-14-r3	10 km; 0.1 s	33.1	20
M25-15-r4	10.5 km; 0.1 s	30.3	25

have been recognized to cause important changes of the neutrino wind properties, e.g., to lead to a decrease of the expansion timescale and to an increase of the wind entropy, see Qian & Woosley (1996), Cardall & Fuller (1997), Sumiyoshi et al. (2000). A comprehensive discussion of these effects in comparison with the Newtonian treatment was provided by Otsuki et al. (2000) and Thompson et al. (2001).

In our simulations we account for relativistic gravity only by using a modified effective potential (Sect. 2.2), but otherwise we solve the Newtonian equations of hydrodynamics. We also ignore relativistic redshift and ray bending effects in our description of the neutrino transport (cf. Scheck et al. 2006).

The use of the generalized potential in a Newtonian hydrodynamics code was shown previously to yield results in very good agreement with relativistic core-collapse simulations up to several 100 ms after core bounce (Liebendörfer et al. 2005; Marek et al. 2006). For the later neutrino-wind phase we tried to compare with solutions plotted by Thompson et al. (2001) for cases when our neutron star masses, neutron star radii, and neutrino-heating rates were similar to the ones considered in that paper. Unfortunately, we were unable to find moments in our simulations where all relevant parameters match up exactly the cases considered by Thompson et al. (2001). As far as a comparison was possible, we observed satisfactory agreement in the main properties characterizing the wind.

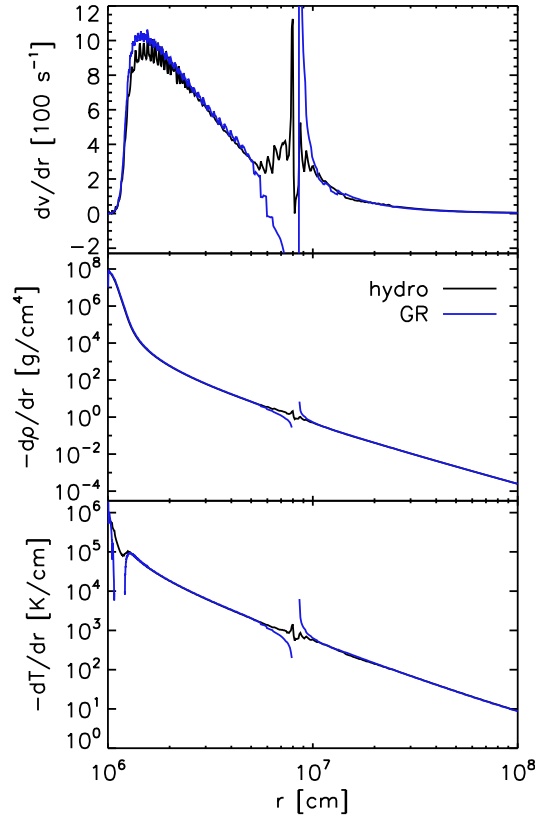


Figure 3.1: Derivatives of the velocity (top), density (middle), and temperature (bottom) as functions of radius from our hydrodynamic model M15-11-r1 at 1.5 s after bounce (black lines) compared to these derivatives as computed from the relativistic stationary wind equations of Eqs. (5)–(7) in Thompson et al. (2001) (blue curves). These equations were evaluated by using the values of all gas quantities as provided by our hydrodynamic model. Consistency between our hydrodynamics results (with approximative treatment of relativity) and the fully relativistic wind solution would require the corresponding lines to lie on top of each other. The agreement is very good and the sonic point is located at about 80 km in both cases. This location is a critical point of the wind equations, which explains the pathological behavior of the curves there. The evaluation of the expression for the temperature gradient is numerically inaccurate in a region where the two terms in Eq. (7) of Thompson et al.’s paper are very large and have opposite signs, in which case dT/dr becomes slightly positive while the hydrodynamical result is still negative.

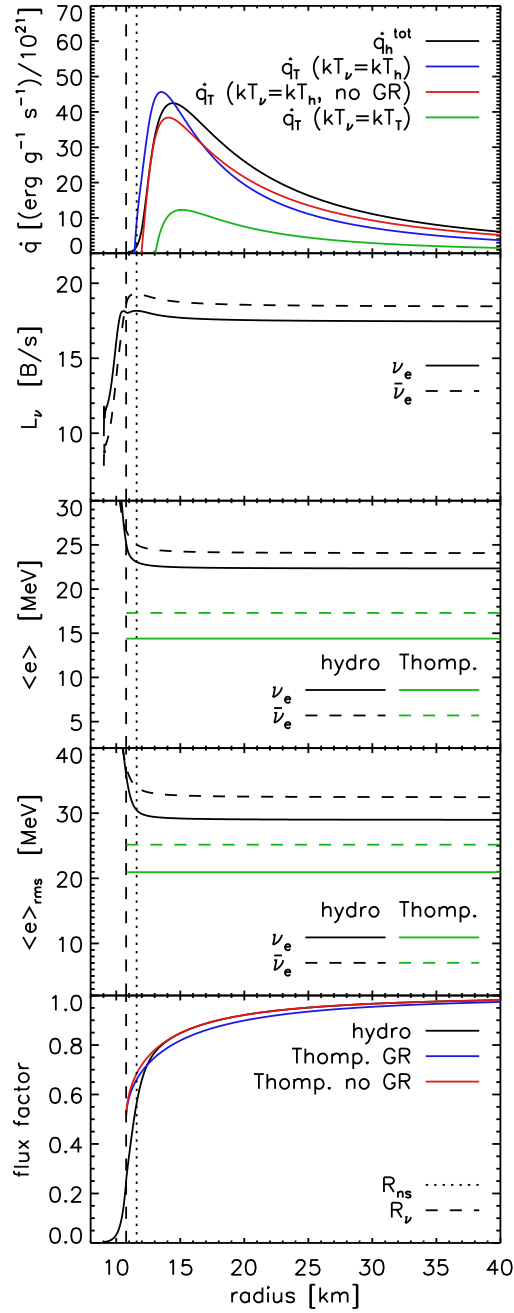


Figure 3.2: Radial profiles of the net total neutrino heating rate \dot{q}^{tot} (top), ν_e and $\bar{\nu}_e$ luminosities L_ν (second panel, in bethe per second or $10^{51} \text{ erg s}^{-1}$), mean neutrino energies $\langle \epsilon_\nu \rangle$ (third panel; Eq. 2.24), rms energies $\langle \epsilon_\nu \rangle_{\text{rms}}$ (fourth panel; Eq. 2.25), and flux factor for model M15-11-r1 at 1.5 s after bounce. For comparison with Thompson et al. (2001), we also show $\langle \epsilon_\nu \rangle$ and $\langle \epsilon_\nu \rangle_{\text{rms}}$ as used in that paper, rescaled to our values of L_{ν_e} and $L_{\bar{\nu}_e}$, the flux factor with and without relativistic corrections from that work, and the Newtonian and GR charged-current heating plus cooling rates using Thompson et al.’s formulas, evaluated with our neutrino luminosities and rms energies (red and blue curves) or with the rescaled rms energies of Thompson et al. (green curve). The vertical dashed line marks the position of the ν_e -sphere, and the vertical dotted line the neutron star “surface” at a density of $10^{11} \text{ g cm}^{-3}$.

A more quantitative comparison is hampered by the fact that relativistic neutrino-wind simulations are not available to us. We therefore decided to make use of Eqs. (5)–(7) for the velocity derivative, $\partial v/\partial r$, the density derivative, $\partial \rho/\partial r$, and the temperature derivative, $\partial T/\partial r$, in the paper of Thompson et al. (2001). Figure 3.1 shows these derivatives as functions of radius at a certain time for one of our models, compared to the results from Thompson et al.’s fully relativistic expressions. Evaluating the latter, we took all quantities on the rhs. of the formulas (velocity v , adiabatic sound speed c_s , density ρ , gravitational mass M , neutrino heating rate \dot{q} , etc.) from our model. Ideally, the pairs of corresponding curves in Fig. 3.1 should fall on top of each other, which would demonstrate consistency of both calculations. The overall agreement of the two cases is very good, with a small difference being visible only around the maximum of the acceleration, which, however, is located at the same radius. Also the sonic point is nearly at the same position of about 80 km (we are not disturbed by the pathological behavior of the curves in this region, where the expressions for the derivatives have a critical point). We therefore conclude that our approach reproduces the most important features of the relativistic solution, and that relativistic kinematics (which we ignore) is of minor importance compared to the effects of the stronger GR potential, which makes the proto-neutron star more compact and the density and temperature gradients in the neutrinospheric region steeper than in Newtonian gravity.

We also compared our neutrino heating and cooling rates with those used by Otsuki et al. (2000) and Thompson et al. (2001). Figure 3.2 shows the radius-dependent net (i.e., heating minus cooling) specific rate of neutrino energy deposition by the β -processes according to Eqs. (20) and (21) of Thompson et al. (2001) with and without corrections for relativistic redshift and ray bending, evaluated at all radii with the stellar parameters and the neutrinospheric values of the ν_e and $\bar{\nu}_e$ luminosities and mean energies from one of our simulations. The data were taken from the same model and time used in Fig. 3.1. The behavior of both curves agrees qualitatively with Fig. 5a of Otsuki et al. (2000). Close to the neutrinosphere ray bending effects enhance the net heating (since GR causes a reduction of the flux factor as visible for Thompson et al.’s prescription of this quantity in Fig. 3.2), whereas gravitational redshifting of the neutrino luminosities and energies grows monotonically with distance from the neutrinosphere and finally wins, reducing the GR rate below the Newtonian value. Otsuki et al. (2000) performed test calculations to disentangle the influence of GR corrections in the neutrino treatment from that of the relativistic terms in the wind structure equations. In spite of the sizable change of the local heating rate, Otsuki et al. (2000) found that neutrino redshift and ray bending have only little impact on the wind entropy. Similar conclusions were arrived at by Thompson et al. (2001).

In Fig. 3.2 also the total specific rate of neutrino heating and cooling from our hydrodynamical model is displayed. This rate includes all contributing processes, i.e. besides the β -reactions of ν_e and $\bar{\nu}_e$ absorption and production also energy transfer by the scattering off electrons, positrons, and free nucleons, and neutrino-antineutrino pair annihilation, to which neutrinos of all flavors contribute (cf. the appendix of Scheck et al. 2006). This total rate is similar to the neutrino capture and emission rates of Eqs. (20) and (21) of Thompson et al. (2001), because for the considered situation the neutrino luminosities are high (see Fig. 3.2) and therefore the wind mass loss rate is large and the wind entropy fairly low ($s_w \lesssim 50 k_B$ per nucleon). At such conditions of high wind density and modest abundance of e^+e^- -pairs, the other reactions do not contribute significantly to the total rate of energy deposition.

We point out here that our approximative treatment of neutrino transport evolves the transport solution self-consistently with the temperature and density structure of the stellar medium.

This is different from the light-bulb approach of previous steady-state or hydrodynamical wind studies (e.g., Sumiyoshi et al. 2000; Otsuki et al. 2000; Thompson et al. 2001). Inside the neutrinosphere neutrinos and matter are in equilibrium, around the neutrinosphere neutrinos begin to decouple thermodynamically from the medium, and at some larger distance they start streaming freely. A changing radial structure of the contracting neutron star leads to changes of the neutrino luminosities and mean energies, and the gradual loss of neutrinos drives the cooling and deleptonization of the surface-near layers of the neutron star. In previous wind studies (except full supernova models), such a coupling and interdependence was ignored. Close to the neutron star surface the flux factor (or flux dilution factor) used in our transport, which is based on a Monte Carlo calibration by Janka (1991), is lower than the vacuum approximation chosen by Thompson et al. (2001) and Otsuki et al. (2000), see Fig. 3.2. Thompson et al. (2001) have tested the improved description by Janka (1991) and found that its effects are negligible for the range of model conditions considered by them. This, however, is true only during phases where the density gradient near the neutrinosphere is very steep and in regions where the neutrino luminosities have already reached their asymptotic values.

The most important difference of our simulations compared to other relativistic wind studies is the different treatment of the spectra in the neutrino transport. In our “grey” but non-equilibrium description of neutrino number and energy transport, we determine a neutrino spectral temperature that is independent of the matter temperature and can be different from it (for details, see the appendix of Scheck et al. 2006). This leads to higher mean energies of ν_e and $\bar{\nu}_e$ radiated from the neutrinosphere than considered in the other works. Figure 3.2 shows these mean energies as functions of radius following the definitions given by Eqs. (2.24) and (2.25).

For comparison, Fig. 3.2 also presents the corresponding mean energies and rms energies as used by Thompson et al. (2001), appropriately scaled by $L_\nu^{1/4}$ to account for the larger neutrino luminosities considered here, and taking $\eta_\nu = 0$ for neutrinos and antineutrinos. The net heating rate computed with these rms energies is significantly lower than the heating rate from our hydrodynamic model (Fig. 3.2).

At first glance, our mean energies for ν_e and $\bar{\nu}_e$ might appear on the large side. One must, however, take into account that the mean energies in our simulations are significantly lower in the first ~ 0.5 seconds when the neutron star is still rather extended, and only increase as it heats up during contraction. They reach a maximum between one and two seconds after bounce to decrease afterwards as the proto-neutron star cools (see Sect. 3.3). So the conditions plotted in Fig. 3.2 correspond to a time when the neutrino luminosities are still rather high and the mean energies in this phase at their maximum. Moreover, one should remember that we ignore gravitational redshifting in our transport. The redshift from the neutrinosphere at radius R_ν to infinity after the contraction of the neutron star can become quite significant, $\sqrt{1 - 2GM/(R_\nu c^2)} = \sqrt{1 - R_s/R_\nu} \approx 0.7\dots 0.8$ for $\frac{1}{2} \gtrsim R_s/R_\nu \gtrsim \frac{1}{3}$, which reduces the mean energies for a distant observer by typically 20–30%. In our Newtonian transport treatment we prefer to use the higher neutrinospheric energies for evaluating the neutrino heating, because the neutrino-wind properties are mostly determined by the heating just outside of the neutrinosphere, where it is also strongest.

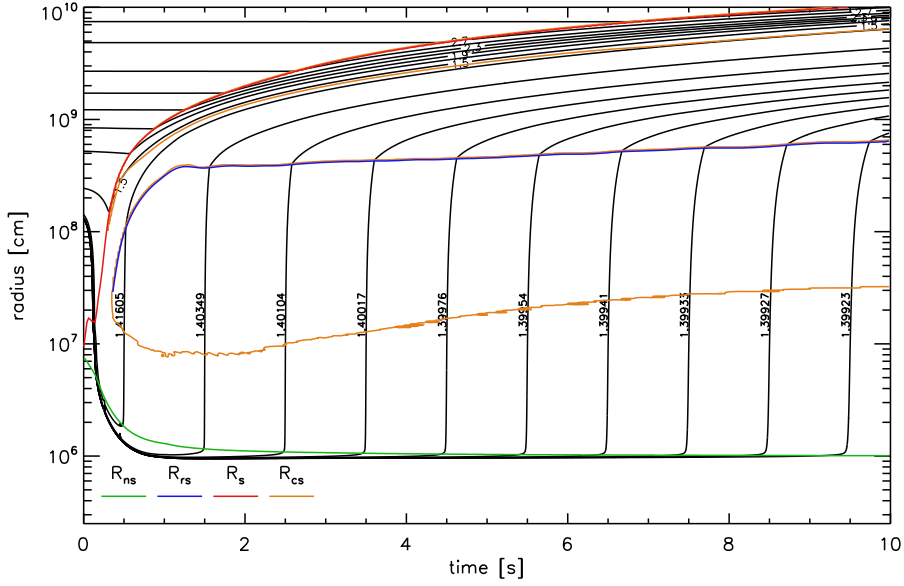


Figure 3.3: Mass shell plot for the evolution of model M15-11-r1. The explosion occurs about 0.2 seconds after bounce. The red line marks the supernova shock, the blue line the wind termination shock, the orange lines the locations where the expansion velocity of the gas equals the local sound speed (sonic points), and the green line the neutron star radius defined as the location where the density drops below $10^{11} \text{ g cm}^{-3}$. A contact discontinuity separates the dense shell of ejecta that were accelerated by the outgoing shock from the very dilute neutrino-driven wind. Mass shells in the wind are labelled by the corresponding enclosed baryonic masses.

3.3 Evolution of a reference case

In our reference model, M15-11-r1, the conditions at the inner boundary were chosen such that the $15 M_{\odot}$ star explodes with an energy of $\sim 1.5 \times 10^{51}$ erg and the neutron star attains a final gravitational mass of $\sim 1.2 M_{\odot}$ ($1.4 M_{\odot}$ baryonic) and a radius of 10 km (Table 3.2).

A mass-shell plot for the space-time evolution of this model is given in Fig. 3.3. The explosion sets in about 200 ms after bounce (at the time t_{exp} given in Table 3.2, which is defined as the moment when the total energy of expanding matter starts to exceed 10^{49} erg). At this time the stalled shock is revived by neutrino heating and starts continuous expansion with an average velocity of roughly $10,000 \text{ km s}^{-1}$. On its way out the shock reverses the infall of the swept-up matter. After the onset of the explosion, ongoing neutrino energy transfer drives an outward acceleration of heated material in the gain layer around the neutron star. At the interface between this dilute neutrino-driven wind and the denser outer ejecta a contact discontinuity is formed. Even farther behind the forward shock, the neutrino-driven wind, whose velocity increases rapidly with distance from the neutron star, collides with more slowly moving material and is decelerated again. The strongly negative velocity gradient at this location steepens into a reverse shock when the wind velocity begins to exceed the local sound speed (Janka & Müller 1995). First indications of a forming wind termination shock can be seen in Fig. 3.3 at $t \gtrsim 350$ ms post bounce at a radius $r \sim 300$ km.

Figure 3.4 displays the ν_e and $\bar{\nu}_e$ luminosities and the mean energies emitted by the nascent neutron star (gravitational redshift effects are ignored). One can see the accretion phase with

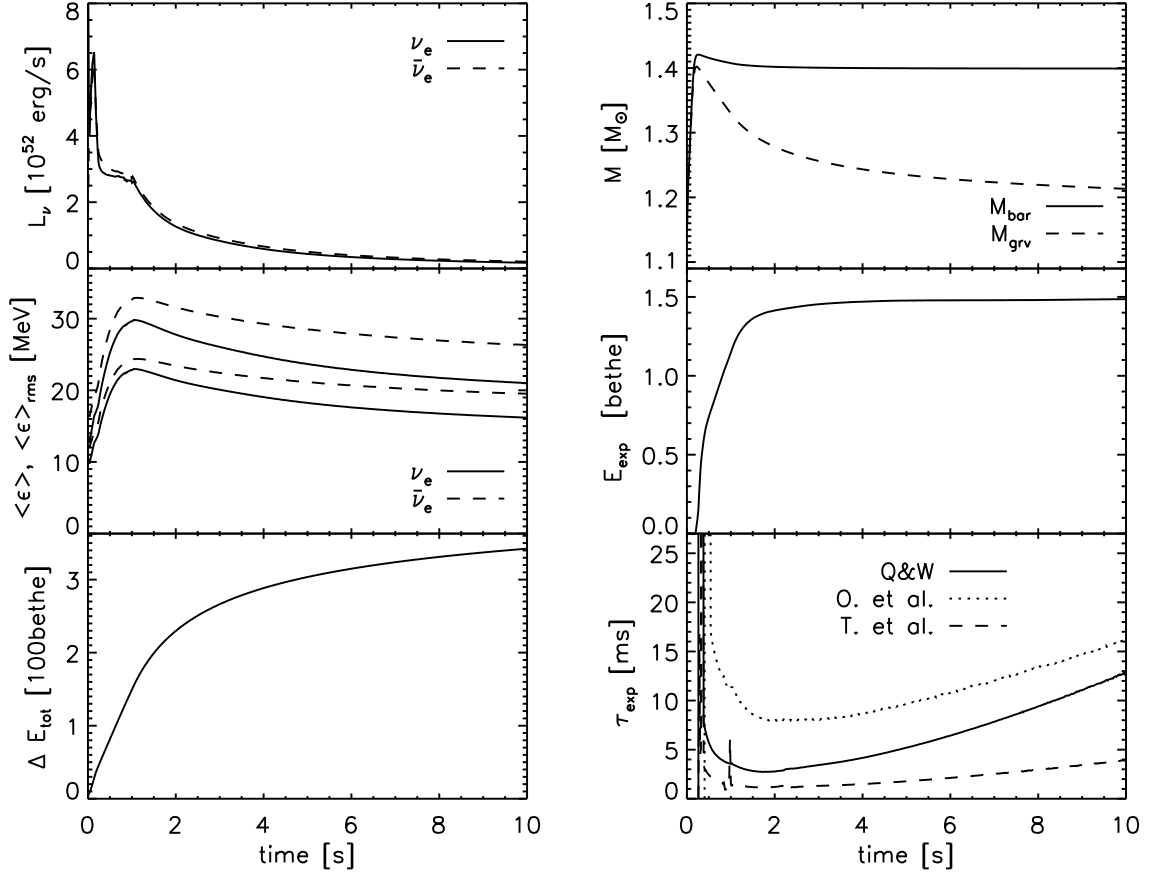


Figure 3.4: Luminosities, mean energies according to Eq. (2.24), and rms energies (Eq. 2.25, $\langle \epsilon \rangle_{\text{rms}}$ $\langle \epsilon \rangle$) of ν_e and $\bar{\nu}_e$, and total energy radiated in neutrinos of all flavors for model M15-11-r1 as functions of time (left), measured outside of the nascent neutron star (at a radius of 500 km). Note that we do not include gravitational redshifting in our neutrino treatment. The rapid decline of the luminosities after about 0.2 marks the end of the accretion phase of the forming neutron star at the onset of the explosion. The panels on the rhs side give the baryonic mass and the gravitational mass (Eq. 2.11) of the neutron star in model M15-11-r1, the explosion energy, and the expansion timescales of the neutrino-driven wind as functions of time. For the latter, the results from three different definitions are displayed, namely those used by Qian & Woosley (1996), Otsuki et al. (2000), and Thompson et al. (2001), given in Eqs. (3.3), (3.4), and (3.5), respectively.

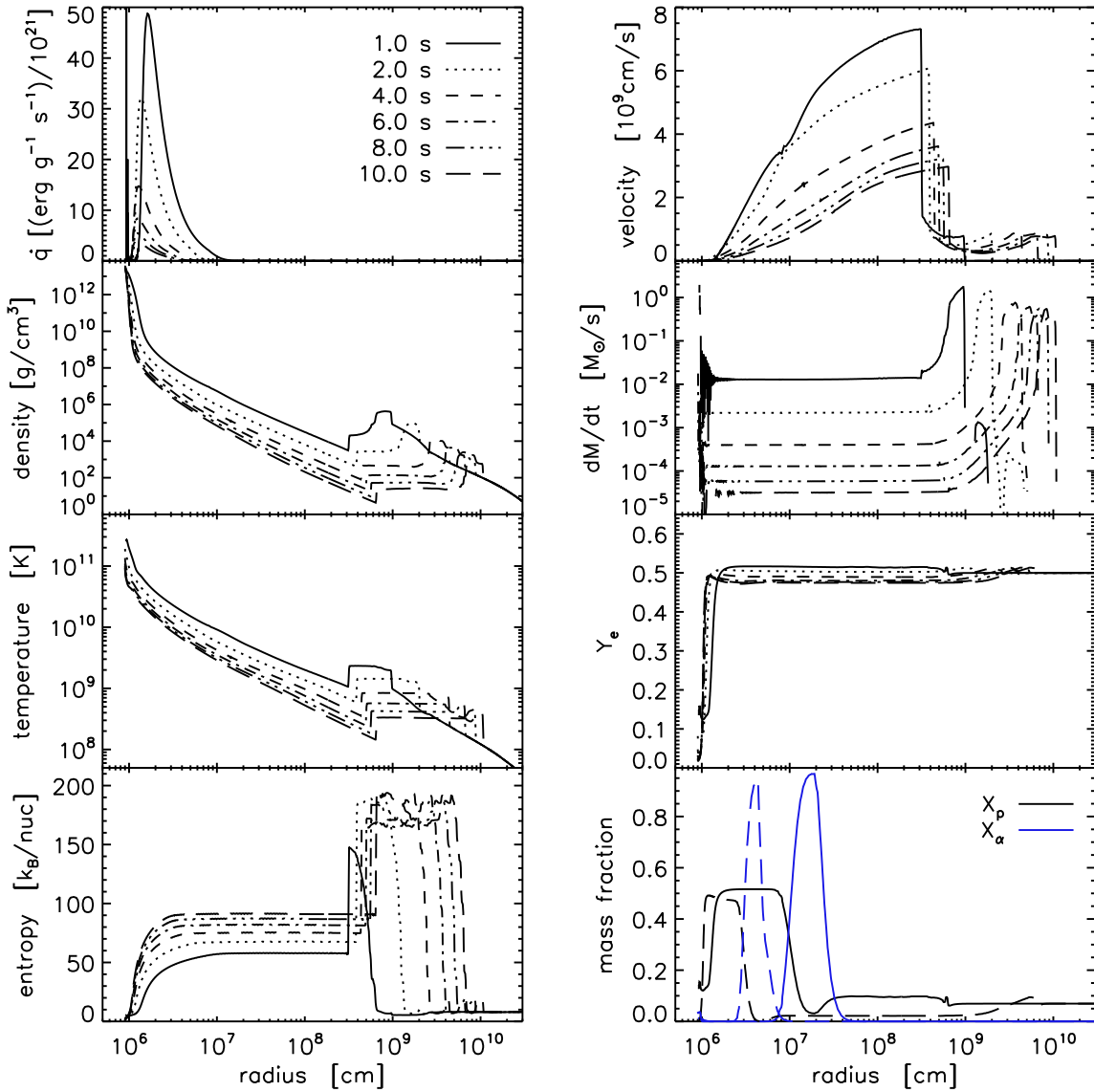


Figure 3.5: Radial profiles of the net neutrino-heating rate \dot{q} , density, temperature, entropy (left, from top to bottom), velocity, mass loss rate, electron fraction Y_e , and mass fractions of free protons and α particles for the neutrino wind in model M15-11-r1 at different post-bounce times. For the mass fractions only the information for the first and last moments of time is provided. The wind termination shock is clearly visible in its effects on the velocity, density, temperature, and entropy of the outflow.

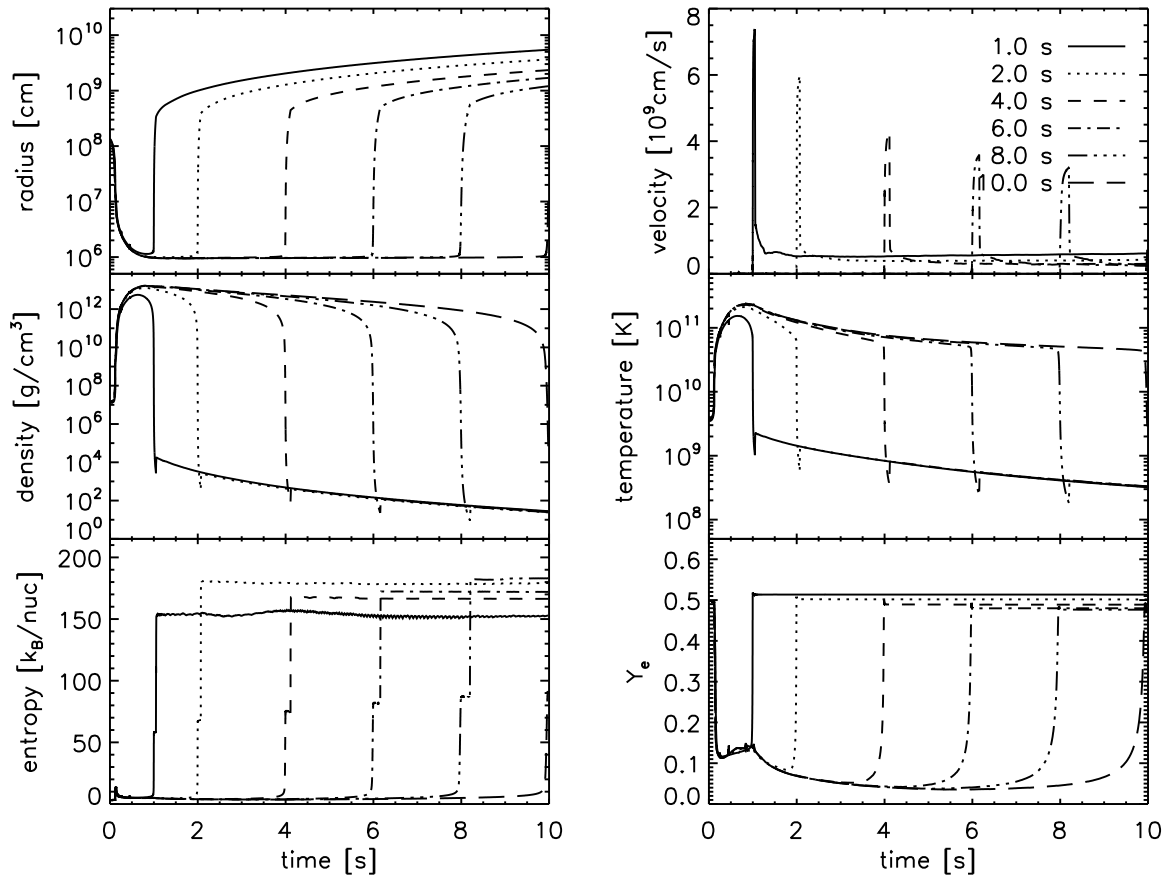


Figure 3.6: Radius, density, entropy (left, from top to bottom), velocity, temperature, and electron fraction Y_e as functions of time along the trajectories of different mass shells that are ejected in the neutrino-driven wind of model M15-11-r1. The times correspond to the moments when the mass shells cross a radius of 100 km. After a very rapid expansion, the wind is abruptly decelerated by the termination shock. This leads to an increase of the entropy by more than a factor of two, and to a subsequently much slower decline of the temperature and density.

its production of accretion luminosity ending at the time the explosion sets in. The following plateau phase until $t \approx 1$ s and subsequent decay of the luminosities show the influence of the time-dependence of the imposed boundary fluxes. This is also the case for the mean neutrino energies. Their values increase during the first second of post-bounce evolution because the inner grid boundary and the neutron star radius contract (Fig. 3.3). Consequently, the outer layers of the neutron star heat up due to the conversion of gravitational energy to internal energy by compression. After one second the rapid contraction is over and the decay of the boundary luminosities leads to less energy transport into these layers, which therefore begin to cool down, causing the mean energies of the radiated neutrinos to decline.

Figure 3.4 also provides information about the total energy carried away by neutrinos and antineutrinos of all three lepton flavors, ΔE_{tot} , as a function of time, and the corresponding reduction of the gravitational mass of the nascent neutron star. The latter is taken to be the modified TOV mass (Eq. 2.11) at the neutron star radius R_{ns} (which is defined as the radius where the density is 10^{11} g cm $^{-3}$). In contrast, the baryonic mass of the neutron star, given by the rest mass enclosed by the radius R_{ns} , initially increases in the course of accretion. After the explosion has taken off, it decreases again only slightly due to the mass loss in the neutrino-driven wind.

The middle panel on the right side of Fig. 3.4 reveals that about 50% of the explosion energy are contributed by the early neutrino wind, and after 2 s the energy has reached 95% of its final value. The panel below gives the expansion timescales of the ejected mass shells in the neutrino wind. The first definition follows Qian & Woosley (1996, Eq. 60), who introduced the dynamical timescale as

$$\tau_{\text{dyn}} = \frac{r}{v} \Big|_{k_{\text{B}}T=0.5 \text{ MeV}}. \quad (3.3)$$

We compare this with the cooling timescale used by Otsuki et al. (2000, Eq. 23),

$$\tau_T = \int_{k_{\text{B}}T=0.5 \text{ MeV}}^{k_{\text{B}}T=0.5 \text{ MeV}/e} \frac{dr}{v}, \quad (3.4)$$

variations of which were considered by Wittl et al. (1994, cooling time between $T = 7 \times 10^9$ K and $T = 3 \times 10^9$ K) and Wanajo et al. (2001, cooling time between $k_{\text{B}}T = 0.5$ MeV and $k_{\text{B}}T = 0.2$ MeV). The third definition we consider is the one of Thompson et al. (2001, Eq. 32), who employed the e-folding time of the density instead of that of the temperature,

$$\tau_{\rho} = \frac{1}{v} \left| \frac{1}{\rho} \frac{\partial \rho}{\partial r} \right|^{-1}_{k_{\text{B}}T=0.5 \text{ MeV}}, \quad (3.5)$$

where we set for our Newtonian simulations $y = 1$ in Thompson et al.'s Eq. (32). As can be expected from the fact that the wind is radiation-dominated and therefore $s \propto T^3/\rho \sim \text{const}$, the timescale τ_{ρ} is always significantly shorter than the cooling timescale τ_T (Fig. 3.4). Ideally, in such a situation one would expect $\tau_T/\tau_{\rho} = 3$, which is more closely reached at later stages when the wind entropy is higher (Fig. 3.5). Due to the different mathematical expressions in Eqs. (3.4) and (3.5), the factor 3 is never exactly realized. The third timescale, Eq. (3.3), yields a result that is between the other two values during most of the computed post-bounce evolution and comes closer to the timescale of Eq. (3.4) in the late stages of the simulations.

In Fig. 3.5 the radial profiles of different wind quantities are given for our reference model M15-11-r1 at a number of post-bounce times. The neutrino heating accelerates the wind to a peak

velocity of about 25% of the speed of light for neutrino luminosities $L_{\nu_e} \approx L_{\bar{\nu}_e} \approx 3 \times 10^{52} \text{ erg s}^{-1}$. The maximum velocity decreases as does the heating rate when the luminosities decline with time. The density and temperature in the wind region follow roughly the usual r^{-3} and r^{-1} behavior, respectively, in the region where the entropy is a constant. The profiles are slightly steeper and thus closer to these power laws at later times when the wind entropy is higher and the wind therefore more dominated by radiation pressure. The radial profiles of ρ and T also steepen at larger distance from the neutron star, leading to a visible increase of the wind acceleration at the point where free nucleons recombine to α -particles and the neutrino heating ceases (see the corresponding panels in Fig. 3.5). At this radius the entropy of the outflow reaches its final value. This asymptotic wind entropy increases from about $60 k_B$ per nucleon at 1 s to around $90 k_B$ at 10 s.

For (approximately) the same values of the ν_e and $\bar{\nu}_e$ luminosities, model M15-11-r1 tends to yield somewhat lower expansion timescales, slightly lower entropies, and a bit higher mass loss rates than those found by Thompson et al. (2001), see Figs. 5, 8, and Tables 1 and 2 there. This can be understood on the one hand by the smaller gravitational mass of the neutron star in our model compared to the canonical $1.4 M_\odot$ star considered by Thompson et al. (2001), and on the other hand it is caused by our larger heating rates due to the higher mean neutrino energies (cf. our discussion in Sect. 3.2). These differences affect the characteristic wind parameters with different sensitivity. According to Qian & Woosley (1996), the entropy scales with the neutrino luminosity L , the mean neutrino energy ϵ , the neutron star radius R , and the neutron star mass M like

$$s \propto L^{-1/6} \epsilon^{-1/3} R^{-2/3} M, \quad (3.6)$$

the expansion timescale like

$$\tau \propto L^{-1} \epsilon^{-2} R M, \quad (3.7)$$

and the wind mass loss rate like

$$\dot{M} \propto L^{5/3} \epsilon^{10/3} R^{5/3} M^{-2} \quad (3.8)$$

(modifications of these relations due to relativistic effects were addressed by Thompson et al. 2001).

During the first ~ 2 seconds after the onset of the explosion, the neutrino wind is p-rich, i.e. $Y_e > 0.5$. This is in agreement with explosion models that employ a Boltzmann solver for the spectral neutrino transport (see Buras et al. 2006b; Pruet et al. 2005). Afterwards the electron fraction drops below 0.5, and gradually the wind develops increasing neutron excess. Qualitatively, this trend to lower Y_e at later times is reproduced when the neutrino luminosities and mean energies from the simulation are inserted into the simple analytic relation $Y_e \sim [1 + (L_{\bar{\nu}_e} \epsilon_{\bar{\nu}_e} / L_{\nu_e} \epsilon_{\nu_e})]^{-1}$, although the values do not agree quantitatively. We emphasize here that the gray and approximative treatment of the neutrino transport employed in this work (for a critical assessment, see Scheck et al. 2006) is also not able to yield reliable results for the electron fraction in terms of absolute numbers. The competition of ν_e and $\bar{\nu}_e$ absorption on free neutrons and protons sensitively determines the asymptotic value of Y_e , an accurate calculation of which requires detailed information of the neutrino and antineutrino spectra in the co-moving frame of the expanding wind matter. The wind at late times might therefore become significantly more neutron rich than predicted in our models. Figure 3.5 also reveals that the

Table 3.2: Results of the 1D models at the end of the simulations at $t = 10$ s after bounce. M_{bar} is the baryonic mass of the neutron star. M_{grav} its gravitational mass (Eq. 2.11). Both masses are computed for the matter inside the neutron star radius R_{ns} . This radius is defined as the location where the density is $10^{11} \text{ g cm}^{-3}$. M_{eff} denotes an “effective mass” of the neutron star, for which a Newtonian potential equals the modified TOV potential of Eq. (2.7) at radius R_{ns} . ΔE_{tot} is the total energy radiated in neutrinos of all flavors (measured in beth [B] = 10^{51} erg). L_{ν_e} and $L_{\nu_e}^*$ are the luminosities of electron neutrinos and antineutrinos measured at 500 km (without gravitational redshifting), $\langle \epsilon_{\nu_e} \rangle$ and $\langle \epsilon_{\nu_e}^* \rangle$ are the corresponding mean energies, E_{exp} is the explosion energy (note that this energy can still decrease somewhat after 10 s because of the negative binding energy of the outer stellar layers, which is not included in the given numbers), t_{exp} is the post-bounce time when the explosion sets in (defined as the moment when the energy of expanding postshock matter exceeds 10^{49} erg), s_{w} is the asymptotic wind entropy per nucleon, and s_{rs} the entropy of the outflow after its deceleration in the wind termination shock.

Model	time [s]	M_{bar} [M_{\odot}]	M_{grav} [M_{\odot}]	M_{eff} [M_{\odot}]	ΔE_{tot} [100B]	R_{ns} [km]	L_{ν_e} [B/s]	$L_{\nu_e}^*$ [B/s]	$\langle \epsilon_{\nu_e} \rangle$ [MeV]	$\langle \epsilon_{\nu_e}^* \rangle$ [MeV]	E_{exp} [B]	t_{exp} [s]	s_{wind} [kg/nuc]	s_{rs} [kg/nuc]
M15-11-r1	10.0	1.399	1.207	1.910	3.422	10.09	1.73	2.06	16.19	19.52	1.486	0.201	91.10	190.55
M15-11-r2	10.0	1.446	1.263	2.031	3.335	10.27	1.96	2.28	16.37	19.50	1.174	0.341	94.19	191.29
M15-11-r5	10.0	1.394	1.208	1.703	3.307	12.94	1.78	2.11	14.57	17.62	1.371	0.221	71.97	131.94
M15-11-r6	10.0	1.440	1.258	1.648	3.274	16.71	1.61	1.93	13.04	15.98	1.043	0.241	61.04	83.63
M15-12-r1	10.0	1.473	1.280	2.116	3.451	9.94	1.74	2.12	16.46	20.30	1.019	0.381	100.14	193.14
M15-13-r3	10.0	1.545	1.341	2.121	3.709	11.22	1.99	2.34	15.88	18.97	0.709	0.701	92.75	155.84
M15-14-r3	10.0	1.397	1.253	1.906	2.602	11.28	1.33	1.54	15.04	18.12	1.239	0.221	90.19	132.57
M15-14-r4	10.0	1.395	1.260	1.878	2.421	11.81	0.96	1.12	14.33	17.40	1.231	0.221	91.02	96.92
M10-11-r1	10.0	1.314	1.132	1.721	3.251	10.22	1.63	1.96	15.85	19.06	1.247	0.321	83.48	476.93
M10-15-r3	10.0	1.344	1.187	1.745	2.817	11.49	1.47	1.72	14.98	18.04	0.716	0.421	80.94	353.32
M20-11-r1	10.0	1.422	1.233	1.973	3.388	10.10	1.74	2.05	16.23	19.52	1.486	0.181	94.18	127.89
M20-13-r3	10.0	1.595	1.411	2.310	3.383	11.10	1.60	1.90	15.66	18.79	0.375	0.761	105.10	—
M20-14-r3	10.0	1.523	1.332	2.118	3.437	11.03	1.61	2.00	15.69	20.00	0.847	0.421	95.32	106.84
M25-15-r4	10.0	1.971	1.657	2.944	5.924	11.56	2.95	3.58	16.88	20.01	1.700	0.401	113.75	117.89

mass loss rate reaches its asymptotic value closest to the neutrinosphere, then Y_e , and finally the entropy.

At a radius of a few 1000 km, the supersonic wind is abruptly slowed down in the termination shock. The compression leads to a density and temperature increase. The conversion of kinetic to internal energy in the shock boosts the entropy to more than twice the wind entropy in model M15-11-r1. This is a much more extreme impact of the termination shock than previously suggested in the literature (Thompson et al. 2001). The decelerated wind material is accumulated in a dense shell between the forward and reverse shocks. The pressure across this dense shell is nearly uniform, while the contact discontinuity between the accumulated wind matter and the dense layer of shock-accelerated progenitor gas is clearly visible in the density profiles. One should also notice that the conditions at the wind termination shock are by no means time-independent as previously assumed in nucleosynthesis calculations (e.g., Wanajo et al. 2002). Temperature and density at the reverse shock in model M15-11-r1 evolve, because the radial position of the reverse shock as well as the wind properties change with time. The impact of the wind termination shock on the conditions in the expanding wind mass shells is better visible in Fig. 3.6, where the time-evolution of different quantities is depicted as seen co-moving with some selected mass shells. The extremely rapid decline of the temperature and density in the fast wind are stopped and switch over to a much slower evolution. After the wind material has been added to the dense shell between the two shocks, it moves with nearly constant velocity. Its density therefore decays approximately like $\rho \propto t^{-2}$ and because the gas is radiation-dominated, its temperature follows roughly the power law $T \propto t^{-2/3}$.

3.4 Analytic discussion of the wind termination shock

The behavior of the wind termination shock and its effects on the neutrino-driven outflow can basically be understood by simple analytic considerations. For this purpose we consider the three Rankine-Hugoniot shock jump conditions for mass, momentum and energy flow,

$$\rho_{rs}u_{rs} = \rho_w u_w, \quad (3.9)$$

$$P_{rs} + \rho_{rs}u_{rs}^2 = P_w + \rho_w u_w^2, \quad (3.10)$$

$$\frac{1}{2}u_{rs}^2 + \omega_{rs} = \frac{1}{2}u_w^2 + \omega_w, \quad (3.11)$$

where the indices w and rs denote quantities of the wind just ahead of the shock and of the shocked matter just behind the shock, respectively. The fluid velocities u_w and u_{rs} are measured relative to the shock velocity, $u = v - U_s$, P is the pressure, ρ the mass density, and $\omega = (\varepsilon + P)/\rho$ the enthalpy per mass unit when ε is the internal energy density of the gas. In case of radiation-dominated and nondegenerate conditions, one can write $s = (\varepsilon + P)/(n_B k_B T)$ for the dimensionless entropy normalized by the baryon density $n_B = \rho/m_B$ (m_B is the average baryon mass), and therefore one gets

$$s_{rs}k_B T_{rs} - s_w k_B T_w = \frac{1}{2}m_B(u_w^2 - u_{rs}^2). \quad (3.12)$$

Since the wind termination shock strongly decelerates the wind, the postshock and preshock velocities fulfill the relation $u_w^2 \gg u_{rs}^2$. Thus the postshock entropy is approximately given by

$$s_{rs} \approx s_w \frac{k_B T_w}{k_B T_{rs}} + \frac{1}{2} \frac{m_B u_w^2}{k_B T_{rs}}. \quad (3.13)$$

Again making the assumption that the gas on both sides of the shock is radiation dominated, the dimensionless entropy per nucleon is given by

$$s = f_\gamma a_\gamma \frac{(k_B T)^3}{n_B}, \quad (3.14)$$

where $a_\gamma = a/k_B^4 = 2.08 \times 10^{49} \text{ erg}^{-3} \text{ cm}^{-3}$ is related to the radiation constant a , and f_γ is a factor whose exact value depends on the temperature and thus the mixture of radiation and e^+e^- pairs; assuming zero electron degeneracy, the corresponding range of values is $\frac{4}{3} \leq f_\gamma \leq \frac{11}{3}$. Equation (3.14) can be used to express $k_B T$ ahead of and behind the shock in terms of s and ρ . Using also that the densities are connected by $\rho_{\text{rs}} = \beta \rho_w$ with $\beta \sim 7$ for a strong shock and radiation-dominated conditions, one derives

$$s_{\text{rs}} \approx \left[\frac{s_w^{4/3}}{\beta^{1/3}} + \alpha^{1/3} \frac{u_w^2}{\rho_w^{1/3}} \right]^{3/4} \approx \left[\frac{s_w^{4/3}}{\beta^{1/3}} + 33.5 \frac{u_{w,9}^2}{\rho_{w,2}^{1/3}} \right]^{3/4}, \quad (3.15)$$

where $\alpha \equiv f_\gamma a_\gamma m_B^4 / (8\beta)$, $u_{w,9}$ is the wind velocity measured in 10^9 cm s^{-1} , $\rho_{w,2}$ the wind density in 100 g cm^{-3} , and the numerical value in the second expression was calculated with $\beta = 7$ and $f_\gamma = \frac{4}{3}$. Equation (3.15) can be rewritten in terms of the wind mass loss rate \dot{M}_w and reverse shock radius R_{rs} , using

$$\dot{M}_w = 4\pi R_{\text{rs}}^2 \rho_w v_w \quad (3.16)$$

and assuming that the shock velocity is negligible, and therefore $v_w = u_w$, which gives

$$s_{\text{rs}} \approx \left[\frac{s_w^{4/3}}{\beta^{1/3}} + (4\pi\alpha)^{1/3} \frac{R_{\text{rs}}^{2/3} u_w^{7/3}}{\dot{M}_w^{1/3}} \right]^{3/4} \approx \left[\frac{s_w^{4/3}}{\beta^{1/3}} + 28.7 \frac{R_{\text{rs},8}^{2/3} u_{w,9}^{7/3}}{\dot{M}_{w,-5}^{1/3}} \right]^{3/4}. \quad (3.17)$$

Here $R_{\text{rs},8}$ is in units of 10^8 cm and $\dot{M}_{w,-5}$ is normalized to $10^{-5} M_\odot$. If the wind entropy is low, $s_w \ll s_{\text{rs}}$, only the second terms in Eqs. (3.15) and (3.17) are relevant.

It is also possible to obtain an estimate of the reverse shock position from known supernova and wind parameters. In case of a strong shock, i.e., $P_{\text{rs}} \gg P_w$, one can derive from Eqs. (3.9) and (3.10) the relation $P_{\text{rs}} \approx (1 - \beta^{-1}) \rho_w u_w^2$. Using again Eq. (3.16) for ρ_w , one gets

$$R_{\text{rs}} \approx \sqrt{\left(1 - \frac{1}{\beta}\right) \frac{\dot{M}_w u_w}{4\pi P_{\text{rs}}}}. \quad (3.18)$$

Assuming the spherical shell between the forward shock at radius $R_s \gg R_{\text{rs}}$ and the reverse shock to have constant pressure and to be radiation dominated, one can make the approximation

$$P_{\text{rs}} \sim \frac{f_{\text{exp}} E_{\text{exp}}}{4\pi R_s^3}, \quad (3.19)$$

where f_{exp} is the fraction of the supernova explosion energy E_{exp} that is present as internal energy of the gas between forward and reverse shock. Plugging Eq. (3.19) into Eq. (3.18) one obtains

$$R_{\text{rs}} \sim \sqrt{\left(1 - \frac{1}{\beta}\right) \frac{\dot{M}_w u_w R_s^3}{f_{\text{exp}} E_{\text{exp}}}} \approx 4.14 \times 10^3 \sqrt{\frac{\dot{M}_{w,-5} u_{w,9} R_{s,10}^3}{f_{\text{exp},0.1} E_{\text{exp},51}}} \text{ [km]}. \quad (3.20)$$

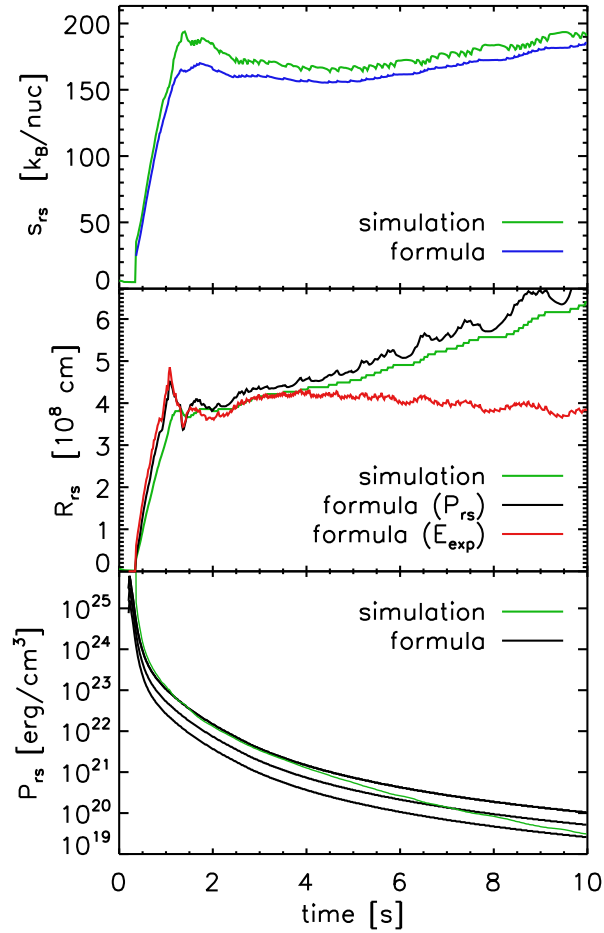


Figure 3.7: Entropy of the shocked material, reverse shock radius, and pressure above it. The green line in the three plots comes directly from simulation results, while the blue line in the upper plot is computed by using Eq. 3.17, the black lines are obtained using the approximation of Eq. 3.19, and the red line is gotten by plugging numbers in Eq. 3.20. In the middle plot $f_{exp} = 1$ is assumed obtaining the red and black lines. In the pressure plot the three black lines correspond to $f_{exp} = 0.25, 0.5, 1$ from the lowest to highest black curve.

The numerical value was computed by taking $\beta = 7$ and normalizing the shock radius to 10^{10} cm, the explosion energy to 10^{51} erg, and the parameter f_{exp} to 0.1.

In Figure 3.7 we show the analytic formulas derived above, evaluated with numbers for the wind quantities and compared to the results from the simulation for the reference model, M15-11-r1. The green line in the three plots correspond to the values taken directly from the simulation. In the upper plot the blue line was computed using Eq. (3.17), the result nicely agrees with the simulation data. In the middle plot there is some discrepancy, the black line which fits well with simulation data is calculated using Eq. (3.18), while for the red one we use Eq. (3.20) with $f_{\text{exp}} = 1$. The difference between the red and green lines is due to the approximation of the pressure in terms of the explosion energy. In the bottom plot the pressure calculated with Eq. (3.19) is plotted for $f_{\text{exp}} = 0.25, 0.5, 1$, increasing from the lower black curve to the higher ones. The simulation data match with the upper curve ($f_{\text{exp}} = 1$) during the first four seconds, and consequently the reverse shock radius predicted for this case (red line in the middle plot) agrees well with the radius measured in the simulations. From four seconds on, however, the pressure at the reverse shock is better approximated if one assumes a smaller contribution of the explosion energy (Eq. 3.20). As time goes on, an increasing fraction of the explosion energy is kinetic energy and not internal energy. The ejected matter is accelerated (PdV expansion work) at the cost of internal energy and, therefore, f_{exp} decreases.

3.5 Variations of inner boundary conditions

It is clear from Eqs. (3.15), (3.17), and (3.18) that the behavior of the reverse shock depends on the structure of the exploding star and on the neutrino-wind properties, in particular the wind mass-loss rate and velocity. Since the latter increases with the distance from the neutron star, the radius of the reverse shock introduces an additional velocity dependence in Eqs. (3.15), (3.17), and (3.18).

In order to investigate the changes associated with different strength and time evolution of the neutrino wind, we varied the wind-determining parameters, i.e., the neutron star mass, radius, and the core neutrino luminosities and energies and their time dependence. In this section we therefore discuss the influence of these variations, which are achieved by changing the inner boundary conditions.

3.5.1 Neutron star contraction

The neutron star contraction can be changed by using a different final radius for the neutron star or by modifying the contraction timescale (see Eq. 2.30). The effect of different neutron star radii is visible from a comparison of our reference model M15-11-r1 with models M15-11-r5 and M15-11-r6. Model M15-11-r2, on the other hand, has a different contraction timescale compared to the reference case .

Figure 3.8 shows the time evolution of quantities that determine and characterize the neutrino wind and reverse shock behavior in our simulations for different contraction parameters (see Table 3.1). These four simulations are computed with the same inner boundary condition for the neutrinos and produce neutron stars with approximately the same gravitational masses but

final radii of 10, 13, and roughly 17 km (Table 3.2). The neutrino luminosities radiated from the nascent neutron star and the energy emitted in ν_e and $\bar{\nu}_e$ as well as the total energy lost in neutrinos are nearly the same (Fig. 3.9). Because of similar explosion energies, also the supernova shock in the four models propagates with similar velocity (Fig. 3.8).

The mean neutrino energies, however, show a clear correlation with the neutron star radius: the more compact the neutron star is, the higher are the energies of the escaping ν_e and $\bar{\nu}_e$ in Fig. 3.9. Also the neutrino-wind properties reveal the variation with the compactness of the neutron star that is qualitatively expected from the analytic expressions given by Qian & Woosley (1996, see also Sect. 3.3, Eqs. 3.6–3.8). A larger R_{ns} leads to a longer expansion timescale and thus lower wind velocity, larger mass-loss rate, and smaller wind entropy (see Fig. 3.8). In case of the mass-loss rate, however, the influence of the larger neutron star radius is partly cancelled by the lower mean neutrino energies (see Eq. 3.8) (and by the slightly higher neutron star mass of model M15-11-r6), for which reason the differences in \dot{M} are rather modest, in particular between models M15-11-r5 and M15-11-r6.

Qualitatively, the reverse shock exhibits the same behavior in these two models as in M15-11-r1. While its radius R_{rs} is essentially the same in models M15-11-r1 and M15-11-r5, the wind termination shock, however, expands less strongly in model M15-11-r6, reacting to the considerably lower wind velocity and slightly slower propagation of the supernova shock in this somewhat less energetic model (cf. Eqs. 3.18 and 3.20). Finally, the entropy of the matter decelerated in the reverse shock behaves as expected from Eqs. (3.15) and (3.17) when values for the wind parameters and reverse shock radius are inserted into these equations. It is highest in model M15-11-r1 and lowest in model M15-11-r6. The densities behind the reverse shock are ordered inversely.

Model M15-11-r2 has a slower contraction than model M15-11-r1 but the same final radius (see left column of Fig. 3.8). Yet, the contraction in the first seconds does not determine the later evolution of the wind. When the final radius is reached both models approach to the same values for the wind quantities, i.e. wind entropy, expansion timescale, and mass-loss rate (see Fig. 3.8). The slower contraction results in a larger neutron star mass and a lower explosion energy (Fig. 3.9). The neutrino energy is larger for the rapid contraction model during the first two seconds of the evolution because its neutron star radius is smaller. However, once the neutron star radius is the same for both models, then, also the neutrino properties have the same values. The entropy at the reverse shock (right column of Fig. 3.8) in the model M15-11-r2 is the same as for the reference cases after 6 s, although the reverse shock radius is still smaller for the model with slower contraction (M15-11-r2).

3.5.2 Different neutrino luminosities and neutron star masses

The neutrino luminosity has a non negligible effect on the wind properties (see Qian & Woosley 1996 and Sect. 3.3). When the luminosity decreases, the wind entropy and the expansion time scale increase and the wind mass loss rate decreases, as we have shown in the reference case after one second. In order to study the effect of the time evolution of the luminosity we compare our reference case, M15-11-r1, to two other models (M15-lt1-r4 and M15-lt2-r3) with different temporal evolution of the luminosity (Eq. 3.1, Eq. 3.2). Another model (M20-l3-r3) with lower inner boundary luminosity (see Tab. 3.1) and different progenitor star allows us to study also the influence of a larger neutron star mass.

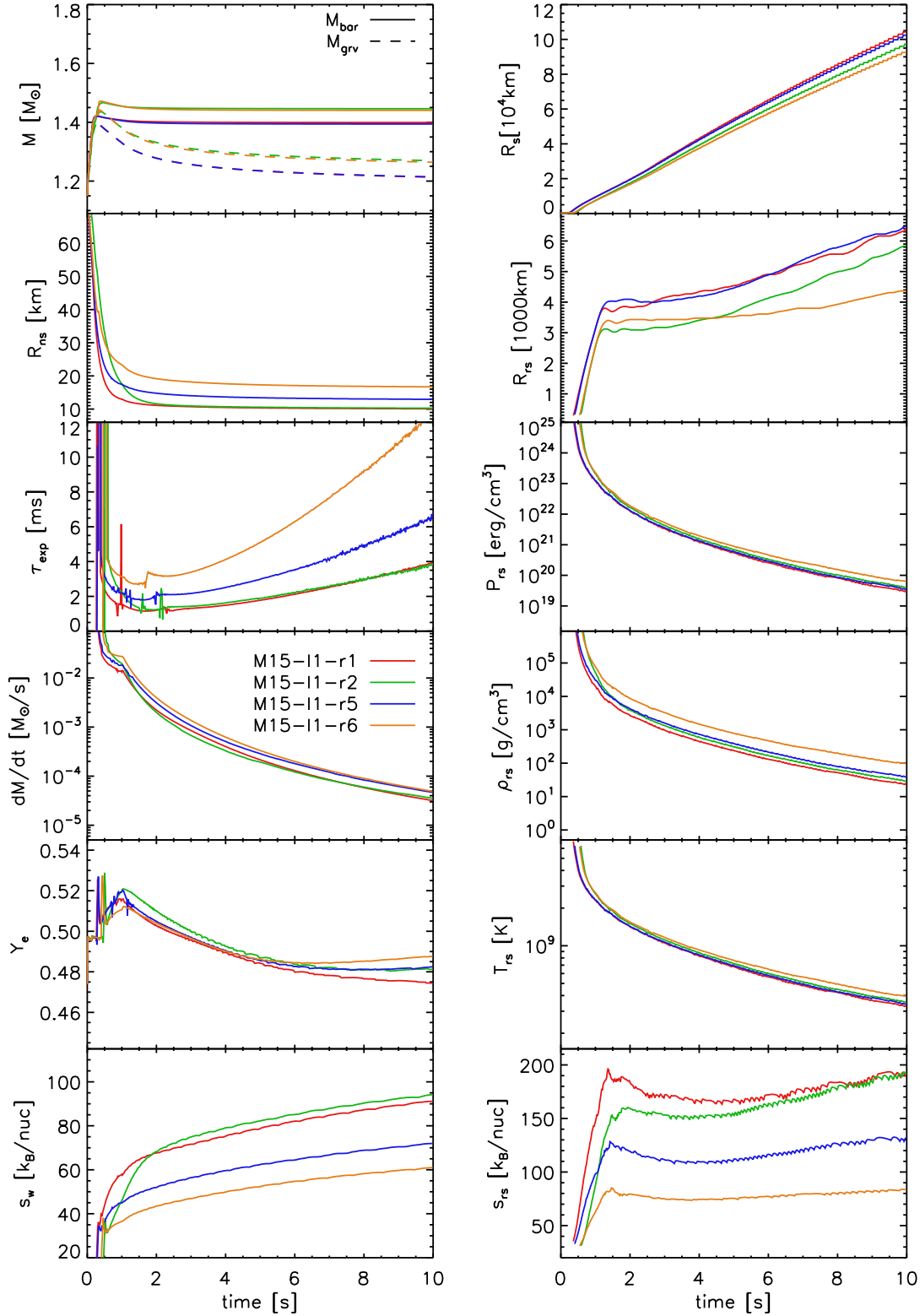


Figure 3.8: Time evolution of different quantities for a set of simulations with different neutron star contraction, M15-11-r1, M15-11-r2, M15-11-r5, and M15-11-r6. Shown are the baryonic mass, M_{bar} , and gravitational mass, M_{grv} (Eq. 2.11), neutron star radius, neutrino-wind expansion timescale according to Eq. (3.5), mass-loss rate, electron fraction, and entropy per nucleon (left, from top to bottom), radius of the supernova shock, radius of the reverse shock, and pressure, density, temperature, and entropy per nucleon downstream of the reverse shock.

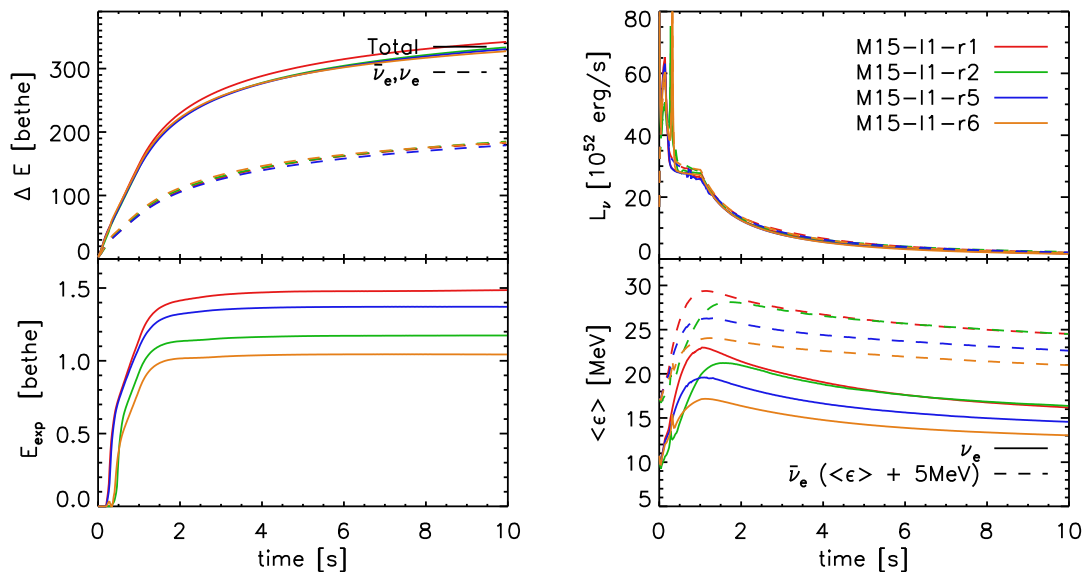


Figure 3.9: For a set of simulations with different neutron star contraction, M15-11-r1, M15-11-r2, M15-11-r5, and M15-11-r6 the different panels show as functions of time in the left column: the cumulative energy emitted in ν_e and $\bar{\nu}_e$, ΔE_{ν_e} and the total energy released in neutrinos and antineutrinos of all flavors, ΔE_{tot} (top), and the explosion energy of the models (bottom); and in the right column: the radiated luminosities of ν_e and $\bar{\nu}_e$ (top), the mean energies of these neutrinos (bottom)(all measured at a distance of 500 km, disregarding gravitational redshift effects).

Model M15-1t2-r3 demonstrates the influence of a more rapid decay of the luminosities and mean energies of the radiated neutrinos after one second of post-bounce evolution. This is associated with a reduced energy loss of the nascent neutron star and leads to an increase of the wind expansion timescale, a steep decrease of the wind mass loss rate, and a higher wind entropy compared to model M15-11-r1. The reverse shock reacts to that by a rapid recession between about 1 s and 3 s after bounce (cf. Eq. 3.18) before it starts an outward motion again at later times when the pressure P_{rs} drops faster than \dot{M}_w and u_w of the wind. Due to the small reverse shock radius, however, u_w at the shock is low and the entropy increase through the wind termination shock is modest.

Model M20-13-r3 with a neutron star radius and neutrino emission properties very similar to model M15-11-r1, but a significantly higher neutron star mass, reveals an even more extreme behavior. The larger neutron star mass increases the wind entropy, but at the same time reduces the wind mass-loss rate and the inverse wind expansion timescale (and thus the wind velocity; cf. Eqs. 3.6–3.8). Moreover, the explosion energy of this model is very low and the supernova shock expands only slowly. All together forces the wind termination shock to retreat as the neutrino fluxes decay, until it falls below the sonic point in the wind and disappears. This brings the whole region from the proto-neutron star surface to the outer boundary of the neutrino-driven outflow (which is the contact discontinuity between shock-accelerated ejecta and neutrino-heated ejecta) in sonic contact, see Fig. 3.12. The neutrino-driven outflow is now only a subsonic breeze and merges with the dense shell of ejecta behind the outgoing supernova shock without being accelerated to supersonic speed.

In order to study this phenomenon and its implications in more detail, we triggered the occur-

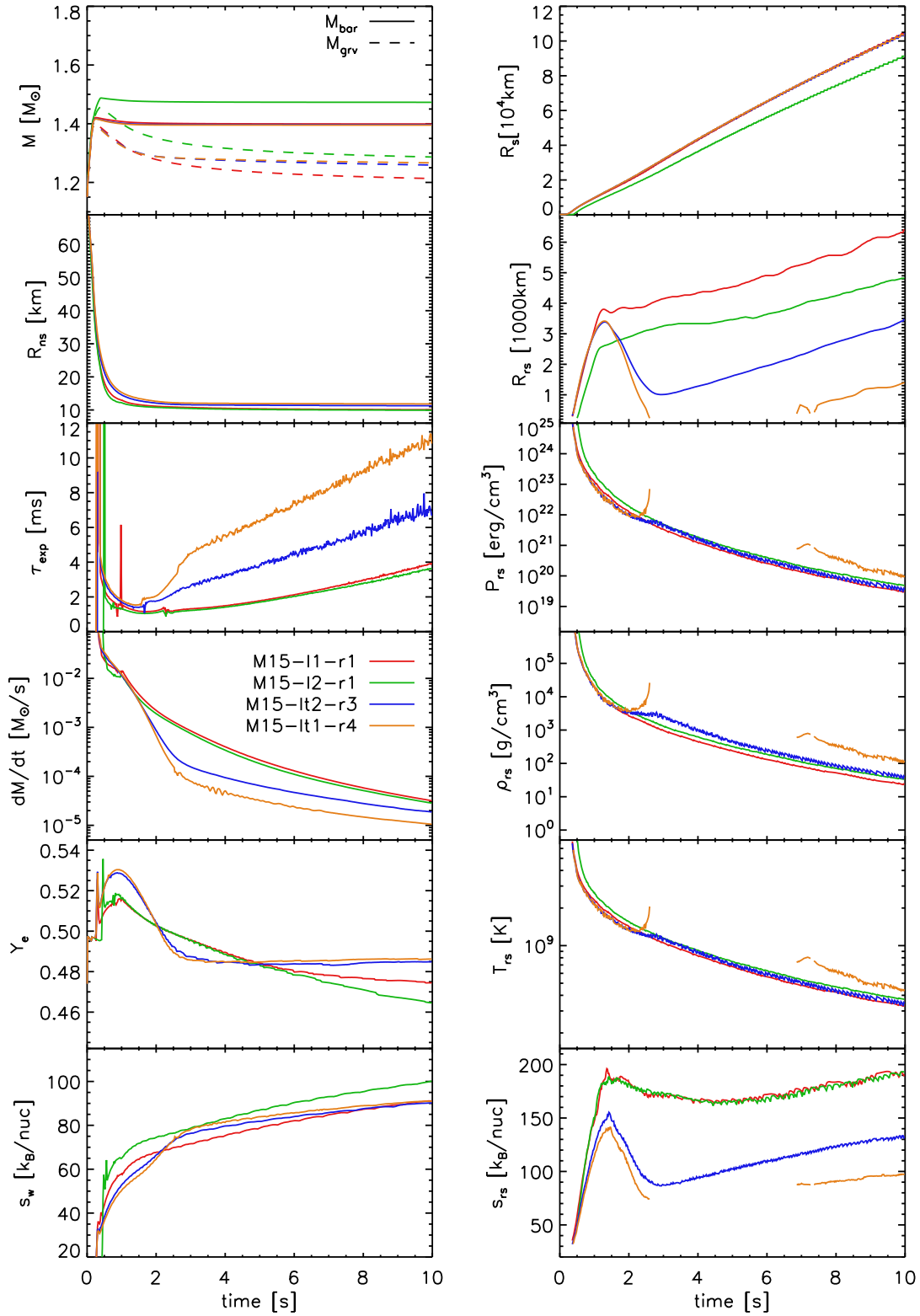


Figure 3.10: The same as Fig. 3.8, but for simulations with varied inner boundary conditions. The models M15-lt1-r4, M15-lt2-r3, and M20-l3-r3 are compared with our reference $15 M_{\odot}$ model M15-l1-r1 in order to demonstrate the influence of different core neutrino luminosities at the inner grid boundary.

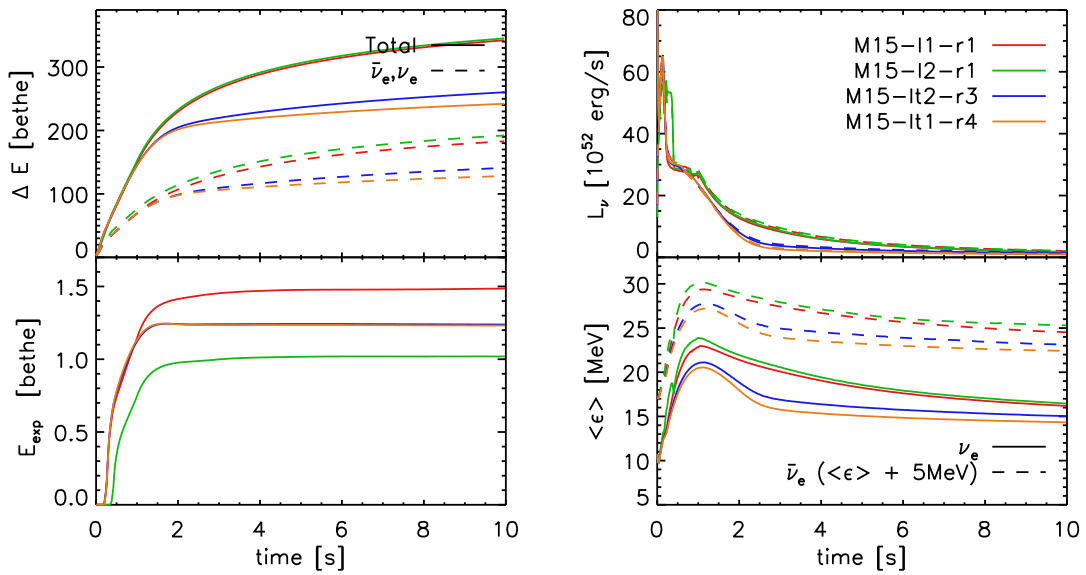


Figure 3.11: The same as Fig. 3.9, but for simulations with varied inner boundary conditions. The models M15-1t1-r4, M15-1t2-r3, and M20-13-r3 are compared with our reference $15 M_\odot$ model M15-11-r1 in order to demonstrate the influence of different core neutrino luminosities at the inner grid boundary.

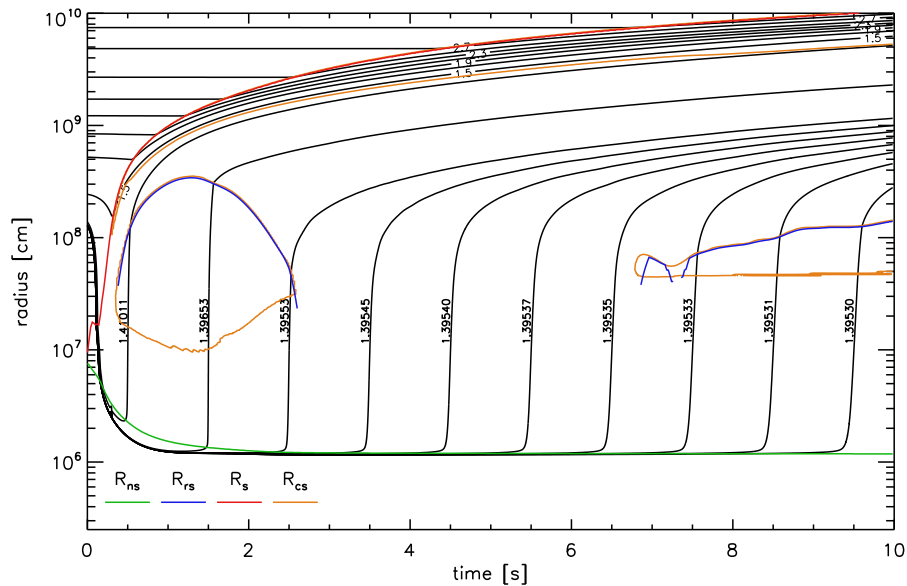


Figure 3.12: Same as Fig. 3.3, but for model M15-1t1-r4. Here the explosion occurs at 0.22 s after bounce and because of the assumed fast subsequent decay of the neutrino luminosity, the reverse shock reveals a much different behavior than in case of model M15-11-r1. It temporarily disappears when a subsonic breeze instead of a wind develops after about 2.5 s. At $t \gtrsim 7$ s the outflow expansion becomes supersonic again and a wind termination shock appears again.

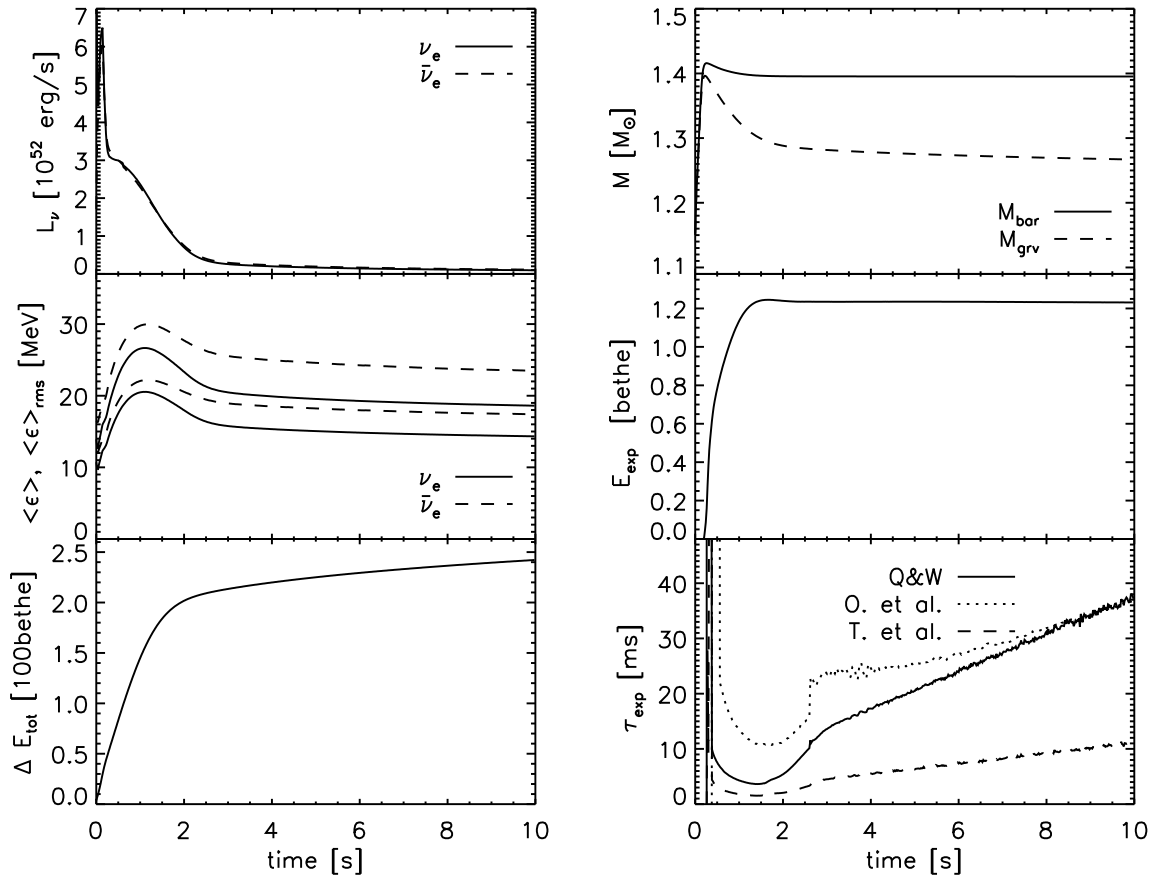


Figure 3.13: Same as Fig. 3.4, but for model M15-lt1-r4. Compared to model M15-l1-r1, the neutrino luminosities and mean energies decrease faster, the total energy radiated in neutrinos and the explosion energy are lower, and the gravitational mass of the neutron star is larger. The breeze solutions that develop between 2.5 s and 7 s have significantly longer expansion timescales.

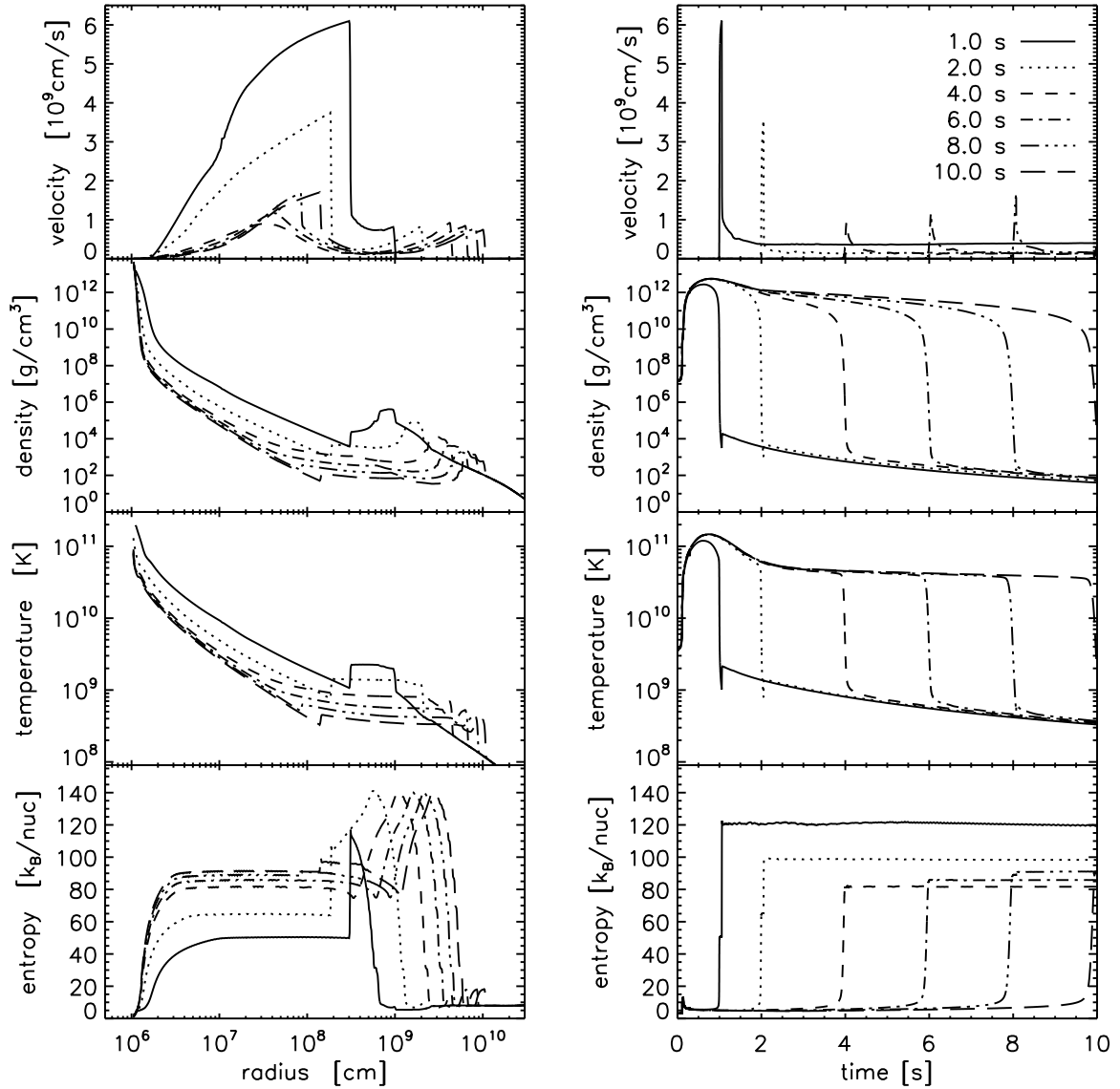


Figure 3.14: Left, from top to bottom: Radial profiles of the velocity, density, temperature, and entropy in model M15-lt1-r4 at different post-bounce times. The profiles should be compared with the corresponding ones of model M15-l1-r1 in Fig. 3.5. Right: The same quantities as functions of time for some mass shells ejected in the neutrino-driven outflow of model M15-lt1-r4. For comparison with Model M15-l1-r1, see Fig. 3.6.

rence of the breeze at a much earlier time in model M15-lt1-r4, in which the neutrino luminosities at the inner boundary were assumed to decay faster and the radiated neutrino energy is therefore even lower than in model M15-lt2-r3 (see Fig. 3.11). As a consequence, the neutrino wind does not have sufficient power to keep the wind termination shock at a large radius. In spite of a standard explosion energy ($E_{\text{exp}} \sim 1.2$ bethe; Table 3.2 and Fig. 3.13) and fast propagation of the supernova shock, the reverse shock begins to retreat already after 1 s and disappears after 2.5 s (Fig. 3.12) whereas this happens only after 7 s as in model M15-lt2-r3 (Fig. 3.10). Fig. 3.13 shows that the transition to the subsonic breeze is accompanied by a considerable growth of the expansion timescales calculated from Eqs. (3.3) and (3.5). The timescale calculated from Eq. (3.4) exhibits even a sudden increase which occurs when the wind termination shock has retreated so much that it is encompassed by the radial integral of Eq. (3.4). The integral then includes shock-decelerated outflow, which cools much more slowly.

After about 7 seconds, however, the sound speed in the neutron star surroundings has dropped and the dense ejecta shell behind the supernova shock has moved outward sufficiently far so that the neutrino-driven outflow can again reach supersonic velocities, despite of a much less powerful acceleration of the wind matter than in the first two seconds after bounce (Fig. 3.12). This is visible also in the radial profiles and mass shell trajectories plotted in Fig. 3.14, where at late times ($t \geq 8$ s) the discontinuity that characterizes the presence of a wind termination shock appears again in all quantities. Because of the low wind velocity and very low mass-loss rate and therefore small reverse-shock radius, at these late times, the shock is much weaker than it was in the early phase. The associated density, temperature, and entropy steps are consequently also smaller (Fig. 3.14).

During the breeze phase the outflow material is accelerated to a maximum velocity and then continuously decelerated again as it joins into the dense layer of ejecta behind the supernova shock. The mass-shell trajectories on the rhs. of Fig. 3.14 illustrate this smooth transition from the breeze expansion to the slower evolution when the matter is added to the dense ejecta shell.

Models M15-lt1-r4 and M20-l3-r3 demonstrate clearly that the wind termination shock can be a transient feature and its presence is very sensitive to the time-dependent conditions in the neutrino-driven outflow and the expansion of the dense postshock shell of supernova ejecta. Simulations with a consistent treatment of the neutron star evolution and of the baryonic mass loss of the nascent neutron star are needed to make predictions of the detailed evolution for a given progenitor star. But even then such predictions are constrained by our incomplete knowledge of the neutrino emission of forming neutron stars on the one hand and of the high-density equation of state and the associated neutron-star properties on the other.

3.6 Different progenitors

The analytic discussion of the previous section, in particular Eqs. (3.15), (3.17), and (3.18), allow us now to understand the behavior of the wind termination shock in different progenitor stars. For this purpose we compare our $15 M_{\odot}$ reference model, M15-l1-r1, with models M10-l1-r1, M20-l1-r1, and M25-l5-r4, which are explosion simulations for 10.2, 20, and $25 M_{\odot}$ stars, respectively. The conditions at the inner grid boundary were chosen such that the models have similar explosion energies between roughly 1.3 B and 2 B (Table 3.2). The $25 M_{\odot}$ star has such a big mass accretion rate and correspondingly high accretion luminosity that the explosion tends

to become stronger than in the lower-mass progenitors. To lessen this effect, we reduced the boundary luminosities compared to the other models and chose a larger final radius of the inner boundary and thus of the new-born neutron star.

The neutron star mass and radius in the 10.2, 15, and 20 M_{\odot} simulations are rather similar (Table 3.2) and so are the time-dependent luminosities, mean neutrino energies, and energy radiated in ν_e and $\bar{\nu}_e$, as well as the total energy release in neutrinos of all flavors, ΔE_{tot} , (Fig. 3.16). The 25 M_{\odot} run, however, sticks out with significantly higher values of all these quantities. Progenitor-dependent differences associated with the density structure of the collapsing star outside of the iron core are responsible for the differences in the time-dependence of the explosion energy for the 10.2, 15, and 20 M_{\odot} models displayed in the lower panel of Fig. 3.16. A more massive progenitor has a higher mass accretion rate and accretion luminosity and also a larger mass in the gain layer. Its explosion therefore tends to be more energetic. In case of the models M20-11-r1 and M25-15-r4, the large binding energy of the outer stellar shells later on leads to a visible decrease of the explosion energy from a maximum value reached transiently during the simulation (Fig. 3.16).

Figure 3.15 shows the time evolution of quantities that determine and characterize the neutrino wind and reverse shock behavior in our simulations with different progenitors. The wind properties (left column in Fig. 3.15) exhibit their well-known dependence on the neutron star mass and radius and on the neutrino luminosities and mean energies. Because of the similarity of these quantities in case of the 10.2, 15, and 20 M_{\odot} models, only rather small differences are visible between these runs, revealing a slightly longer expansion timescale, lower mass-loss rate, and higher entropy for model M20-11-r1 with its more massive neutron star (see also Table 3.2). The electron fraction shows a somewhat wider variation because of its strong sensitivity to the spectral and flux differences of the ν_e and $\bar{\nu}_e$ emission. The large neutron star mass and neutrino luminosities in case of the 25 M_{\odot} progenitor separate this model clearly from the others. They affect in particular the neutrino-wind entropy, which scales with the value of the neutron star mass but is only weakly dependent on the neutrino emission properties (Eq. 3.6). In contrast, the expansion timescale and mass loss rate are similar to the other models because of a partial cancellation of their dependencies on L , ϵ , and M in Eqs. (3.7) and (3.8).

The wind termination shock evolves largely differently in all cases (Fig. 3.15, right column). Obviously, the progenitor structure has a big influence on its behavior. The supernova shock expands much faster in the lower-mass stars, causing a more rapid decline of the pressure in the shell between forward and reverse shock. The propagation of the forward shock and the time-varying conditions there are communicated inward to the reverse shock on the sound propagation timescale. Therefore the pressure just downstream of the reverse shock, P_{rs} , as well as the density and temperature at this location, decrease, too. From Eq. (3.18) it can be understood that in model M10-11-r1 the strong pressure reduction triggers a fast outward motion of the reverse shock. In the 15 M_{\odot} star the increase of R_{rs} is much less extreme, and in the 20 and 25 M_{\odot} runs the wind termination shock even retreats after ~ 2 s of initial expansion and transient stagnation. In these cases the decline of P_{rs} is not fast enough to compete with the decrease of \dot{M}_{w} and u_{w} in the numerator of Eq. (3.18). A similar effect can be observed at $t = 1$ s when we change the time-dependence of the neutrino luminosity at the inner grid boundary. The subsequent luminosity decrease leads to the mass-loss rate and velocity of the wind dropping more quickly than P_{rs} in all models except M10-11-r1, explaining why the initial expansion of the reverse shock is stopped at about this time.

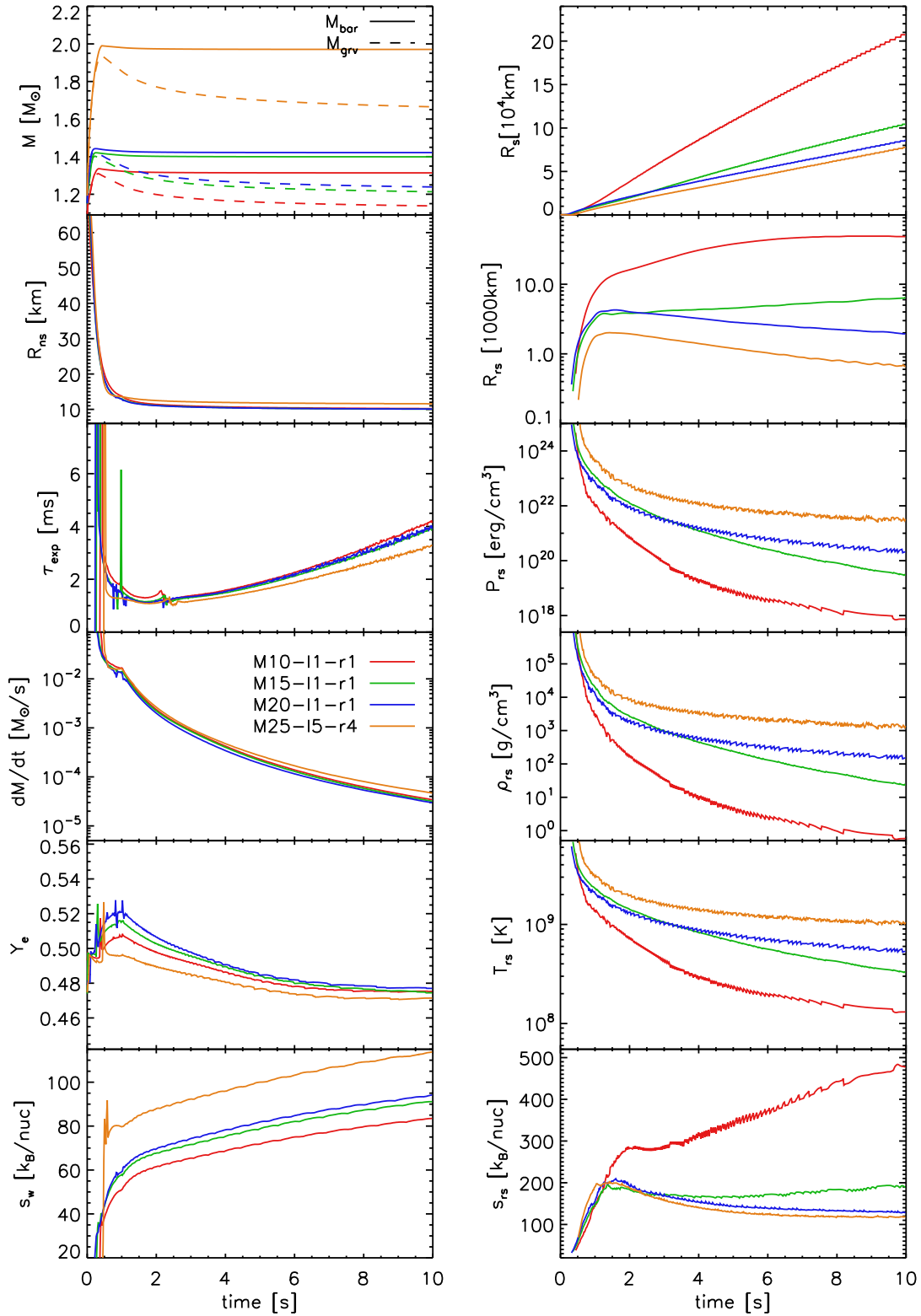


Figure 3.15: The same as Fig. 3.8, but for simulations with varied progenitor star. The models M10-11-r1, M20-11-r1, and M25-15-r4 are compared with our reference $15 M_{\odot}$ model M15-11-r1.

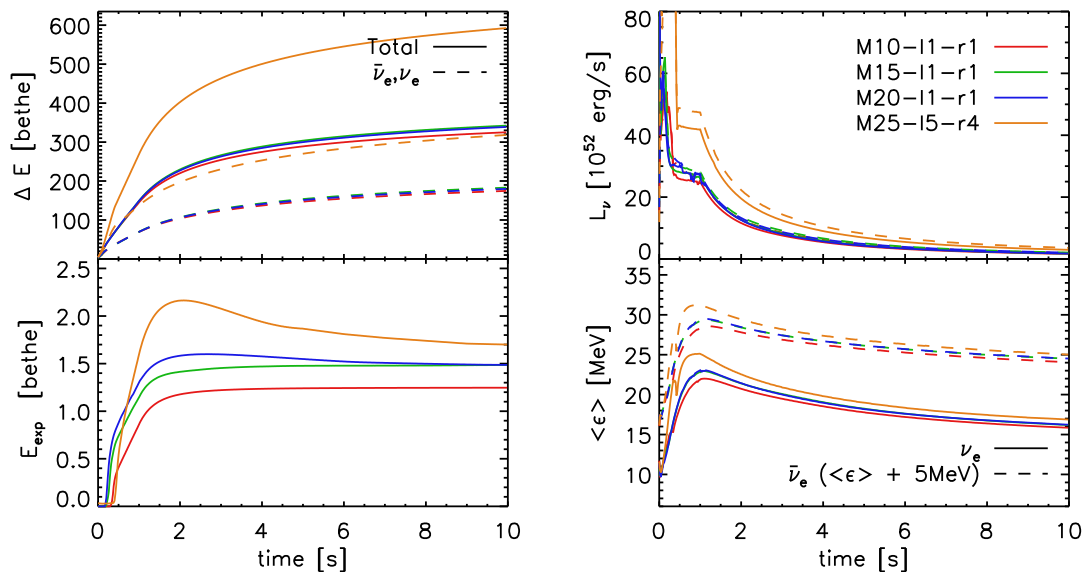


Figure 3.16: The same as Fig. 3.9, but for simulations with varied the progenitor star. The models M10-11-r1, M20-11-r1, and M25-15-r4 are compared with our reference $15 M_{\odot}$ model M15-11-r1.

Because of the different reverse shock behavior, the density, temperature, and entropy downstream of the reverse shock as functions of time show also large differences between the progenitors (Fig. 3.15). In model M10-11-r1 the wind termination shock moves to radii beyond 10,000 km within little more than one second. During this phase the density ρ_w behind this shock drops to less than 10^3 g cm^{-3} and the temperature T_w becomes lower than 10^9 K . The entropy, on the other hand, is nearly $300 k_B$ per nucleon after 2 seconds. In the runs for the more massive progenitors, the density and temperature at the reverse shock are larger for a longer period of postbounce evolution, and the entropy does not reach the very high values of the $10 M_{\odot}$ simulation. The more massive the progenitor is — or, more precisely, the denser the shells around the iron core are — the slower propagates the shock for a given value of the explosion energy, and the more confined is the reverse shock. In none of the compared cases, however, are the conditions at the wind termination shock constant with time.

3.7 Summary

The most important results of the one-dimensional simulations can be summarized as follows:

- The basic properties of the wind termination shock which forms when the outflow becomes supersonic, can be understood from simple analytic considerations using the shock-jump conditions at this reverse shock. The entropy of the shock-decelerated matter increases with the wind velocity and is lower for high wind density. Therefore a large reverse shock radius is favorable for a high entropy jump. The reverse shock radius increases with the mass-loss rate and velocity of the wind, but decreases when the pressure behind the reverse shock is high. The latter dependence links the behavior of the reverse shock to the propagation of the supernova shock and thus to the progenitor structure and the explosion properties.

- The conditions at the reverse shock are progenitor-dependent and usually strongly time-dependent and therefore the shock effects are not well represented by an outer boundary condition with constant pressure (e.g., Sumiyoshi et al. 2000) or constant temperature (e.g., Wanajo et al. 2002). The conversion of kinetic energy to internal energy in the wind termination shock can raise the entropy to several times the wind entropy. We find the highest values of more than $400 k_B$ per nucleon behind the reverse shock (more than a factor of five increase) — but also the lowest temperatures ($\lesssim 10^9$ K) and densities ($\lesssim 1000 \text{ g cm}^{-3}$) — in case of the considered $10 M_\odot$ progenitor. In this star the supernova shock and the reverse shock propagate outward very rapidly. In the considered progenitors with masses of more than $15 M_\odot$ the maximum entropies are more than $200 k_B$ per nucleon, corresponding to an increase of roughly a factor of three, with densities and temperatures behind the reverse shock in the first ten seconds of typically $100\text{--}10^4 \text{ g cm}^{-3}$ and $0.4\text{--}2 \times 10^9$ K, respectively.
- When the supernova shock expands slowly or the neutrino emission from the nascent neutron star decays rapidly and the wind power thus drops quickly, the reverse shock can show phases of recession and can even reach the sonic point in the wind and vanish. The outflow then becomes a subsonic breeze that merges smoothly with the ejecta shell behind the shock without any jumps in the velocity and in the thermodynamic quantities. Changing conditions around the neutron star can lead to a re-establishment of a supersonic wind at later times.

4

Results for two-dimensional models

In the previous chapter we have shown that the reverse shock could play an important role for nucleosynthesis because it is able to increase the entropy and to change the evolution of density and temperature. As discussed in Sect. 3.4, the value that the entropy can reach and the position of the reverse shock depend not only on the neutrino wind, which for non-rotating neutron stars, is spherical and can be studied by one-dimensional simulations, but it is also influenced by the pressure in the preceding ejecta. Multi-dimensional effects (e.g. convection, downflows, instabilities) modify the pressure distribution and can destroy the reverse shock or change its shape and position, which could also have influence on the nucleosynthesis. A detailed analysis of the behavior of the reverse shock in two dimensions is the goal of this chapter. For this purpose we have performed several simulations that are summarized in Sect. 4.1. A detailed analysis is done for one model in Sect. 4.2, and interpreted using analytic derivations in Sect. 4.3. Models based on the same progenitor star but with different boundary luminosities and ejecta morphologies are briefly discussed in Sect. 4.4, and models based on different progenitor stars are addressed in Sect 4.5. One- and two-dimensional simulation are compared in Sect. 4.6.

4.1 The computed models

Two-dimensional simulations are computational significantly more expensive than one-dimensional ones. Therefore it was not possible to calculate a similar number of models and run the simulations as long as in the case of the one-dimensional models of Chapter 3. A list of our 2D models with their characterizing parameters is given in Table 4.1. The names of the models start with “T” to denote two dimensions. The rest of the name has the same meaning as in one-dimensional simulations (see Sect. 3.1). The name extensions “11”, “12” corresponds to different boundary luminosities. The contraction parameters (Eq. 2.30) are also given in Table 4.1, and different values are indicated by “r1”, “r0”, “r4” in the name of the model. There are also simulations for different progenitor stars (Table 2.1) with the masses indicated in Table 4.1. The initial models are the same as in the one-dimension simulations. However, since

Table 4.1: Model parameters of our two-dimensional simulations. The different models are characterized by the chosen contraction of the inner grid boundary, which is expressed in terms of the final radius R_f and the exponential contraction timescale t_0 (cf. Eq. 2.30). In addition, different initial luminosities of ν_e plus $\bar{\nu}_e$ (measured in bethe [B] = 10^{51} erg per second) are imposed at the inner grid boundary.

Model	Contraction (R_f, t_0)	$L_{\nu_e}^{\text{ib}} + L_{\bar{\nu}_e}^{\text{ib}}$ [B/s]	Progenitor Mass [M_\odot]
T15-11-r0	8 km; 0.1 s	52.5	15
T15-11-r1	9 km; 0.1 s	52.5	15
T15-12-r1	9 km; 0.1 s	38.6	15
T10-11-r1	9 km; 0.1 s	52.5	10
T10-12-r1	9 km; 0.1 s	38.6	15
T25-15-r4	10.5 km; 0.1 s	30.3	25

this initial configuration is spherically symmetric, i.e. isotropic, and our code conserves this symmetry, it is necessary to add random perturbations to the velocity field (with an amplitude of typically 0.1 %) to allow for hydrodynamic instabilities like convection (for more details see Scheck et al. 2006, Scheck 2006). As we reported on the effects of varying boundary conditions (contraction, neutrino luminosity) already in Chapter 3, we will now focus on the impact of two-dimensional effects.

The evolution of the reverse shock (and its effect on the maximum entropy value and on the temporal variation of density and temperature) depends on the interaction of the neutrino-driven wind with the slower-moving preceding ejecta. The wind is spherically symmetric because the neutrino emission is isotropic. Varying boundary conditions, i.e. contraction, neutrino luminosity, affects the wind properties in the same way as in 1D (Sect. 3.5). However, the ejecta are strongly influenced by multidimensional effects, as hydrodynamic instabilities lead to a pronounced anisotropy of the explosion. These important effects are not modelled in one-dimensional simulations. Furthermore, the anisotropy varies strongly with the neutrino luminosity at the inner boundary during the first hundreds of milliseconds of the explosion and even depends in a chaotic way on the initial random perturbation. Therefore a single two-dimensional simulation is not sufficient to clarify the influence of multidimensional effects — several models with different initial and boundary conditions are required.

The enhancement of neutrino heating due to convection has a direct consequence on the explosion: for the same inner boundary parameters, it occurs earlier than in 1D and is more energetic. As there is less time for the neutron star to accrete matter, a process that is basically stopped once the explosion has set in, the neutron star masses are smaller in two dimensions. This results also in different wind and reverse shock properties. To find a two- and a one-dimensional model with the same wind properties is therefore non-trivial.

In order to organize the two-dimensional discussion, we will first analyze a reference case in detail, and then discuss the other models of Table 4.1 briefly.

Table 4.2: Results of the 2D models at one second after bounce. The end of the simulation is denoted by the time t_{end} given in seconds after bounce. M_{bar} is the baryonic mass of the neutron star. The neutron star radius is R_{ns} is defined as the location where the density is $10^{11} \text{ g cm}^{-3}$. ΔE_{tot} is the total energy radiated in neutrinos of all flavors (measured in bethe [B] = 10^{51} erg), L_{ν_e} and $L_{\bar{\nu}_e}$ are the luminosities of electron neutrinos and antineutrinos measured at 500 km, $\langle \epsilon_{\nu_e} \rangle$ and $\langle \epsilon_{\bar{\nu}_e} \rangle$ are the corresponding mean energies, E_{exp} is the explosion energy, t_{exp} is the post-bounce time when the explosion sets in (defined as the moment when the energy of expanding postshock matter exceeds 10^{49} erg).

Model	t_{end} [s]	M_{bar} [M_{\odot}]	ΔE_{tot} [100B]	R_{ns} [km]	L_{ν_e} [B/s]	$L_{\bar{\nu}_e}$ [B/s]	$\langle \epsilon_{\nu_e} \rangle$ [MeV]	$\langle \epsilon_{\bar{\nu}_e} \rangle$ [MeV]	E_{exp} [B]	t_{exp} [s]
T15-11-r0	2.0	1.393	1.460	12.79	25.53	26.45	22.68	24.04	1.364	0.156
T15-11-r1	1.0	1.388	1.461	13.27	27.66	28.22	22.55	23.87	1.341	0.162
T15-12-r1	1.5	1.421	1.228	12.76	22.60	23.23	22.27	23.75	1.405	0.184
T10-11-r1	2.8	1.261	1.305	14.82	22.97	24.63	20.51	22.10	1.457	0.153
T10-12-r1	2.2	1.280	1.146	13.44	21.76	22.49	21.36	22.91	0.938	0.170
T25-15-r4	1.6	1.869	2.233	13.41	36.46	39.92	24.31	25.51	3.674	0.197

4.2 Evolution of a reference case in two dimensions

In this section we describe the evolution of Model T15-11-r0 (see Table 4.1) giving a brief overview of how the explosion develops in presence of convection and showing how the wind evolves in 2D. It is not our aim to analyse the origin of the anisotropies (see Scheck et al. 2006; Scheck 2006; Scheck et al. 2007 for discussion of this issue), but to study how they influence the later interaction between the wind and the slower-moving ejecta. We have chosen Model T15-11-r0 as a reference case because it presents standard values for an explosion of a $15 M_{\odot}$ progenitor, i.e. at 2 s after bounce it has an explosion energy of $\sim 1.6 \text{ B}$, the neutron star contracts to a radius of $\sim 10 \text{ km}$ and obtains a baryonic mass of $\sim 1.4 M_{\odot}$.

The entropy distribution for different times is shown in Fig. 4.1. At the beginning the distribution is spherical symmetric, except for small random seed perturbations. However, when the neutrinos start to deposit energy behind the shock a negative entropy gradient establishes in this region. The layer between neutron star and shock becomes thus Ledoux-unstable¹ and develops a convective overturn. In the first panel ($t = 100 \text{ ms}$ after bounce) one can distinguish, in the left side (region between $\theta = \pi/2$ and $\theta = \pi$), Rayleigh-Taylor “mushrooms”, which start to grow from the initial perturbations. The buoyant bubbles merge and rise up, disturbing the shock shape. Neutrino-heated matter with high entropy streams upwards, while downflows transport low entropy matter from the shock to the neutron star (see Fig. 4.1 panel for $t = 150 \text{ ms}$), where it is decelerated and spread around the neutron star. The downflows and rising bubbles evolve quickly on time scales of the order of 10 ms. These convective structures and the associated shock deformations are characterised by increasingly large angular scales. Eventually the mass

¹ In the Ledoux approximation, convective instabilities arise when a displaced fluid element of constant entropy and electron fraction, maintaining pressure equilibrium with its surroundings, experiences buoyancy forces which tend to amplify its displacement. In this case the criterion for convective instability is given by

$$\frac{dS}{dr} \left(\frac{\partial \rho}{\partial S} \right)_{Y_e, P} + \frac{dY_e}{dr} \left(\frac{\partial \rho}{\partial Y_e} \right)_{S, P} > 0.$$

distribution below the shock is highly anisotropic and dominated by low modes. In this phase persistent neutrino-heating in the post-shock layer, aided by convection, finally leads to the onset of the explosion: The matter in the gain layer becomes unbound and moves outwards behind the accelerating shock.

After the onset of the explosion the evolution becomes slower, and the shock and the ejecta expand quasi-self-similarly (see Fig. 4.1 panel for $t \geq 300$ ms). This “freeze-out” of the morphology occurs when a large bubble in the southern hemisphere (left side in Fig. 4.1) has pushed the shock further out. This hemispheric asymmetry is visible until the end of the simulation. At 400 ms there is still a downflow present near the equatorial plane which continuously accretes matter onto the neutron star. However, in the following a neutrino-driven wind forms around the neutron star and blows this last downflow away (see panel for $t = 500$ ms). Like in the one-dimensional simulations the wind material is accelerated to velocities that are supersonic in the frame of the slower-moving ejecta further out, which leads to the formation of a reverse shock. The wind depends on the spherical neutrino emission, therefore the region between the neutron star and the reverse shock evolves as in one-dimensional models (Chapter 3).

The local radius of the reverse shock is angle-dependent since the layer between reverse shock and shock has developed a very anisotropic matter distribution. At $t = 0.4 - 0.5$ s one can see how the reverse shock expands faster in the southern hemisphere, i.e. negative z -axis, where also the ejecta have moved out farther. In contrast, high density regions in the ejecta, which are the remainders of former downflows blown away by the wind, present obstacles that prevent a fast reverse shock expansion (Fig. 4.2). The most prominent of these regions is located near the equatorial plane. In the analytic discussion of the last Chapter (Sect. 3.4) we found (Eq. 3.18) that the reverse shock position is proportional to the pressure, mass outflow rate and wind velocity, i.e.

$$R_{\text{rs}} \propto \sqrt{\frac{\dot{M}_w u_w}{P_{\text{rs}}}}. \quad (4.1)$$

Since the mass outflow rate, \dot{M}_w , and the wind velocity, u_w , are similar for every angle, due to the spherical-symmetry of the wind, the angular dependence comes from the behavior of the pressure above the shock, P_{rs} . In the regions where the pressure is higher the reverse shock radius has a lower value (see Fig. 4.4).

Figure 4.3 shows the velocity, pressure and entropy radial profiles for two angles, which correspond to the red and green lines in Fig. 4.2. From these profiles one can see that the behavior of the flow between neutron star and reverse shock is the same as in 1D (see Fig. 3.5): the neutrinos heat the matter, which can expand quickly since the density is low, the velocities becomes supersonic and approaches an asymptotic value. The variation of the reverse shock radius with angle does not affect much to the maximum value that the velocity can reach. The reason for this is that for large radii the velocity increases only slowly towards the asymptotic value. Another remarkable feature appears in the red line of the velocity profile which goes through the, above mentioned, high-density region: just outside of the reverse shock the velocities are almost zero. This indicates that there was a dense downflow in this region before, which delayed and hampered the expansion into this direction, leading to a low velocity outflow and higher pressure values. The later has a direct influence (Eq. 4.1) on the reverse shock position, as we have already shown in Fig. 4.4 and explained above. Moreover, in the pressure jump the value corresponding to the wind pressure can vary significantly depending on the position of

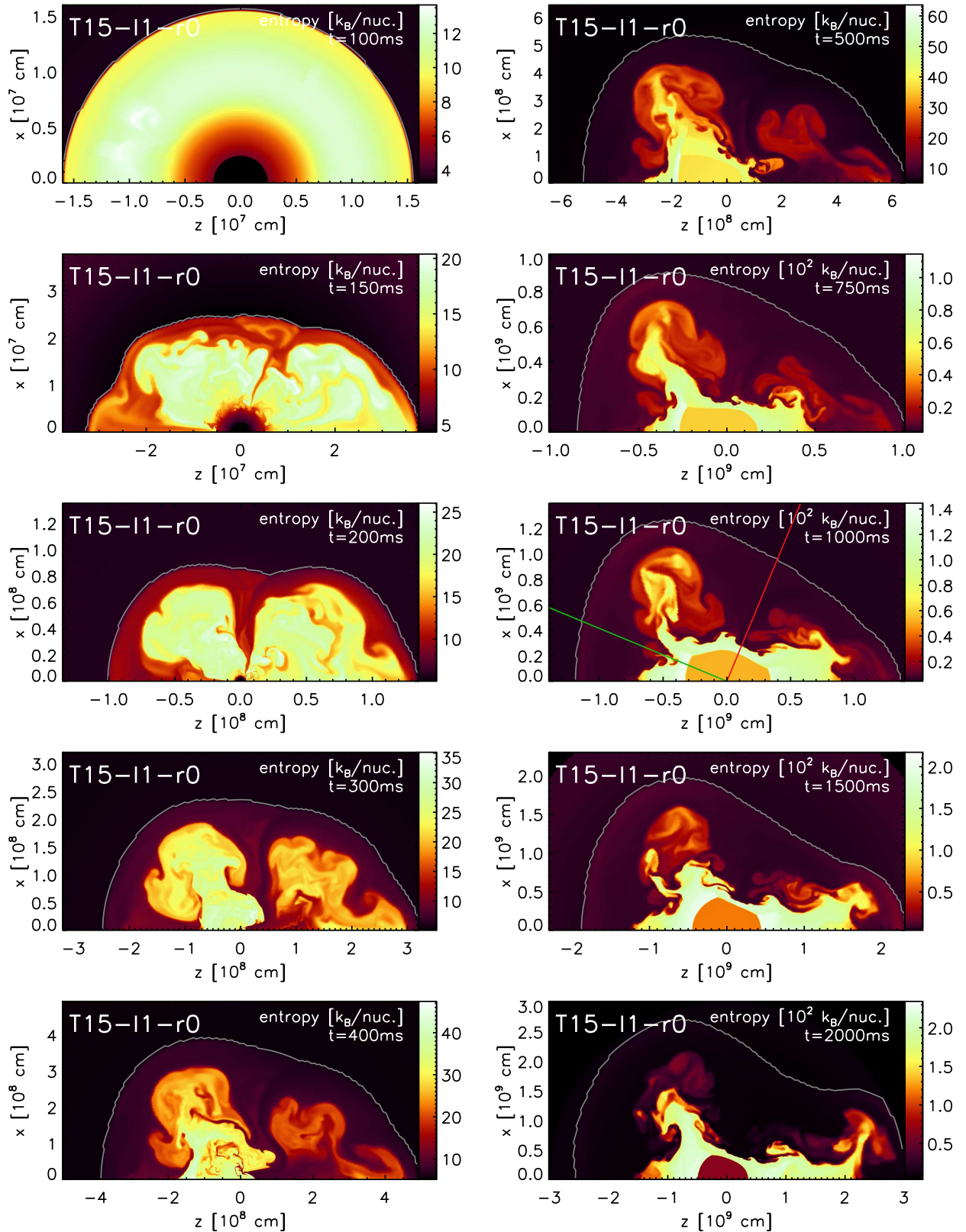


Figure 4.1: Entropy distribution in Model T15-11-r0 for different times. The figures are plotted such that the polar axis is orientated horizontally with “south” ($\theta = \pi$) on the left and “north” ($\theta = 0$) on the right. The grey line marks the shock radius. Note that the scales differ between plots. The red and green lines in the 1000 ms panel mark selected angles, which will be used to show the evolution of shocked material properties in Sect. 4.6.

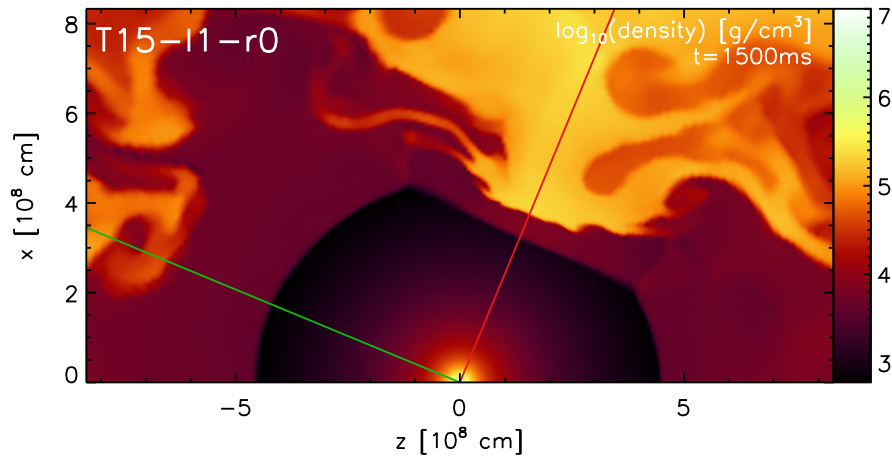


Figure 4.2: Density distribution in Model T15-11-r0 for $t = 1.5$ s. Only the inner part is plotted to show that the reverse shock radius is smaller when an obstacle (high density region) is present. The red and green lines mark selected angles, along which the radial profiles for different quantities are given in Fig. 4.3.

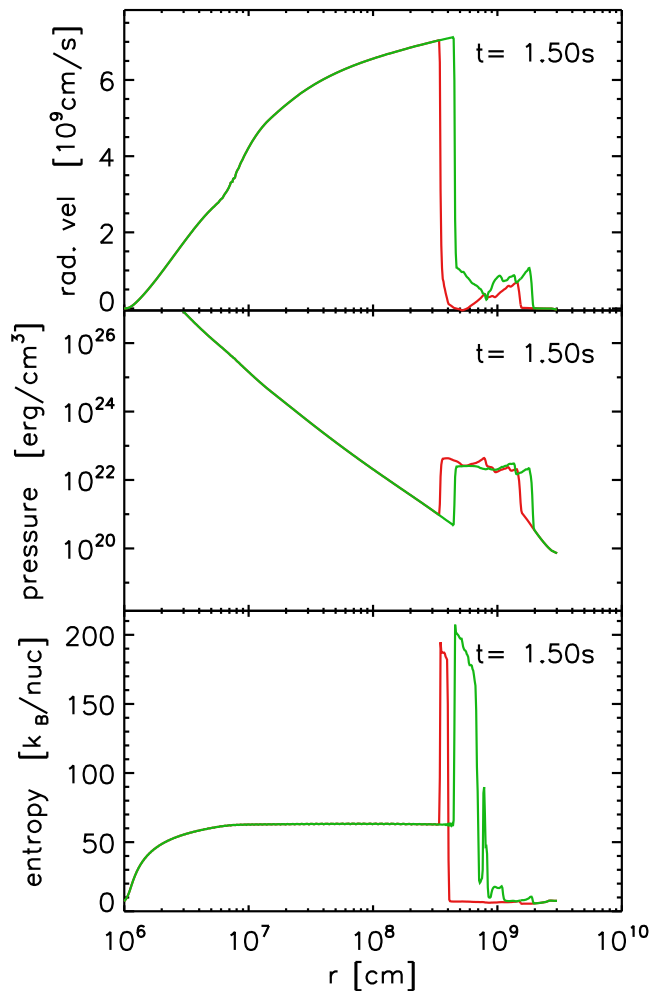


Figure 4.3: Radial profiles of the velocity, pressure and entropy for Model T15-11-r0 at $t = 1.5$ s. The red and green line correspond to two different angles, which are indicated with the same color in Fig. 4.2.

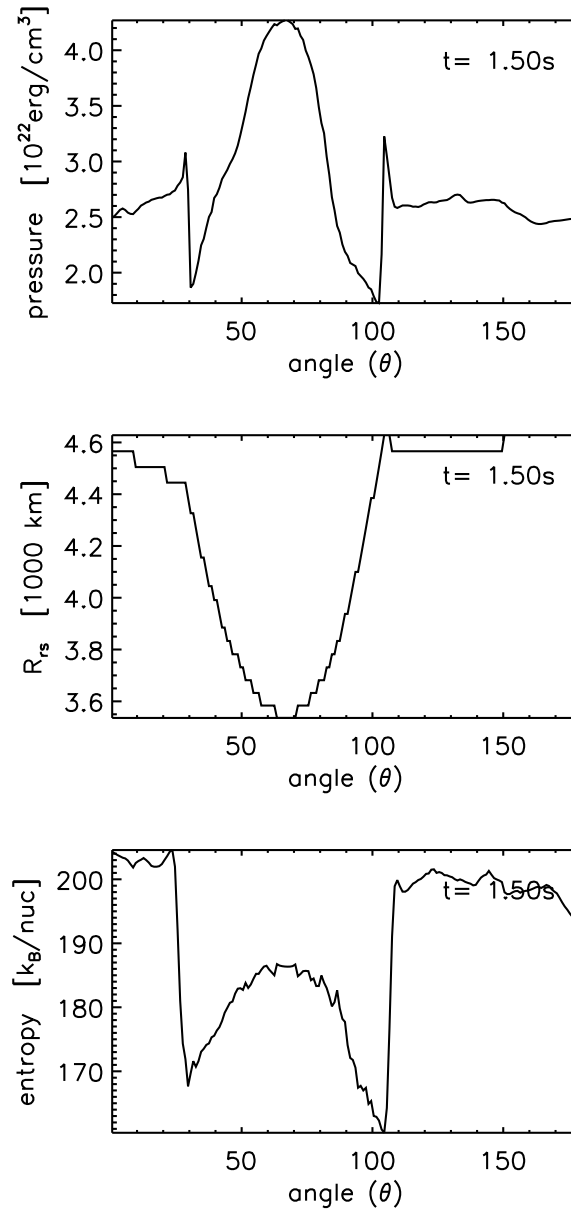


Figure 4.4: Angular variation of the pressure, radius and entropy at the reverse shock for the reference model at $t = 1.5$ s.

the reverse shock. This is because, unlike the wind velocity, the pressure does not approach a constant value. The pressure jump can be also used to calculate the angle between reverse shock and wind velocity (Sect. 4.3).

As visible in Fig. 4.3, the entropy increases in the region where the neutrinos deposit energy near the neutron star, remains constant in the wind further out and shows a jump at the reverse shock. All these features are the same as in one-dimensional simulations (see Fig. 3.5). However, the anisotropic distribution of the ejecta in the layer between reverse shock and shock leads to an angle dependence of the entropy jump. Figure 4.4 shows the entropy value of the shocked material just above the reverse shock as a function of the azimuthal angle. The entropy jump depends on the reverse shock position (roughly $s_{rs} \propto \sqrt{R_{rs}}$), however, in Fig. 4.4 the reverse

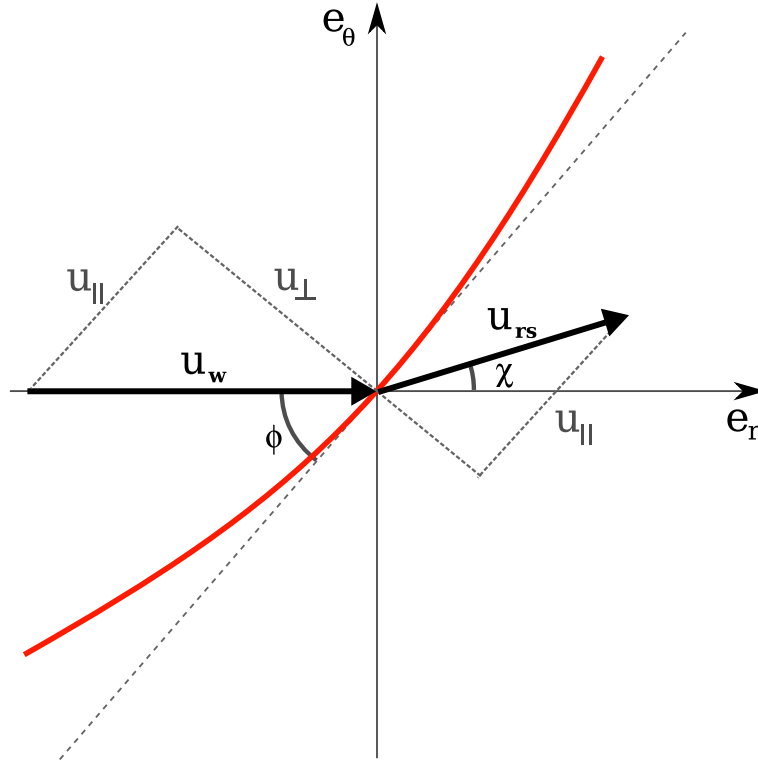


Figure 4.5: Schematic representation of the velocities in a fluid going through an oblique shock (red line). Only the velocity component perpendicular to the shock, u_{\perp} , is changed when a mass element crosses the shock – the parallel component is conserved. Therefore, the direction of the flow is changed at the shock.

shock radius has a minimum at $\theta \approx 65$, while the entropy has a local maximum. The reason for this is that the entropy also depends on the wind velocity (see Eq. 3.17), or, more precisely, on the component of the velocity that is perpendicular to the shock. And this component is larger at the angle where the entropy has a local maximum. The angular dependence is explained in more detail in the following section.

4.3 Analytic discussion: angular dependence

In this section we study the angular dependence that enters in the Rankine-Hugoniot conditions in the case of an oblique shock (Landau & Lifshitz 1959). Figure 4.5 shows a schematic representation of what happens in an oblique wind termination shock: The wind expands in radial direction with a velocity u_w and hits the shock at an angle ϕ .

The tangential component of the velocity, u_{\parallel} is continuous through the shock, i.e.:

$$u_w \cos \phi = u_{rs,r} \cos \phi + u_{rs,\theta} \sin \phi . \quad (4.2)$$

where the velocities of the rhs,

$$u_{rs,r} = u_{rs} \cos \chi , \quad (4.3)$$

$$u_{rs,\theta} = u_{rs} \sin \chi , \quad (4.4)$$

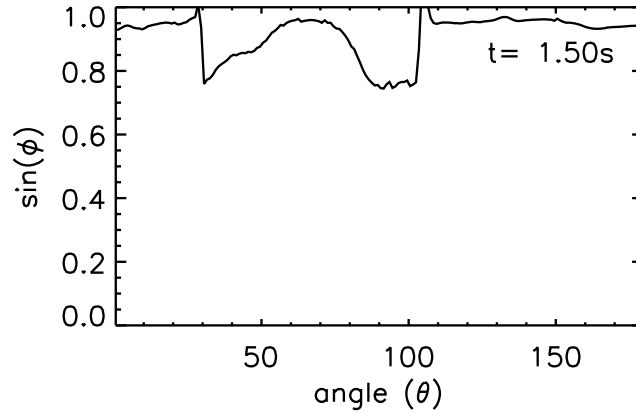


Figure 4.6: Result of plugging numbers in Eq. 4.7 for Model T15-11-r0 at $t = 1.5$ s. Using this equation $\sin \phi$ can be approximately calculated for every angular beam, i.e. for every θ .

are the radial and tangential reverse shock velocity components (see Fig. 4.5).

On the other hand, the component of the velocity, u_{\perp} , which is perpendicular to the shock, is the one that enters in the Rankine-Hugoniot conditions, Eqs. (3.9) – (3.11). The mass conservation equation, Eq. (3.9), including the angle can be rewritten as:

$$\rho_w u_w \sin \phi = \rho_{rs} u_{rs,r} \sin \phi + \rho_{rs} u_{rs,\theta} \cos \phi. \quad (4.5)$$

The momentum continuity equation, Eq. (3.10), for an oblique shock is:

$$P_w + \rho_w u_{w,\perp}^2 = P_{rs} + \rho_{rs} u_{rs,\perp}^2 \quad (4.6)$$

where only the perpendicular component of the velocity has to be considered. One can write this equation in terms of the angle ϕ ,

$$\Delta P = \rho_w u_w^2 \sin^2 \phi \left(1 - \frac{1}{\beta} \right), \quad (4.7)$$

where ΔP is the pressure jump at the reverse shock, u_w is the radial velocity (Fig. 4.5), and β is given by the density or velocity jump,

$$\beta = \frac{\rho_{rs}}{\rho_w} = \frac{u_{w,\perp}}{u_{rs,\perp}} = \frac{u_w \sin \phi}{u_{rs,r} \sin \phi + u_{rs,\theta} \cos \phi}. \quad (4.8)$$

Equation (4.7) indicates that the sine of the angle ϕ is smaller when the pressure jump is also smaller, while ϕ tends to $\pi/2$, i.e. the wind velocity is perpendicular to the reverse shock, at those angles where the jump ΔP is larger. The angle ϕ can be directly related to the jump in the pressure because in the wind ρ_w and u_w have the same value for every angular beam at a given radius, and the product $\rho_w u_w^2$ does not change much for different positions of the reverse shock because of the asymptotic behavior of the velocity (Fig. 4.3). We plug numbers for the pressure jump, wind velocity and density in Eq. (4.7), assuming $\beta = 7$. For doing that we use again the references case, i.e. Model T15-11-r0 (Sect. 4.2), at 1.5 s after bounce. Fig. 4.6 shows the value of the $\sin \phi$ as a function of the azimuthal angle θ . There are angles where the

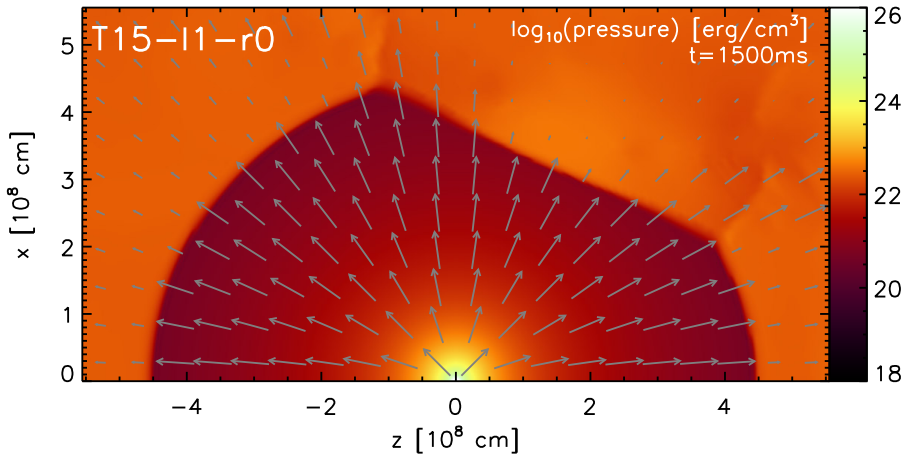


Figure 4.7: Pressure distribution in Model T15-11-r0 for $t = 1.5$ s. The arrows mark the velocity field. Only the inner part is plotted to show the effect of the reverse shock on the velocity.

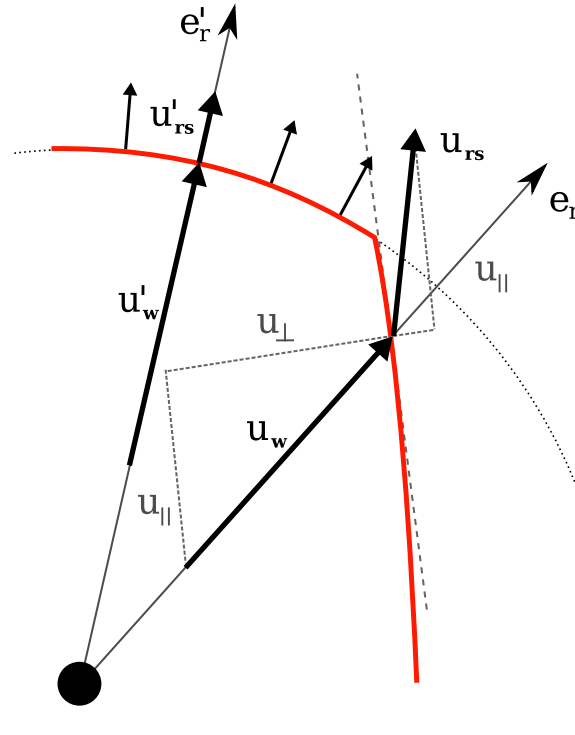


Figure 4.8: Schematic representation of the velocities in a fluid going through the reverse shock (red line) where a kink leads to the collimation of the outflowing matter.

velocity is perpendicular to the reverse shock, as Fig. 4.7 shows, here the arrows represent the velocity field and the pressure is given by the color scale. However, the value of $\sin \phi$ is never one because of simplifications of assuming $\beta = 7$ and not taking into account the velocity of the reverse shock. The velocity entering in the Rankine-Hugoniot conditions (Eq. 4.7) is the fluid velocity in the frame of the reverse shock, u_{rs} , and we are using the fluid velocity in the frame of the neutron star, v_{rs} . Therefore, if the reverse shock expansion is very rapid and anisotropic these two velocities are not exactly the same, but $u_{rs} = v_{rs} - \dot{R}_{rs}$ with \dot{R}_{rs} being the velocity of the reverse shock in the frame of the neutron star.

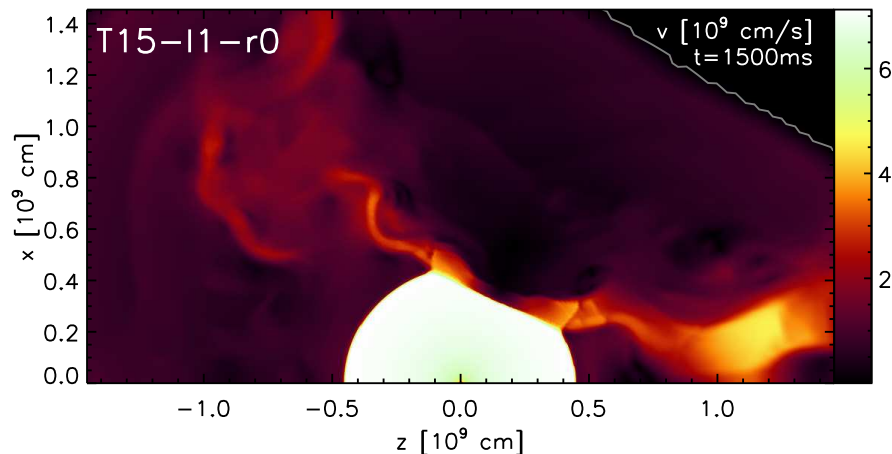


Figure 4.9: Velocity distribution in Model T15-11-r0 for $t = 1.5$ s. The jump of the velocity at the reverse shock is clearly visible and also the two main outflow streams formed as a consequence of the reverse shock shape, which comes from the evolution of the ejecta during the first half second of the explosion.

In Fig. 4.7 one can distinguish two points in the reverse shock at $\theta \approx 30$ and $\theta \approx 100$ where the angle ϕ changes abruptly. Fig. 4.8 illustrates, in a simplified way, the effect that such a kink in the reverse shock has on the flow across the discontinuity. The oblique shock is less effective in decelerating the flow, which leads to much higher velocities outside the non-spherical parts of the reverse shock than above the spherical parts. Furthermore, the wind hitting the non-spherical part of the reverse shock is deflected towards the radial flow outside of the spherical part of the reverse shock. These effects result in the formation of collimated high velocity outflows starting at the kinks (see Fig. 4.9). Moreover, the kinks of the reverse shock lead to minimum values of the pressure and entropy for the shocked material (see Fig. 4.4).

4.4 Two more models base on a $15 M_{\odot}$ progenitor

In this section we present two additional models based on the same progenitor as our reference case: T15-11-r1 and T15-12-r1 (see Table 4.1). These models develop different ejecta distributions due to the different neutrino luminosities and the chaotic dependence of the flow on the initial perturbations that were also chosen differently. We describe briefly the evolution of the two models, in order to be able to analyze the influence of the anisotropy on the reverse shock position and on the entropy of the shocked material.

The evolution of the Model T15-11-r1 is shown in Fig. 4.10 and values for several important quantities are given in Table 4.2. The initial model is the same as in the reference case described in Sect. 4.2 but the parameters are slightly different (see Table 4.1). Also the initial random perturbations are different. In the post-shock layer a negative entropy gradient establishes that leads to the beginning of the convection, which is clearly visible already in the first panel corresponding to a time of 200 ms after bounce. At 300 ms there are still downflows in the left part, while the wind is already starting in the right. This is visible by the almost constant value that the entropy reaches just outside the neutron star. About hundred ms later the wind has started in all directions and the reverse shock is visible as a jump of the entropy in the right part (see panel for $t = 400$ ms). The following evolution is less dynamic than the previous phase, the

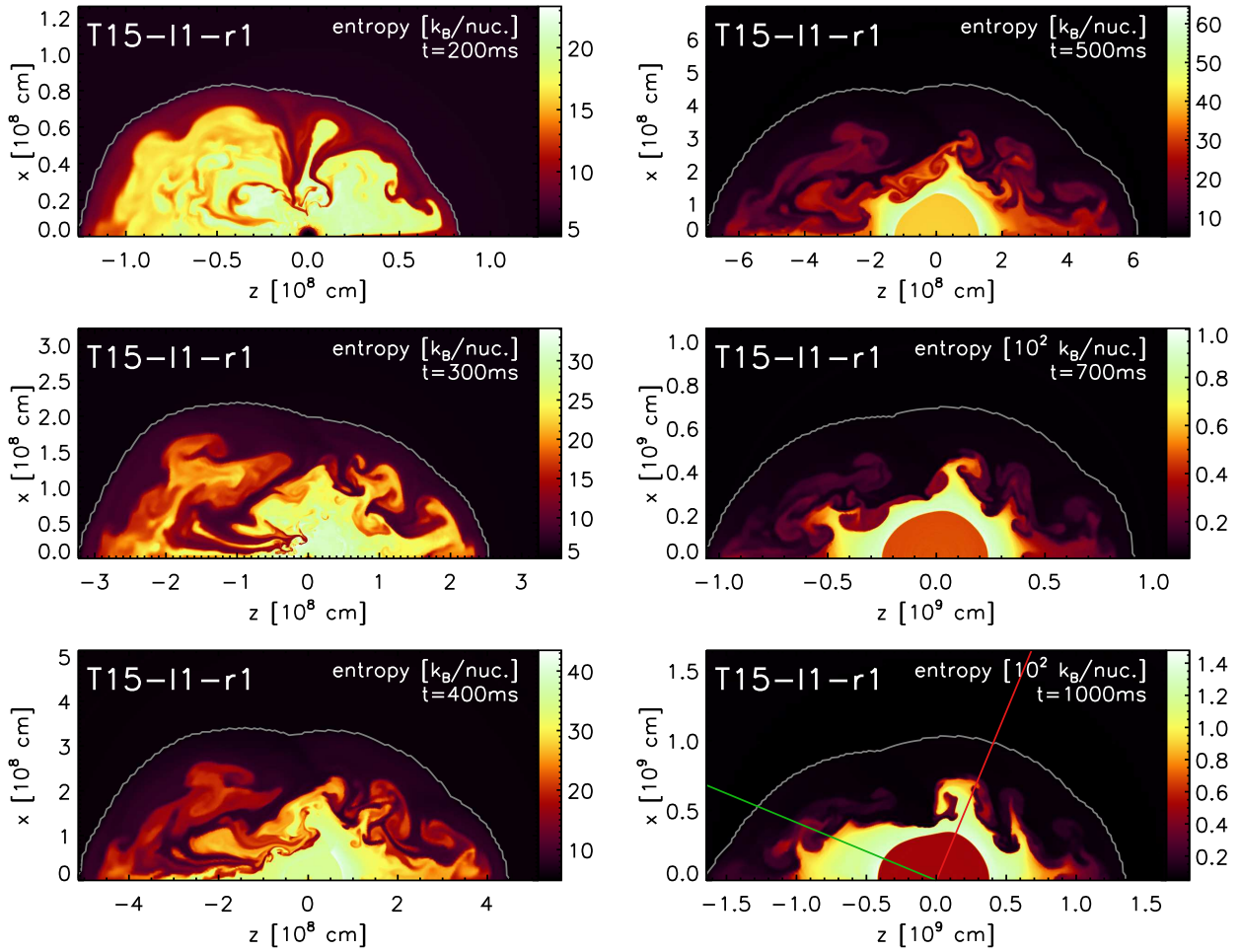


Figure 4.10: Entropy distribution in Model T15-11-r1 for different times. Same as Fig. 4.1.

wind material expands supersonically and the ejecta between shock and reverse shock moves outwards with a slow change of its structures. The reverse shock remains almost spherical symmetric until approximately one second after bounce. The spherical shape of the reverse shock (see panel for $t = 700$ ms) gives rise to the same situation as in one-dimensional simulations. One second after bounce the anisotropic distribution of the ejecta begins to affect to the reverse shock, which starts to develop a flat, non-spherical section like in the reference case (Sect. 4.2).

In contrast to this nearly spherical model, the evolution of Model T15-12-r1 is characterized by long-lasting downflows and a strongly anisotropic shape of the reverse shock, which last only a few tens milliseconds. In the panel for $t = 200$ ms of Fig. 4.11 one can see that the entropy distribution is rather homogeneous with the presence of only one narrow downflow (compare with the other models at the same time in Figs. 4.1 and 4.10). Here the formation and grow of the Rayleigh-Taylor mushrooms is also nicely visible. The subsequent evolution (see panels for $t = 300$ ms and $t = 400$ ms) is dominated by convection without a main downflow – instead many small structures prevail in this phase. After 500 ms, one can see that a main downflow has formed at an angle of approximately $\pi/4$ while a bubble inflates the north (right) hemisphere. The presence of this downflow continues until one second, and consequently there are two outflows at every side of the downflow. The expansion to the left and to the right of these outflows is visible in the panel for $t = 700$ ms. Moreover one can also see the deformation of

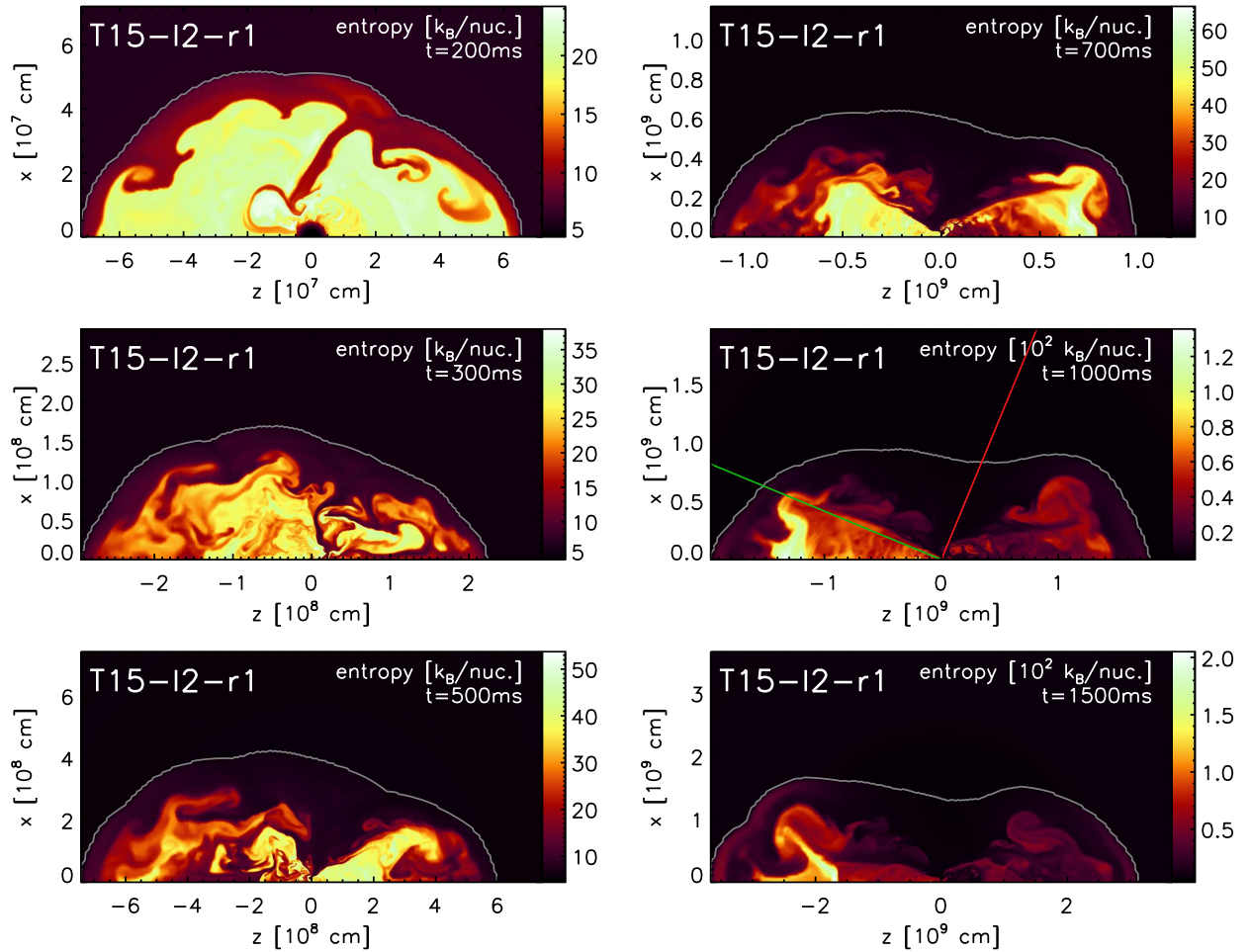


Figure 4.11: Entropy distribution in Model T15-l2-r1 for different times. Same as Fig. 4.1.

the shock due to this rapid expansion of the matter in certain directions. However, the development of these outflows is quite different. The outflow in the northern hemisphere (right side in Fig. 4.11) starts earlier but does not become supersonic. On the other hand, the outflow in the southern hemisphere is able to reach supersonic velocities and a reverse shock caused by the interaction with the preceding ejecta is already present at $t = 700$ ms (see Fig. 4.11). In the following, the entropy of the shocked matter increases and the reverse shock continues to expand, while there is not yet an indication of a spherical wind around the neutron star.

Why are the evolutions of these two models so different? The two models, T15-l1-r1 and T15-l2-r1, studied here have different inner boundary luminosities (see Table 4.1). The Model T15-l2-r1, i.e. the one with long-lasting downflows, has a lower luminosity at the inner boundary, which makes it more difficult to blow away the matter that is being accreted. Long-lasting downflows are possible, in particular for low explosion energies. However, here we see that even for similar explosion energy, one can find strong differences in the downflows behavior due to the chaotic dependence on the initial perturbation (Scheck et al. 2006; Scheck 2006). These two models have similar explosion energies because the matter that is responsible for the bulk of the explosion energy, is concentrated in a narrow shell just below the supernova shock. This region follows the evolution of the shock, which is very similar in the two models.

4.5 Progenitor variation

We have seen that the conditions for nucleosynthesis could be influenced by the reverse shock, and we have demonstrated, by analytic means (Sects. 3.4, 4.3), that its behavior depends on the evolution of the layer between the forward shock and the reverse shock. In the spherically symmetric case the behavior of this shell is strongly influenced by the progenitor structure. And in two-dimensional simulations we have seen that anisotropies emerging during the first second of the explosion have a big influence. It is, therefore, interesting to study the combined effect of the two ingredients: progenitor structure and ejecta anisotropy.

For the $10 M_{\odot}$ progenitor we have tried two different neutrino luminosities at the inner boundary (Table 4.1). Model T10-11-r1 has the same parameters as the one-dimensional Model M10-11-r1 (Table 3.1), however it has a very high explosion energy, $E_{\text{exp}} = 1.8 \text{ B}$ at 2 s after bounce. Therefore, we have performed another simulation with lower boundary luminosity, i.e. Model T10-12-r1.

Figure 4.12 shows that, for the Model T10-11-r1, the anisotropies develop very quickly, and at $t = 200 \text{ ms}$ (first panel), there is already a big deformation of the supernova shock. Between 200 ms and 500 ms the most remarkable feature is a big downflow near the equatorial plane ($\theta = \pi/2$). After half a second the wind has already started and the anisotropic matter distribution leads to a non-spherical reverse shock. Moreover, the rapid shock expansion caused by the steep density gradient present in this progenitor (see Fig. 2.1) produces a region of high entropy just below the shock radius. The following evolution is characterized by an increasingly strong deformation of the reverse shock and very high values of the entropy, which we found already for the same progenitor in the spherically symmetric simulations.

The Model T10-12-r1, which has lower boundary luminosity, develops also an anisotropic configuration with significant shock deformation after 200 ms (see Fig. 4.13). The shock expansion is slower than for Model T10-11-r1 in the first hundreds milliseconds. After 400 ms the wind starts and hits the ejecta, forming a rather spherical reverse shock. However, the small deviations from the spherical shape are enough to produce significant differences in the entropy of the shocked material. For this low-mass progenitor, the model with lower boundary luminosity develops a quasi-spherical reverse shock and the model with higher boundary luminosity becomes more anisotropic. In case of the $15 M_{\odot}$ progenitor (see Sect. 4.4), the opposite was true, i.e. the more spherically symmetric reverse shock appears in the simulation with higher boundary luminosity. This shows that the form of the reverse shock is not only influenced by the boundary luminosity, but depends also in a chaotic way on the initial perturbations. A more quantitative conclusion regarding the relative importance of these two dependencies would require more simulations.

We have chosen the $25 M_{\odot}$ progenitor to study a case of a progenitor more massive than the $15 M_{\odot}$ reference case (see Table 2.1). The parameters for Model T25-15-r4 (Table 4.1) are the same as for one-dimensional simulation for this progenitor. Owing to the convective overturn, which increases the efficiency of neutrino-heating, the explosion energy is significantly higher in two dimensions. Moreover, the explosion begins much earlier in the two-dimensional simulation ($t_{\text{exp}} = 0.197 \text{ s}$) than in the corresponding one-dimensional simulation ($t_{\text{exp}} = 0.401 \text{ s}$).

The evolution of the Model T25-15-r4 is shown in Fig. 4.14. Due to the high accretion rate the shock does not expand as rapidly as in less massive progenitors. After 200 ms the typical

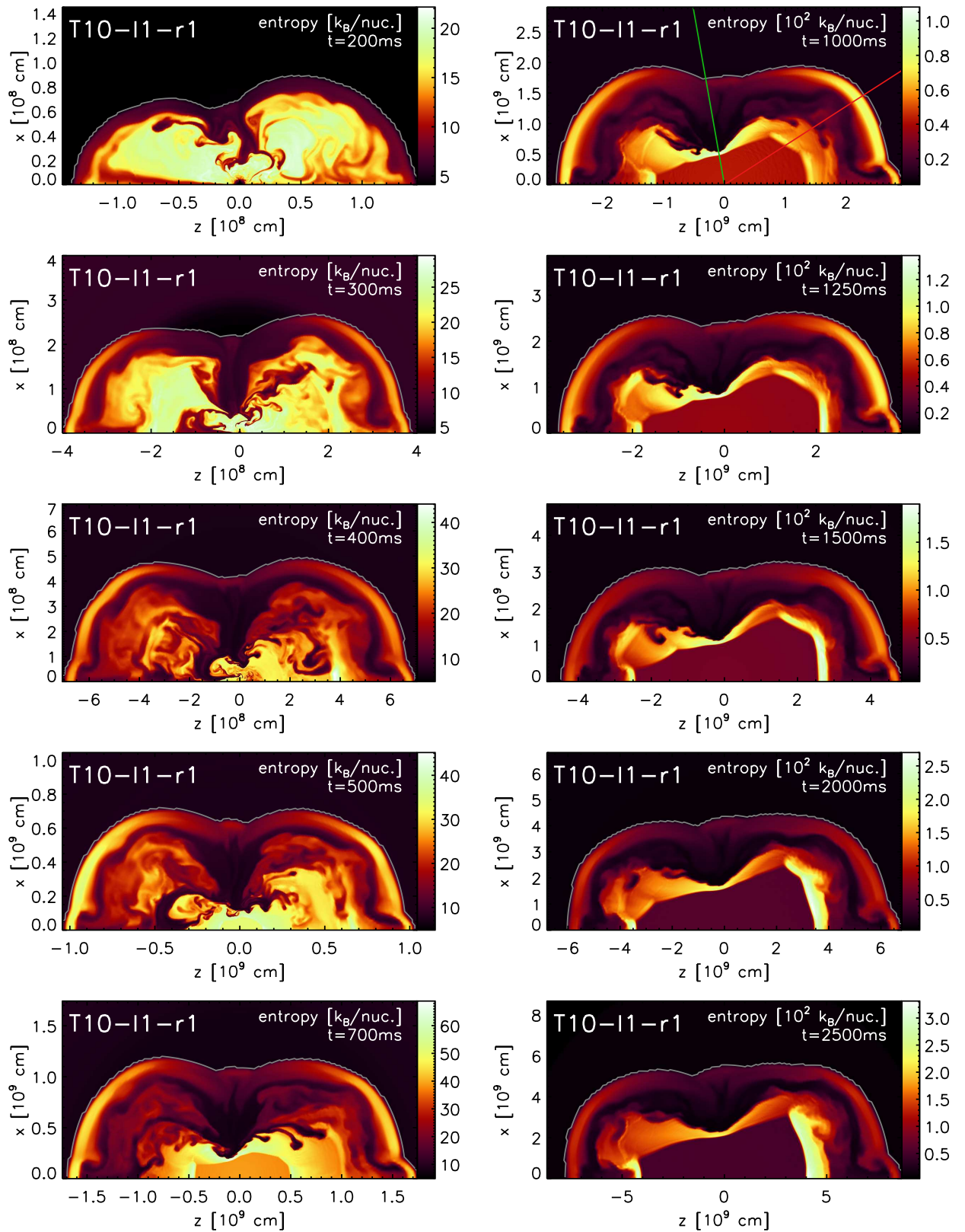


Figure 4.12: Entropy distribution in Model T10-11-r1 for different times. Same as Fig. 4.1.

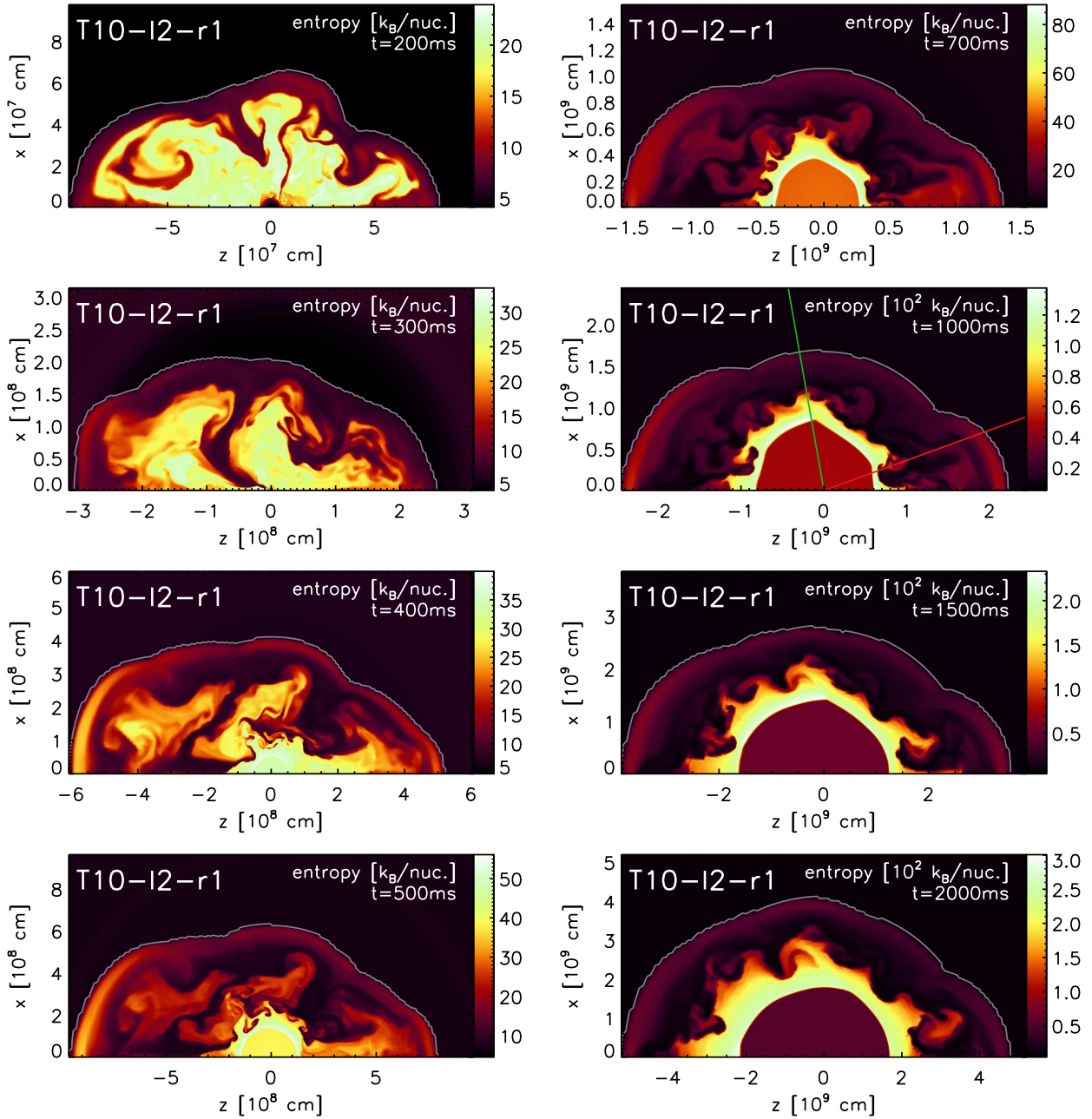


Figure 4.13: Entropy distribution in Model T10-I2-r1 for different times. Same as Fig. 4.1.

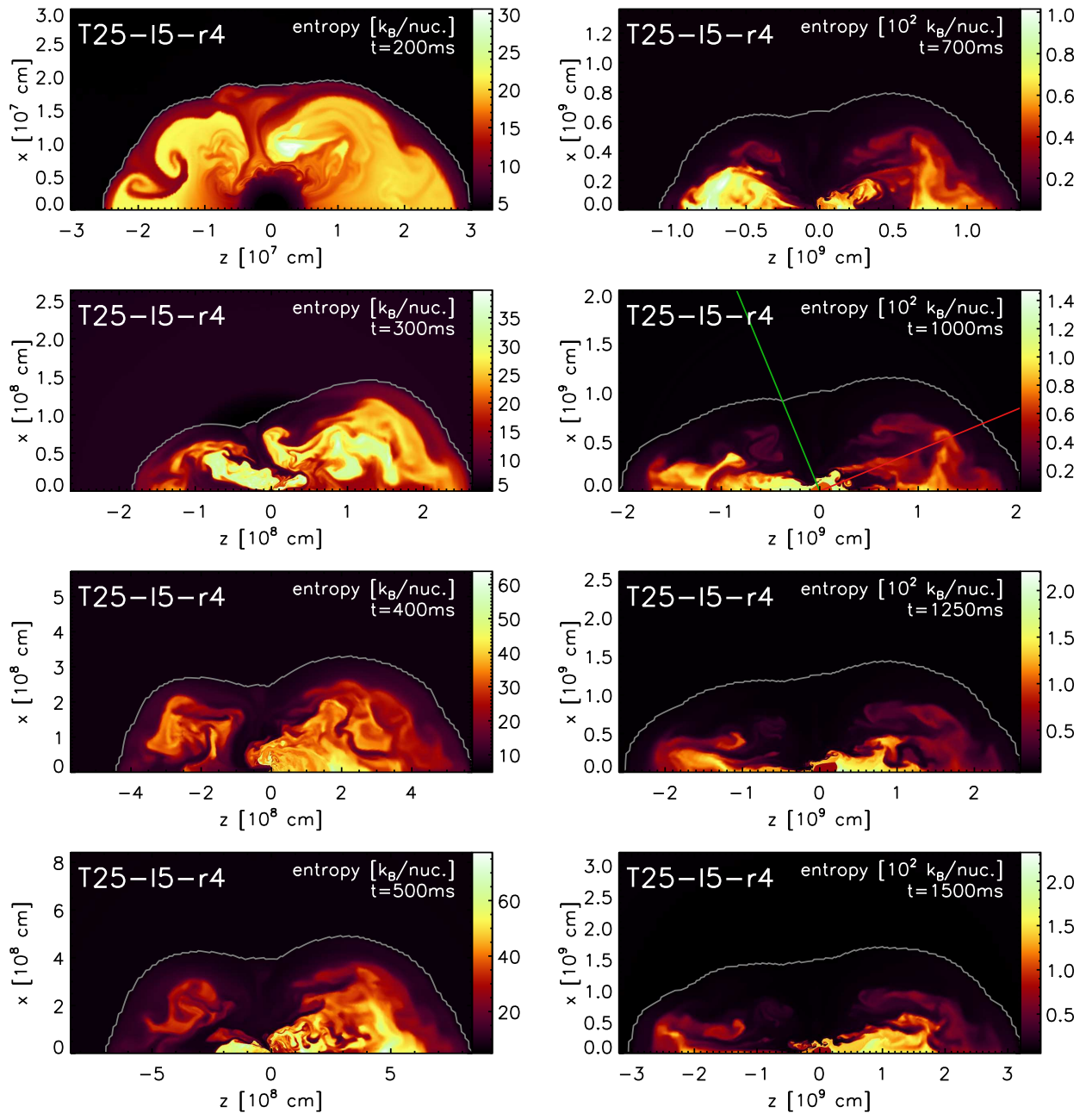


Figure 4.14: Entropy distribution in Model T25-15-r4 for different times. Same as Fig. 4.1.

two-dimensional structures have just started to emerge. However, in the following panels one can see that the instabilities are able to grow. Also as a consequence of the high accretion rate the downflows are quite stable and the wind is not able to blow them away from the vicinity of the neutron star until almost $t = 1$ s after bounce. Therefore, the ejecta have more time to develop a highly anisotropic pressure distribution, which leads to a non-spherical reverse shock. In simulations based on this rather extreme progenitor model we encountered several numerical problems that did not show up for less massive stars. This prevented us from computing more $25M_{\odot}$ models and even made impossible to continue the simulation of Model T25-15-r4 for longer time.

4.6 Comparison of one- and two-dimensional simulations

In this section we compare the typical values of the relevant quantities at the reverse shock in 1D and 2D. There are many possibilities to carry out such comparison. For example, one can consider two models of the same progenitor with similar explosion energy in 1D and 2D, or models, in which the explosion starts at the same time after bounce. The latter is much harder to achieve, as the explosion time is not known a priori. Therefore, our choice is to keep the same boundary parameters in one- and two-dimensional simulations. This means the explosion energies will be different, since the convection increases the efficiency of the neutrino energy deposition, thus changing also the time when the explosion starts. The models we investigate here are: T10-11-r1, T15-11-r0, and T25-15-r4 (see Table 4.1 for the boundary parameters). They can be directly compared to the one-dimensional models: M10-11-r1, M15-11-r1, and M25-15-r4, respectively.

From the models presented in this chapter it is obvious that 2D effects can have a strong influence on the conditions relevant for nucleosynthesis. Is the variation of the thermodynamic conditions due to 2D effects less or more important than the variation related to different progenitor stars that are visible in the one-dimensional simulations? In order to answer this question we show in Figs. 4.15, 4.16, 4.17, the evolution of entropy, pressure, density, and temperature of the shocked material, as well as the reverse shock radius for progenitor stars with masses of 10, 15, and 25 M_{\odot} , respectively. The red and green lines correspond to the angles marked with straight lines of the same colors in the plot of the entropy distribution for $t = 1000$ ms (Figs. 4.12, 4.1, and 4.14).

In Model T10-11-r1 the reverse shock position and orientation change considerably with angle (see Fig. 4.12). In the Figure 4.15 the red and green lines mark approximately the maximum and minimum radii of the reverse shock, respectively. The maximum value is only a bit larger than the one we found in the one-dimensional simulation for the same progenitor and initial parameters (Fig. 3.15). All other quantities shown in Fig. 4.15 are also in the same range as in 1D. Besides the angular variation, Fig. 4.15 shows that in 2D the properties of the matter behind the reverse shock do not evolve as smoothly as in 1D.

Figure 4.16 shows that for the 15 M_{\odot} the evolution is almost spherically symmetric, because the values for the red and green lines do not differ much from each other, although they correspond approximately to extreme reverse shock positions. Apart of a flat section of the reverse shock (see Sect. 4.2), the evolution is rather similar to 1D, not only qualitatively but also quantitatively (see Fig. 3.15).

In the case of the most massive progenitor, Model T25-15-r4, the quantities vary with time around a mean value (Fig. 4.17). The wind starts after half second, but the accretion continues and the reverse shock is destroyed again by downflows (Fig. 4.14). The wind reappears again but lasts only until another downflow reaches the reverse shock. The effect of the long-lasting downflows is visible by the points in Fig. 4.17 between half a second and one second, which mark the presence of the reverse shock just during a short time – there is not a continuous line like in the other progenitors for the same time. The high accretion rate prevents a fast expansion of the reverse shock, which stays at smaller radii than in less massive progenitors. This effect is the same as in the one-dimensional simulation. However, in 2D the evolution of the downflows leads to a varying deformation of the reverse shock, and therefore also of the properties in the shocked material vary. This can allow for larger entropy values in certain regions (compare Fig. 4.17 and Fig. 3.15).

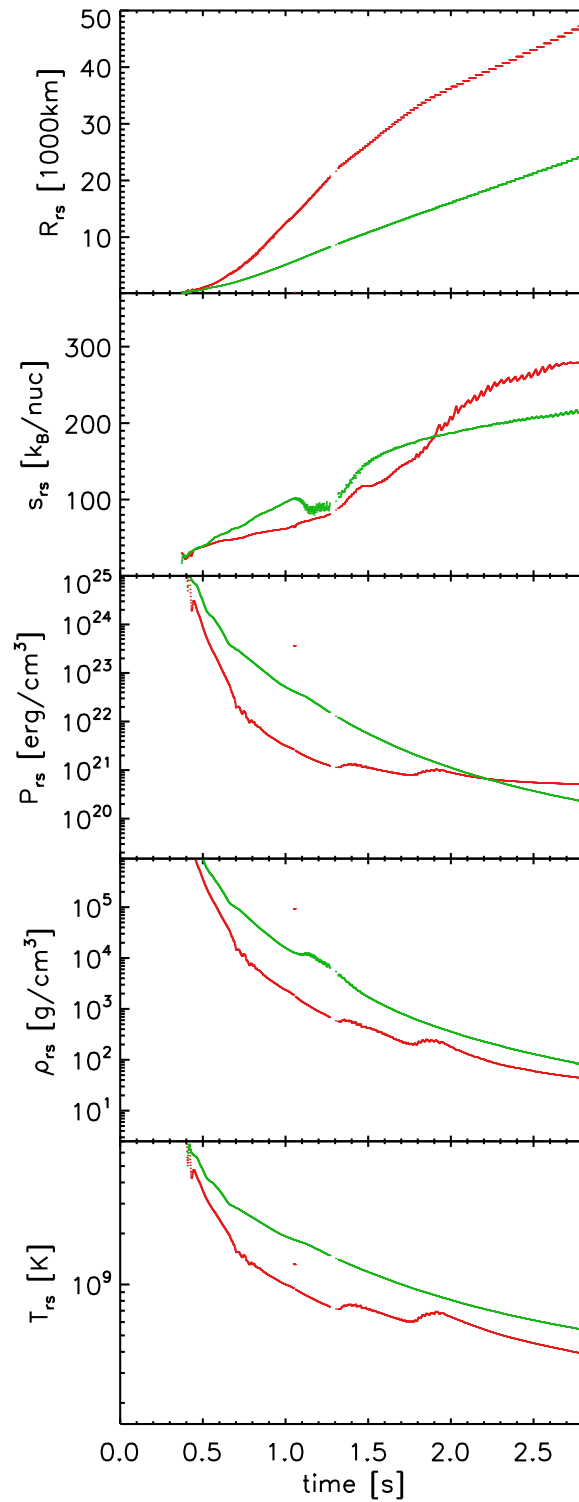


Figure 4.15: Time evolution of different quantities for the Model T10-11-r1. Shown are the radius of the reverse shock, and entropy per nucleon, pressure, density, and temperature downstream of the reverse shock. The red and green lines correspond to two chosen angles that are marked with the same color in the panel for $t = 1$ s of Fig. 4.12.

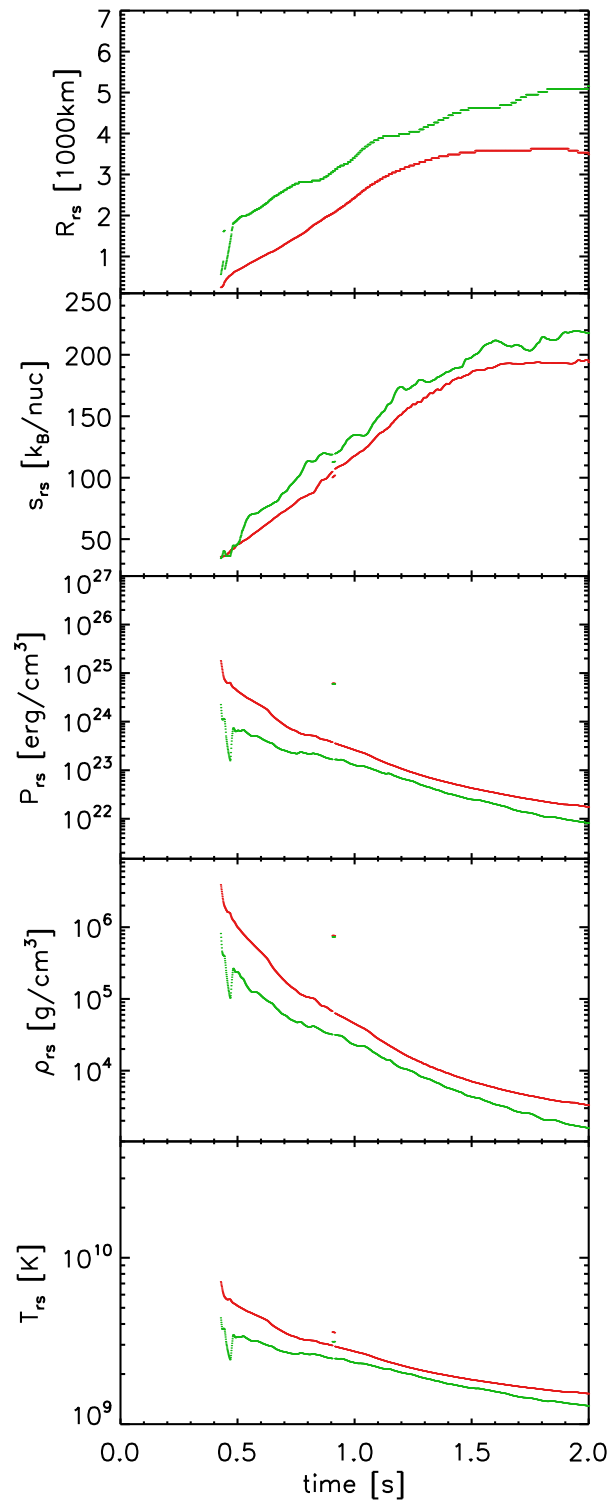


Figure 4.16: Same as Fig. 4.15 but for the Model T15-11-r0. Here the color lines are associated with the angles marked with the same colors in Fig. 4.1.

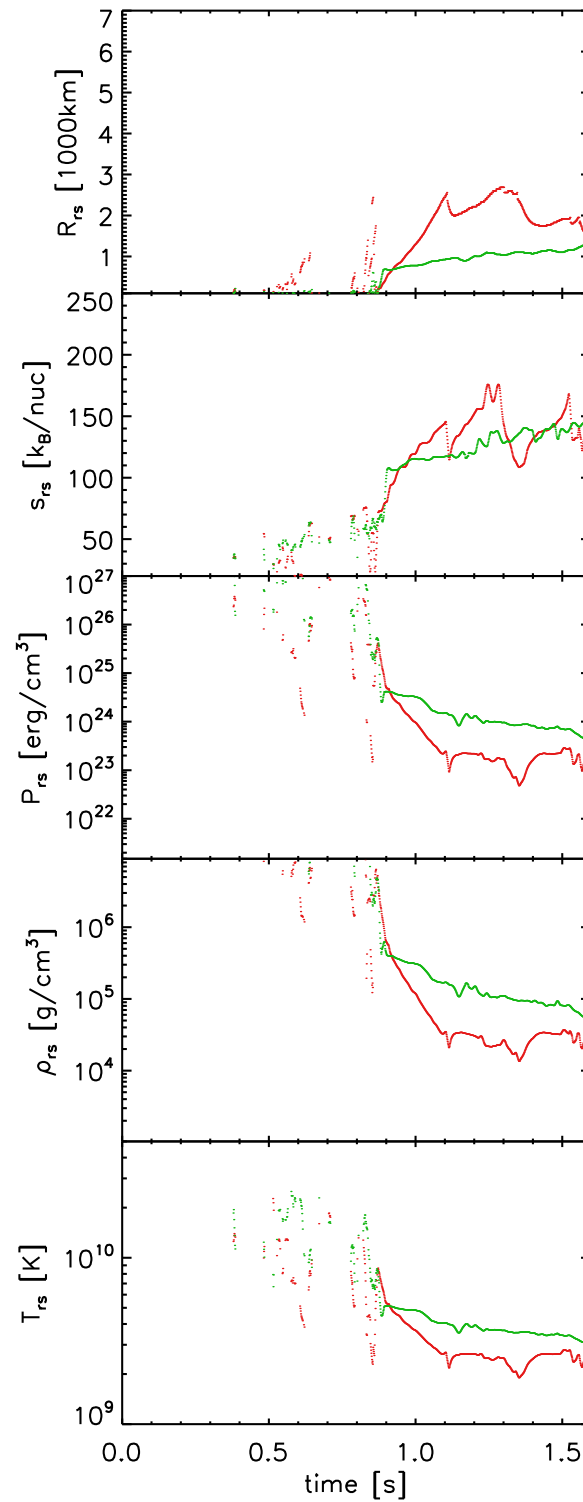


Figure 4.17: Same as Fig. 4.15 but for the Model T25-15-r4. Here the color lines are associated with the angles marked with the same colors in Fig. 4.14.

Two-dimensional simulations have a broader range of values for the properties of the shocked material than one-dimensional simulations. However, the progenitor dependence visible in the one-dimensional simulations is not completely destroyed by 2D effects. In particular there is a quite good agreement between 1D and 2D results for those angular beams where the reverse shock reaches its maximum radius and is perpendicular to the radial direction, i.e. the maximum values for the entropy are similar in 1D and 2D. To assess the influence of 2D effects on the nucleosynthesis more quantitatively, one has to compare the distribution functions of relevant quantities computed from one- and two-dimensional simulations. For this purpose we determine e.g. the total amount of matter that is ejected as a function of entropy by integrating over time the flux of mass for a given entropy value which goes through the reverse shock radius:

$$\Delta M(s_i < s < s_{i+1}) = \sum_n \sum_\theta \Delta A(R_{rs}, \theta, t_n) \cdot v_{rs}(R_{rs}, \theta, t_n) \cdot \rho_{rs}(R_{rs}, \theta, t_n) \cdot (t_{n+1} - t_n). \quad (4.9)$$

Here $A(R_{rs}, \theta, t_n) = 2\pi R_{rs}^2 (\cos \theta_{j+1} - \cos \theta_j)$ is the cell surface through which the matter flows. The first sum represents the integration over time, while the second sum integrates over those angular beams where the reverse shock is present and the entropy is in the considered range $s_i < s(R_{rs}, \theta, t_n) < s_{i+1}$.

Figure 4.18 shows the result of applying Eq. (4.9) for the three progenitors discussed before. The orange line results from performing the integration for the one-dimensional simulations. The mass distribution for the one-dimensional models are rather flat, i.e. the amount of mass is roughly of the same order for each entropy bin. This can be explained by the fact that on the one hand mass flux decreases strongly with time, but on the other hand the entropy varies more and more slowly. Therefore, although for a given entropy range the mean mass flux is lower for a larger entropy value, the time interval, in which such entropies prevail, is larger (see Fig. 4.19). For the $25 M_\odot$ one-dimensional model the entropy at late times varies so slowly that actually more mass is accumulated in the bins around $s = 200k_B/\text{nuc}$ (in $0.8\text{s} < t < 1.6\text{s}$) than for smaller entropies (see Fig. 3.15).

In the two-dimensional models the non-spherical reverse shock leads to a range of entropies at any given time. As the obliqueness of the reverse shock in 2D can easily reduce the entropy of the shocked matter, whereas large changes of the reverse shock radius are required to modify this entropy significantly, one can expect that in general the mass in the high-entropy bins is reduced in 2D. This effect is clearly visible in case of the $10 M_\odot$ model, where almost no mass with $s > 200k_B/\text{nuc}$ is produced in the two-dimensional model. However, this model shows also a second effect: The maximum entropies are somewhat higher than in 1D, because, due to the strong anisotropy of the model, parts of the reverse shock are located at a larger radius than in the corresponding 1D model (see Figs. 4.15 and 3.15). In case of the $15 M_\odot$ models, however, the higher maximum entropy in 2D is caused by the more compact neutron star and is not related to 2D effects. The latter are anyway very weak in Model T15-I1-r1, in which the reverse shock remains nearly spherical. This explains the good agreement of the histograms in this case.

Another remarkable feature of Fig. 4.18 appears in the low-entropy region, which is empty in the case of one-dimensional simulations. In spherically symmetric simulations the minimum value of the entropy corresponds to the wind entropy at the moment of the reverse shock formation. In contrast, for two-dimensional simulations this minimum value depends also on the orientation of the reverse shock with respect to the radial velocity, therefore lower values are also possible.

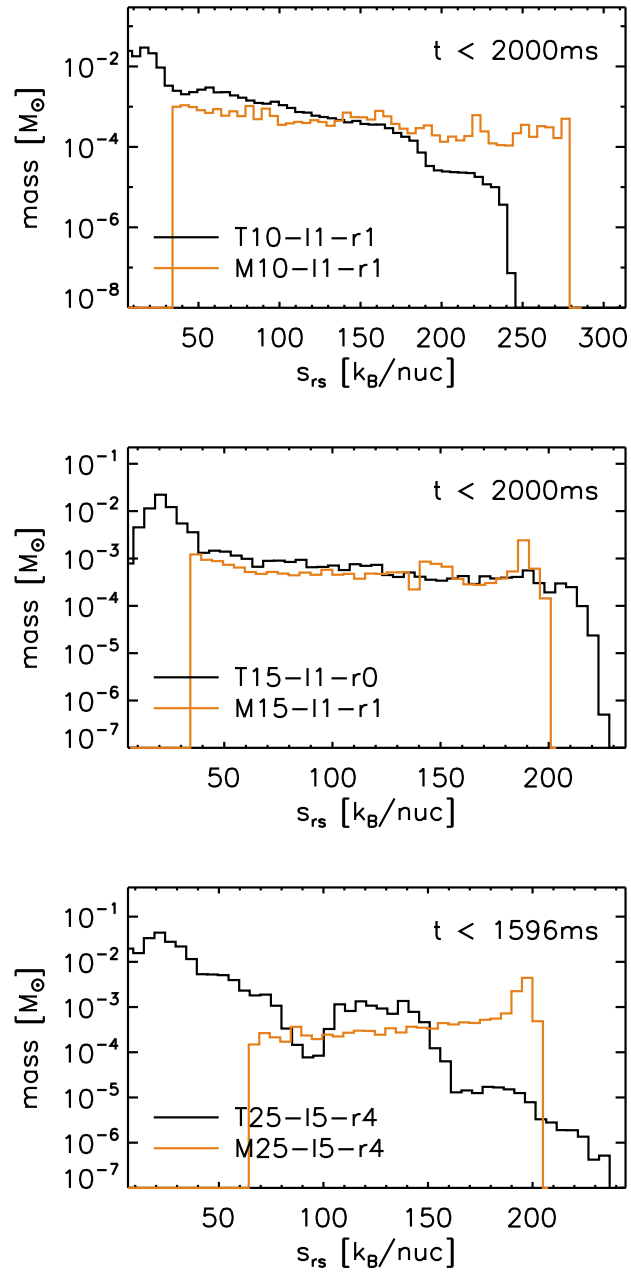


Figure 4.18: Ejecta mass vs. entropy of the matter crossing the reverse shock. The time integration of Eq. (4.9) is done from the moment the reverse shock appears until the end of two-dimensional simulation (this time is given in the every plot). The black and orange lines correspond to 2D and 1D simulations, respectively. The different panels corresponds to different progenitors: 10, 15, and $25 M_{\odot}$, from top to bottom.

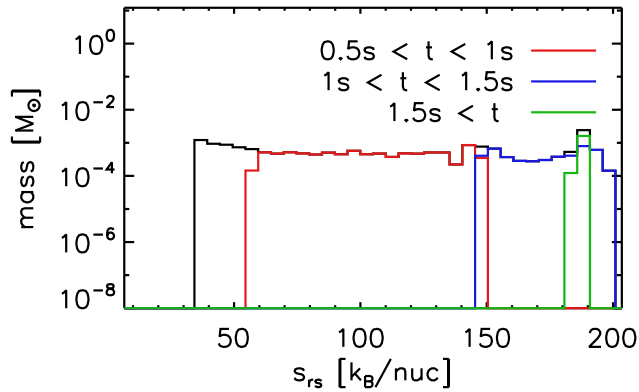


Figure 4.19: Ejecta mass vs. entropy of the matter crossing the reverse shock. Only the results for the Model M15-11-r1 (one-dimensional simulation) is shown. The different colors correspond to different time intervals for the integration of Eq. (4.9), and the black line corresponds to the total time between the formation of the reverse shock and $t = 2$ s after bounce.

This kind of histograms is also a tool to study the evolution of the electron fraction, Y_e . In Fig. 4.20 one can see the distribution of ejecta mass versus electron fraction for the two-dimensional simulations of the three progenitors discussed in this section. The black line corresponds to the integration of Eq. (4.9) for the whole time, i.e. from the formation of the reverse shock until the end of the simulations. The colors mark different integration intervals. At first, the matter is in the most proton-rich state and then moves towards the neutron-rich zone of the diagram, i.e. $Y_e < 0.5$. At the end of the simulations, the matter is still proton rich. In order to carry out a detailed analysis of the nucleosynthesis relevant-conditions therefore not only a larger number of two-dimensional simulations is required to be able to do some statistics, but also calculations following the supernova explosion for several seconds after bounce are needed to allow the matter to become neutron-rich.

4.7 Summary

In addition to the variability present in our one-dimensional models, multi-dimensional effects like long-lasting anisotropic accretion and directed outflow introduce a stochastic element in the supernova evolution during the first seconds of post-bounce evolution. The supernova ejecta in different directions can develop largely different conditions due to the strong anisotropy of the explosion mechanism and of the environment of the forming neutron star. The pronounced anisotropy is caused by hydrodynamic instabilities, which allow small seed perturbations to grow to large-amplitude global modes before the onset of the explosion. The morphology of the explosion ejecta depends in a unpredictable, chaotic way on the initial perturbations. What is the influence of these multidimensional effects on the interaction between wind and ejecta?

- The wind termination shock feature is also present in two dimensions. However, the reverse shock is non-spherical, which is a consequence of the anisotropic pressure distribution in the ejecta. We have shown by analytic means that a larger pressure above the reverse shock leads to a smaller reverse shock radius. The varying radius implies also that the parts of the shock are not oriented perpendicular, but at an oblique angle to the

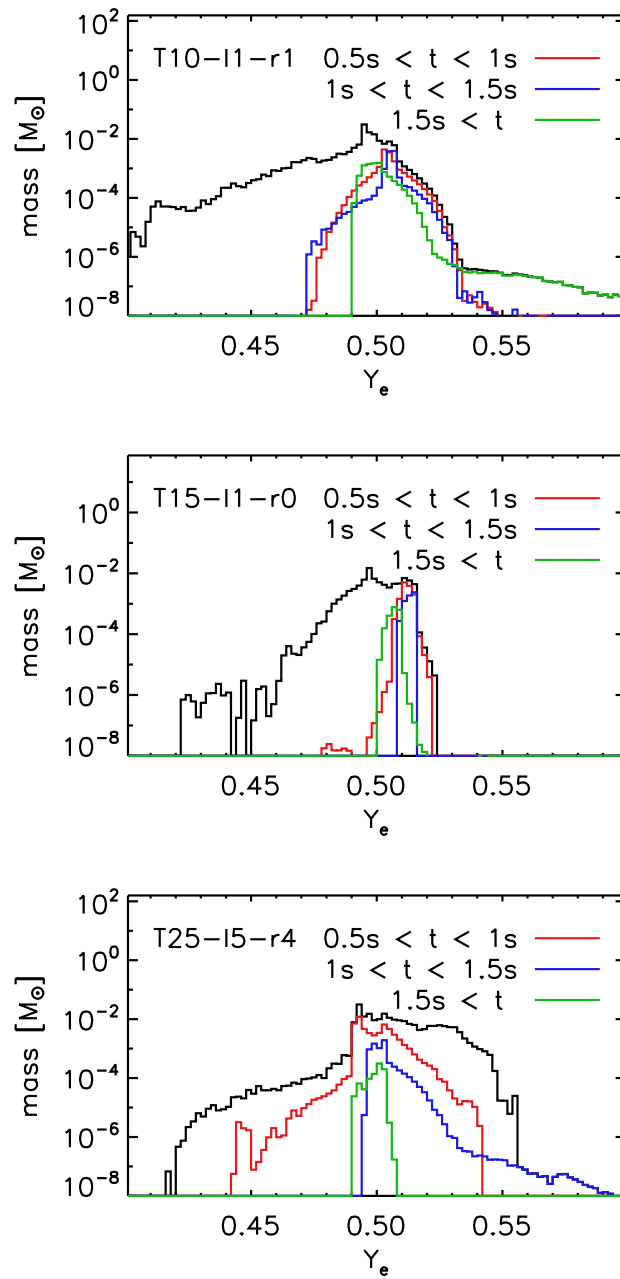


Figure 4.20: Ejecta mass vs. electron fraction of the matter crossing the reverse shock. Only the results for two-dimensional simulations are shown. The different colors correspond to different time intervals for the integration of Eq. (4.9), and the black line corresponds to the total time between the formation of the reverse shock and the end of the simulation. The different panels corresponds to different progenitors: 10, 15, and 25 M_{\odot} , from top to bottom.

radial direction. We observed often “kinks” in the reverse shock (i.e. points, where the obliqueness changes abruptly), which give rise to collimated high-velocity outflows.

- The shape of the reverse shock is time dependent – spherical reverse shocks can turn non-spherical and vice versa. It is even possible that the reverse shock does not contain the full solid angle, because long-lasting downflows of matter from the ejecta to the neutron star are still present. For higher boundary luminosities these downflows tend to be blown away earlier. However, when exactly this happens depends also sensitively and in a chaotic way on the initial random perturbation.
- There is no obvious dependence of the anisotropy on the progenitor mass – both strongly anisotropic and almost spherical reverse shocks are possible for low and high mass progenitors. The thermodynamic conditions around the non-spherical reverse shock in the two-dimensional models vary but are in general not far from those of the corresponding one-dimensional models, i.e. simulations with same boundary parameters. However, the amount of mass with given conditions, e.g. high entropy, is different compared to one-dimensional simulations. In 2D the obliqueness of the reverse shock tends to reduce the amount of high-entropy matter, whereas due to the varying reverse shock radius even higher maximum entropies are possible.

5

Summary and conclusions

The main nucleosynthesis process yielding elements heavier than iron is the rapid neutron capture on “seed nuclei”, also known as “r-process”. Rapid implies that several neutron captures take place before the nucleus undergoes a beta decay, so that the nuclei taking part in this process move far out of the “valley of β -stability”. The extreme conditions required for this nucleosynthesis process, i.e. high neutron densities and short dynamical time scales, point to cataclysmic astrophysical events as possible sites for the r-process. Already fifty years ago, core-collapse supernovae were proposed by Burbidge et al. (1957) and Cameron (1957) as the most promising scenario in which heavy elements can be synthesized by rapid neutron capture. The aim of this work was to understand better the role supernovae may play for the formation of heavy elements, in particular whether supernova explosions are a viable site for the creation of r-process elements.

Core-collapse supernovae are caused by the collapse of the iron core of a massive star, which leads to the formation of an extremely dense neutron star. During this process an outward traveling shock wave is generated in the center of the core. After the shock has been launched, most of its energy is lost in the dissociation of iron-group nuclei and therefore the shock stagnates. Yet, neutrinos streaming out from the nascent neutron star, could be able to deposit sufficient amounts of energy behind the shock wave to “revive” it. The shock wave would then propagate through the outer stellar layers, making them unbound and thus disrupting the star. This “neutrino-driven explosion mechanism” is the most promising way to explain core-collapse supernovae, although still it has to be shown that it works reliably. However, independent of the details of the explosion mechanism, once the explosion has set in and the shock expands, the densities around the neutron star must decline strongly. This allows for the formation of a neutrino-driven wind, i.e. due to strong neutrino heating, matter is blown from the neutron star surface and accelerated to supersonic velocities.

The conditions given in neutrino-driven winds — temperature, density (which together determine the entropy, $s \propto T^3/\rho$), neutron density, and expansion timescale — are interestingly close to allowing the r-process to happen. In the past years, the nucleosynthesis potential of this site

was studied by means of analytic models (Qian & Woosley 1996) and by numerically solving the wind equations for given boundary and initial parameters (Otsuki et al. 2000; Thompson et al. 2001). Yet, only for extreme and not generic parameters (i.e. for a very large neutron star mass near the upper mass limit and for a very small neutron star radius), it was possible to obtain the conditions needed for the generation of the heaviest elements (Thompson et al. 2001). Therefore, the question arises whether these models contain all the ingredients that are relevant for setting the conditions in this nucleosynthesis site. In pioneering two-dimensional hydrodynamical simulations of supernova explosions Janka & Müller (1995) and Burrows et al. (1995) found that the supersonic neutrino-driven wind is decelerated in a strong “reverse” or “termination” shock, when it hits the slower moving matter ejected earlier, at the onset of the explosion. Although the formation of this reverse shock cannot be treated directly by steady-state wind solutions, several groups tried to assess its possible influence by imposing an outer boundary condition with constant pressure (Sumiyoshi et al. 2000) or constant temperature (Wanajo et al. 2002). However, as Thompson et al. (2001) pointed out, the behavior of such a termination shock can be dependent on the stellar progenitor and on time, therefore the only way to study its impact is by performing hydrodynamical simulations of the long-time evolution of core-collapse supernova explosions and post-explosion outflows.

The one- and two-dimensional hydrodynamical simulations carried out for this work are the first detailed investigation of the interaction of the neutrino-driven baryonic outflow from the neutron star surface with the slower dense shell of ejecta that moves outwards behind the expanding supernova shock. The main result is that a wind termination shock can not only change the wind entropy by factors of a few, which is a huge value and an unexpected finding, but leads also to a much slower expansion of the shocked outflow after its deceleration. Furthermore, we confirmed the speculations of Thompson et al. (2001) that the reverse shock depends on the progenitor star and its behavior can vary strongly with time.

The wind properties and the evolution of the ejecta layer located between reverse shock and forward shock was found to be crucial to understand the behavior of the matter decelerated at the reverse shock. The basic dependence can be described by analytic means, showing that the entropy of the shocked gas attains higher values for increasing reverse shock radius and wind velocities. The development of the wind is determined (Qian & Woosley 1996) by the neutron star parameters (mass and radius) and neutrino properties (luminosity and energy). Since all these quantities are time dependent, e.g. the neutron star contracts and decreases in the gravitational mass due to its continuous loss of energy by neutrino emission, the reverse shock position and thus the properties of the shocked material vary with time. In extreme cases, characterised by rapid decrease of the neutrino luminosity (and consequently also of the wind power) or by slow supernova expansion in the more massive stars, the reverse shock retreats until it reaches the sonic point. At this position the reverse shock vanishes, leaving a subsonic breeze.

The pressure above the reverse shock has a direct influence on the reverse shock position and thus also on the entropy jump. This pressure is affected by the propagation of the forward shock, and thus by the progenitor structure, and by the anisotropies that develop in the ejecta layer. For a low-mass progenitor ($10 M_{\odot}$) with rather low mass accretion rate and a steep density gradient in the layer surrounding the iron core, the supernova shock and also the reverse shock were shown to expand very quickly. Due to the large radii reached by the reverse shock, the entropy of the shocked material can even reach $500 k_{\text{B}}/\text{nuc}$. However, the low temperatures that prevail at such radii suggest that the influence of the reverse shock on the nucleosynthesis in the

supernova outflow is negligible in this case. On the other hand, more massive progenitors (e.g. $25 M_{\odot}$ stars) develop a rather modest entropy jump at the reverse shock, since the latter remains at comparably small radii. Yet, because of the more massive neutron star the wind entropies are higher (Qian & Woosley 1996) than in less massive progenitors. The high wind entropy values and the short expansion timescales might allow for a larger number of free neutrons per seed nucleus. This composition together with the sudden deceleration of the matter, which happens at a radius where the wind temperature is still high, might be better suitable for efficient r-processing.

The other aspect, which affects the evolution of the reverse shock is the anisotropic matter distribution of the ejecta caused by hydrodynamic instabilities. Two-dimensional simulations show that a pronounced explosion anisotropy does not prevent the formation of a reverse shock. However, the reverse shock is strongly deformed in particular due to the presence of downdrafts of dense, low-entropy matter. The radius and the orientation (relative to the radial direction) of the reverse shock lead to an angular dependence of the properties of the shocked-matter. Therefore, the amount of ejected matter with certain conditions, e.g. high entropy, differs between the spherically symmetric and two-dimensional cases. This will have consequences for the yields of nucleosynthesis production in the ejecta.

Because of the involved approximations and assumptions (e.g. an inner boundary that mimics the evolution of the shrinking neutron star, and a simplified neutrino transport that allows to save computational time), the calculations developed here can only be suggestive but are not suitable for making definitive predictions of the nucleosynthesis-relevant conditions in dependence of the progenitor star. The main goal of this work was therefore a matter-of-principle study of the interaction of the neutrino-driven wind and the slow-moving ejecta. In spite of the mentioned limitations and although detailed nucleosynthesis network calculations are essential to draw conclusions about the influence of the reverse shock on the production of heavy elements, one can already speculate about possible implications.

Only if the reverse shock affects the wind during (or prior to) a phase of its expansion which is important for the operation of n-capture reactions, i.e. at temperatures around and somewhat below 10^9 K and neutron densities of 10^{23} – 10^{26} cm^{-3} , the wind termination shock may have a decisive influence on the possibility of high-mass r-process elements to form. Such conditions could rather discontinuously depend on the way the explosion starts to develop, on progenitor properties, and on anisotropies in the ejecta, because the reverse shock needs to be at a beneficial location during a certain evolution phase of the neutrino wind. Moreover, the proton-richness of the early supernova ejecta, which is seen in our models as well as in state-of-the-art simulations with energy-dependent neutrino transport, points to the later stages of the neutrino wind as more likely site for r-processing.

An important result of the simulations performed for this work is the fact that the material is dramatically slowed down and reheated when it crosses the reverse shock, causing an abrupt change of the expansion timescale, i.e. density and temperature do not drop by several orders of magnitude in milliseconds as in the wind phase, but they decrease just slightly during seconds. This has two effects: on one hand, the neutron capture can proceed for a longer time, and can even continue until all the free neutrons are captured on heavy nuclei; on the other hand, the beta decay timescale is not any more restricted to be as short as the expansion timescale of the fast wind. The latter will affect the path along which the r-process takes place in the plane of neutron number vs. proton number, and thus it probably changes the requirements for the wind

condition, which could become less extreme than the ones needed for making the r-process elements in the neutrino-driven wind without reverse shock deceleration.

Although the wind termination could provide improved conditions for the r-process, it remains to be investigated whether and when the production of heavy elements for this modified site is compatible with observational constraints coming from the r-process element abundances in very old stars in the Galactic halo — known as ultra metal-poor (UMP) halo stars. The interstellar medium in which these ultra metal-poor stars were formed was already enriched with those heavy elements. The abundance pattern observed in the solar system and in the ultra metal-poor stars is the same, especially in the range of atomic numbers between 35 and 55 (Cowan & Thielemann 2004; Cowan & Sneden 2006). This implies that the r-process has taken place in a very robust way for a long time. Therefore, the varying conditions in the neutrino-driven wind and the strong time- and progenitor-dependence of the behavior of the wind termination shock and of its effects on the wind raise a serious question: Do supernova cores provide the environment for producing the extremely uniform solar-system like r-process abundance pattern between the Ba- and Pt-peaks observed in ultra metal-poor stars?

Certainly a larger number of simulations in one and two dimensions combined with detailed nucleosynthesis calculations is needed to study such questions and come to more definitive conclusions. Especially in the two-dimensional case it would be important to perform enough simulations to have reasonable set of models which show the possible variation of conditions and their links to governing parameters of the problem. Improved neutrino transport methods will bring a more accurate prediction of relevant wind properties. Moreover, using more progenitor stars and including rotation might reveal interesting new phenomena. For r-process nucleosynthesis the later stages of the developing explosion are the most interesting ones. Therefore running the simulations for several seconds will be crucial in our future work.

Bibliography

- Arcones, A., Janka, H.-T., & Scheck, L. 2007, A&A, submitted 13
- Argast, D., Samland, M., Thielemann, F.-K., & Qian, Y.-Z. 2004, A&A, 416, 997 7
- Arnett, D. 1996, Supernova and Nucleosynthesis (Princeton UP) 5, 7
- Bethe, H. A. 1990, Reviews of Modern Physics, 62, 801 8
- Bethe, H. A. & Wilson, J. R. 1985, ApJ, 295, 14 8
- Buras, R., Janka, H.-T., Rampp, M., & Kifonidis, K. 2006a, A&A, 457, 281 8, 13, 18, 22
- Buras, R., Rampp, M., Janka, H.-T., & Kifonidis, K. 2003, Physical Review Letters, 90, 241101 8, 13
- Buras, R., Rampp, M., Janka, H.-T., & Kifonidis, K. 2006b, A&A, 447, 1049 8, 12, 13, 18, 37
- Burbidge, E. M., Burbidge, G. R., Fowler, W. A., & Hoyle, F. 1957, Reviews of Modern Physics, 29, 547 5, 6, 7, 81
- Burrows, A., Hayes, J., & Fryxell, B. A. 1995, ApJ, 450, 830 8, 12, 82
- Burrows, A. & Lattimer, J. M. 1986, ApJ, 307, 178 8
- Burrows, A., Livne, E., Dessart, L., Ott, C. D., & Murphy, J. 2006, ApJ, 640, 878 8
- Cameron, A. G. W. 1957, PASP, 69, 201 5, 81
- Cameron, A. G. W. 2001, ApJ, 562, 456 7
- Cardall, C. Y. & Fuller, G. M. 1997, ApJ, 486, L111 11, 27
- Clayton, D. D. 1968, Principles of stellar evolution and nucleosynthesis (Univ. Chicago Press) 5, 6
- Colella, P. & Woodward, P. R. 1984, Journal of Computational Physics, 54, 174 16
- Colgate, S. A. & White, R. H. 1966, ApJ, 143, 626 8
- Cowan, J. J. & Sneden, C. 2006, Nature, 440, 1151 84
- Cowan, J. J. & Thielemann, F.-K. 2004, Physics Today, 57, 47 84
- Duncan, R. C., Shapiro, S. L., & Wasserman, I. 1986, ApJ, 309, 141 9

- Freiburghaus, C., Rosswog, S., & Thielemann, F.-K. 1999, *ApJ*, 525, L121 7
- Fröhlich, C., Hauser, P., Liebendörfer, M., et al. 2006a, *ApJ*, 637, 415 10
- Fröhlich, C., Hauser, P., Liebendörfer, M., et al. 2005, *Nuclear Physics A*, 758, 27 11
- Fröhlich, C., Martínez-Pinedo, G., Liebendörfer, M., et al. 2006b, *Physical Review Letters*, 96, 142502 11
- Heger, A., Woosley, S. E., Martínez-Pinedo, G., & Langanke, K. 2001, *ApJ*, 560, 307 23
- Herant, M., Benz, W., Hix, W. R., Fryer, C. L., & Colgate, S. A. 1994, *ApJ*, 435, 339 8
- Hoffman, R. D., Woosley, S. E., Fuller, G. M., & Meyer, B. S. 1996, *ApJ*, 460, 478 11
- Janka, H.-T. 1991, *A&A*, 244, 378 18, 31
- Janka, H.-T. & Müller, E. 1995, *ApJ*, 448, L109 8, 12, 32, 82
- Janka, H.-T. & Müller, E. 1996, *A&A*, 306, 167 8, 16
- Keil, W. & Janka, H.-T. 1995, *A&A*, 296, 145 8
- Kifonidis, K., Plewa, T., Janka, H.-T., & Müller, E. 2003, *A&A*, 408, 621 16
- Kitaura, F. S., Janka, H.-T., & Hillebrandt, W. 2006, *A&A*, 450, 345 8
- Kotake, K., Sato, K., & Takahashi, K. 2006, *Reports of Progress in Physics*, 69, 971 8
- Landau, L. & Lifshitz, E. 1959, *Course of Theoretical Physics. Fluid mechanics*, Vol. Vol. 6 (Pergamon) 62
- Lattimer, J. M., Mackie, F., Ravenhall, D. G., & Schramm, D. N. 1977, *ApJ*, 213, 225 7
- Lattimer, J. M. & Swesty, D. F. 1991, *Nuclear Physics A*, 535, 331 22
- LeBlanc, J. M. & Wilson, J. R. 1970, *ApJ*, 161, 541 7
- Liebendörfer, M., Mezzacappa, A., Thielemann, F.-K., et al. 2001, *Phys. Rev. D*, 63, 103004 8
- Liebendörfer, M., Rampp, M., Janka, H.-T., & Mezzacappa, A. 2005, *ApJ*, 620, 840 8, 27
- Marek, A., Dimmelmeier, H., Janka, H.-T., Müller, E., & Buras, R. 2006, *A&A*, 445, 273 16, 17, 27
- Meyer, B. S. 1994, *ARA&A*, 32, 153 11
- Meyer, B. S., Mathews, G. J., Howard, W. M., Woosley, S. E., & Hoffman, R. D. 1992, *ApJ*, 399, 656 10, 11
- Mezzacappa, A., Liebendörfer, M., Messer, O. E., et al. 2001, *Physical Review Letters*, 86, 1935 8
- Otsuki, K., Tagoshi, H., Kajino, T., & Wanajo, S. 2000, *ApJ*, 533, 424 9, 11, 18, 27, 30, 31, 33, 36, 82

- Pons, J. A., Reddy, S., Prakash, M., Lattimer, J. M., & Miralles, J. A. 1999, *ApJ*, 513, 780 8
- Pruet, J., Hoffman, R. D., Woosley, S. E., Janka, H.-T., & Buras, R. 2006, *ApJ*, 644, 1028 11
- Pruet, J., Woosley, S. E., Buras, R., Janka, H.-T., & Hoffman, R. D. 2005, *ApJ*, 623, 325 11, 12, 37
- Qian, Y.-Z. 2000, *ApJ*, 534, L67 7
- Qian, Y.-Z. & Woosley, S. E. 1996, *ApJ*, 471, 331 11, 26, 27, 33, 36, 37, 43, 82, 83
- Rampp, M. & Janka, H.-T. 2000, *ApJ*, 539, L33 8
- Rampp, M. & Janka, H.-T. 2002, *A&A*, 396, 361 8, 16, 18
- Rosswog, S., Liebendörfer, M., Thielemann, F.-K., et al. 1999, *A&A*, 341, 499 7
- Scheck, L. 2006, PhD thesis, Technische Universität München 56, 57, 67
- Scheck, L., Kifonidis, K., Janka, H.-T., & Müller, E. 2006, *A&A*, 457, 963 12, 16, 18, 19, 20, 22, 26, 27, 30, 31, 37, 56, 57, 67
- Scheck, L., Kifonidis, K., Janka, H.-T., & Müller, E. 2007, *A&A* 57
- Scheck, L., Plewa, T., Janka, H.-T., Kifonidis, K., & Müller, E. 2004, *Physical Review Letters*, 92, 011103 12
- Sumiyoshi, K., Suzuki, H., Otsuki, K., Terasawa, M., & Yamada, S. 2000, *PASJ*, 52, 601 12, 27, 31, 54, 82
- Takahashi, K. & Janka, H.-T. 1997, in *Origin of matter and evolution of galaxies in the universe '96*, ed. T. Kajino, Y. Yoshii, & S. Kubono, 213 9
- Takahashi, K., Witt, J., & Janka, H.-T. 1994, *A&A*, 286, 857 11
- Terasawa, M., Sumiyoshi, K., Yamada, S., Suzuki, H., & Kajino, T. 2002, *ApJ*, 578, L137 12
- Thompson, T. A., Burrows, A., & Meyer, B. S. 2001, *ApJ*, 562, 887 11, 12, 15, 18, 27, 28, 30, 31, 33, 36, 37, 39, 82
- Thompson, T. A., Burrows, A., & Pinto, P. A. 2003, *ApJ*, 592, 434 8
- Wanajo, S. 2006, *ApJ*, 650, L79 11
- Wanajo, S., Itoh, N., Ishimaru, Y., Nozawa, S., & Beers, T. C. 2002, *ApJ*, 577, 853 12, 39, 54, 82
- Wanajo, S., Kajino, T., Mathews, G. J., & Otsuki, K. 2001, *ApJ*, 554, 578 11, 36
- Wilson, J. R. 1985, in *Numerical Astrophysics*, ed. J. M. Centrella & R. L. Bowers (Boston: Jones and Bartlett), 422 8
- Witt, J., Janka, H.-T., & Takahashi, K. 1994, *A&A*, 286, 841 10, 11, 36

Woosley, S. & Janka, T. 2005, *Nature Physics*, 1, 147–8

Woosley, S. E. & Baron, E. 1992, *ApJ*, 391, 228–9, 11

Woosley, S. E., Heger, A., & Weaver, T. A. 2002, *Reviews of Modern Physics*, 74, 1015–7, 23

Woosley, S. E. & Hoffman, R. D. 1992, *ApJ*, 395, 202–10, 11

Woosley, S. E. & Weaver, T. A. 1995, *ApJS*, 101, 181–23

Woosley, S. E., Wilson, J. R., Mathews, G. J., Hoffman, R. D., & Meyer, B. S. 1994, *ApJ*, 433, 229–11

Acknowledgments

En primer lugar quiero dar las gracias a mi familia. A mis padres quiero agradecerles todo el apoyo que me han dado durante estos años de doctorado. Sin sus consejos, sus “valores éticos y estéticos”, los 15 minutos al día, el sobrepeso en el aeropuerto y todas aquellas pequeñas cosas, este trabajo no habría sido posible. A ellos y a mis hermanos, Julia y Ángel, también me gustaría darles las gracias por hacerme sentir que no ha cambiado nada cada vez que vuelvo a casa.

I want to thank my supervisor, Hans Thomas Janka, for his support and advice. I am indebted to him for the project he gave me and for guiding me at every step. I am very grateful to him for the enthusiasm he shows in every discussion, in every explanation. This was enough as motivation to go to the Mensa. His broad knowledge of the field together with his critic point of view and his “I don’t believe it” encouraged me to learn more, to read more, and to question more. Also I want to say thank you to Thomas for his patient and his understanding in difficult moments.

A special thanks goes to Leonhard Scheck, Konstantinos Kifonidis and Robert Buras for sharing with me their experience in simulating supernovae. Their support, advice and the discussions were very useful and a good complement to Thomas. The patient explanations of Konstantinos were crucial in the first year to start working with the hydro-code. This work would not have been possible without the help of the Leonhard who helped me in all the stages, from debugging to writing, from the nice physics to the nice plots. Danke technischer Berater.

I also would like to thank Wolfgang Hillebrandt (especially for the advices in last months of taking decisions) Ewald Müller and all the hydro-group. In particular, I want to say thank you to my office mates: Shu, Robert, Leonhard, and Martin. The MPA and IMPRS are acknowledged for making a nice environment to work.

I am grateful to S. Woosley and A. Heger for providing me with the progenitor models, to A. Marek for computing the collapse with the VERTEX code. The computations were performed on the NEC SX-5/3C and the IBM p690 “Regatta” system of the Rechenzentrum Garching, and on the IBM p690 cluster “Jump” of the John von Neumann Institute for Computing (NIC) in Jülich.

Finally, I want to say thank you to all my friends from here and from there. If I try to write all the names, I will forget someone, therefore I just say gracias, Danke, tesekkürler, grazie, Tak, Thank you.

Curriculum Vitae

Name: Almudena Arcones Segovia

Geburtsdatum: 21.8.1979
Geburtsort: Madrid

Schulbildung: 1985–1993 C.P. Federico Garcia Lorca, Majadahonda (Madrid)
1993–1997 I.E.S. Carlos Bousoño, Majadahonda (Madrid)

Studium: 9/1997–02/2003 Physik, Universidad Complutense de Madrid
10/2000-08/2002 Hauptstudium, Spezialisierung auf Astrophysik
11/2002-11/2003 Diplomarbeit am Max-Planck-Institut für Astrophysik
Titel: “*Studies of Neutrino-Heating and Shock-Revival Phase in a Supernova Core by Using an Analytic Toy Model*”
Betreuer: Dr. Hans Thomas Janka
02/2003 Akademischer Grad “Licenciada en Ciencias Físicas”
seit 01/2004 Promotion in Allgemeiner Physik
Technische Universität München und
Max-Planck-Institut für Astrophysik
Titel der Dissertation: “*On Nucleosynthesis-Relevant Conditions in Neutrino-Driven Supernova Outflows*”
Betreuer: Dr. Hans-Thomas Janka

Max-Planck-Institut für Astrophysik

**On Nucleosynthesis-Relevant Conditions
in Neutrino-Driven Supernova Outflows**

Almudena Arcones Segovia